

# **Near-field characterization of Bloch surface waves based 2D optical components**

THÈSE N° 7870 (2017)

PRÉSENTÉE LE 22 AOÛT 2017

À LA FACULTÉ DES SCIENCES ET TECHNIQUES DE L'INGÉNIEUR

LABORATOIRE D'OPTIQUE APPLIQUÉE

PROGRAMME DOCTORAL EN PHOTONIQUE

ÉCOLE POLYTECHNIQUE FÉDÉRALE DE LAUSANNE

POUR L'OBTENTION DU GRADE DE DOCTEUR ÈS SCIENCES

PAR

**Richa DUBEY**

acceptée sur proposition du jury:

Prof. L. Thévenaz, président du jury

Prof. H. P. Herzig, directeur de thèse

Prof. E. Descrovi, rapporteur

Prof. M.-P. Bernal, rapporteuse

Prof. F. Sorin, rapporteur



ÉCOLE POLYTECHNIQUE  
FÉDÉRALE DE LAUSANNE

Suisse  
2017



# Abstract

Bloch surface waves (BSWs) are surface electromagnetic modes that propagate at the interface between a multilayer substrate and a homogeneous external medium. The optical field of the surface mode is confined near the surface of the multilayer. This vertical confinement as well as the low absorption inherent to the dielectric materials make the BSWs an interesting candidate for the development of 2D optical systems and sensors. Such a periodic multilayer structure is introduced as a platform on which many optical functions can therefore be created.

In this thesis, two-dimensional optical components based on the Bloch wave platform are studied, in particular: a disk resonator, a Bessel-like beam generator and a waveguide grating as a Bragg mirror engraved in a waveguide. The optical properties of the components such as the resonance inside the disc, the "quasi non-diffracting" behavior and the reflection properties are presented. The 2D optical components are designed from a commercial FDTD program (CST Microwave studio). They are then characterized by a near-field scanning microscope with multi-heterodyne detection (MH-SNOM). Thanks to the MH-SNOM, it is possible to map the field distribution locally at the surface of the structures with a resolution lower than the wavelength. Simultaneous measurement of amplitude and phase allows a detailed reconstruction of the complex amplitude of the electric field.

In a first part, the influence of a device layer of material with a high refractive index ( $\text{TiO}_2$ ) is studied. The impact of the thickness of the  $\text{TiO}_2$  layer on the propagation properties of the BSWs is presented. It is demonstrated that by adapting the thickness of the device layer, the BSW dispersion curve position can be moved within the photonic band gap and consequently the BSW mode propagation properties can be adapted. The propagation properties of the BSWs include, for example, the propagation length and the effective refractive index. Thanks to the low losses and the design of our multilayer platform, propagation lengths in the range of millimeter are obtained.

In a second part, 2D optical components fabricated in a 60 nm ( $\lambda/25$ ) device layer of  $\text{TiO}_2$  are presented, and initially, disk resonators. The latter are key elements in integrated optics systems. For a disk with a radius of 100  $\mu\text{m}$ , an experimental quality factor of the order of  $10^3$  is obtained.

A 2D Bessel-like beam generator is also studied. An isosceles triangle is used to generate such a beams. The main expected property of Bessel-type beams is their "quasi non-diffracting" nature. The optical properties of non-diffracting beams are measured in the near-field for different base/height ratios of the isosceles triangle. It is demonstrated that the beam propagates without significant spreading for considerable propagation distance, approximately 50  $\mu\text{m}$ .

Finally, the gratings engraved in a waveguide are studied. It is demonstrated that they perform as a Bragg mirror at wavelength,  $\lambda=1550$  nm. Thanks to the MH-SNOM, the interference fringes between the incident wave and the reflected wave are measured. The experimental reflectivity is obtained from the contrast of the interference fringes. The presented waveguide grating can be used as a Bragg reflector at telecom wavelengths for 2D optics systems.

**Key words:** Micro and nanostructures, Bloch surface waves (BSWs), near-field scanning microscope (SNOM), 2D optics, photonics, optics, near-field characterization, multilayer structures, surface electromagnetic waves.





# Résumé

Les ondes de surface de Bloch (BSWs) sont des modes électromagnétiques de surface qui se propagent à l'interface entre un substrat à couches multiples et un milieu externe homogène. Le champ optique du mode de surface est confiné près de la surface de la multicouche. Ce confinement vertical ainsi que la faible absorption inhérente aux matériaux diélectriques font des BSW un candidat intéressant pour le développement de systèmes optiques et de détecteurs 2D. Une telle structure multicouche périodique peut constituer une plateforme sur laquelle de nombreuses fonctions optiques peuvent donc être créées.

Dans cette thèse, des composants optiques à 2 dimensions basés sur la plate-forme à ondes de Bloch sont étudiés, en particulier : un résonateur à disque, un générateur de faisceau de type Bessel et un réseau de type comme un miroir de Bragg positionné sur un guide d'onde. Les propriétés optiques des composants telles que la résonance à l'intérieur du disque, le comportement "quasi non diffractant" et les propriétés de réflexion sont présentées. Les composants optiques 2D sont conçus à partir d'un programme FDTD commercial (CST Microwave studio). Ils sont ensuite caractérisés grâce à un microscope à balayage en champ proche à détection multi-hétérodyne (MH-SNOM). Grâce au MH-SNOM, il est possible de dresser une carte de la distribution du champ local à la surface des structures et ce, avec une résolution inférieure à la longueur d'onde. La mesure simultanée de l'amplitude et de la phase permet une reconstruction détaillée de l'amplitude complexe du champ électrique.

Dans une première partie, l'influence d'une couche superficielle de matériau de haut indice de réfraction ( $\text{TiO}_2$ ) est étudiée. L'impact d'un changement d'épaisseur de la couche de  $\text{TiO}_2$  sur les propriétés de propagation des BSWs est établie. Il est démontré qu'en adaptant l'épaisseur de la couche superficielle, la position de courbe de dispersion BSW peut être déplacée dans la bande interdite photonique et qu'en conséquence, les propriétés de propagation de mode BSW peuvent être adaptées. Les propriétés de propagation des BSWs incluent par exemple la longueur de propagation et l'index de réfraction efficace. Grâce aux faibles pertes et au design de notre plate-forme multicouche, des longueurs de propagation de l'ordre du millimètre sont obtenues.

Dans une seconde partie, des composants optiques 2D fabriqués dans une couche superficielle de 60 nm ( $\lambda/25$ ) de  $\text{TiO}_2$  sont présentés et pour commencer, des résonateurs à disque. Ces derniers sont des éléments clés dans les systèmes d'optique intégrés. Pour un disque de rayon 100  $\mu\text{m}$ , un facteur de qualité expérimental de l'ordre de  $10^3$  est obtenu.

Un générateur de faisceau 2D de type Bessel est également étudié. Cet élément consiste en un triangle isocèle. La propriété principale attendue des faisceaux de type Bessel est leur nature « quasi non-diffractant ». Les propriétés optiques de faisceaux non-diffractant sont mesurées en champ proche pour différents rapports base/hauteur du triangle isocèle. Il est démontré que le rayon se propage sans dispersion significative sur des distances au-delà de 50  $\mu\text{m}$ .

Enfin, des réseaux inscrits sur un guide d'onde sont étudiés. Leur propriété à former un miroir de Bragg autour de 1550 nm est démontrée. Grâce au MH-SNOM, les franges d'interférences entre l'onde incidente et l'onde réfléchie sont mesurées. La réflectivité expérimentale est obtenue à partir du contraste des franges d'interférences. Le réseau ici présenté peut être utilisé comme un réflecteur de Bragg aux longueurs d'onde de télécommunications pour des systèmes optiques 2D.

**Mots clé :** Micro et nanostructures, ondes de surface de Bloch (BSWs), microscope à balayage en champ proche (SNOM), optique 2D, photonique, optique, caractérisation en champ proche, structures multicouches, ondes électromagnétiques de surface.



# Content

<b>CHAPTER 1 INTRODUCTION.....</b>	<b>12</b>
1.1 Bloch Surface Waves .....	12
1.2. Surface Plasmons Politrons (SPPs) - State of art.....	15
1.2.1 2D Bragg mirror .....	15
1.2.2 Non-diffracting plasmonic beams.....	16
1.2.3 Plasmonic resonators .....	17
1.2.4 Plasmonic waveguides .....	17
1.2.5 Plasmonic Lens.....	18
1.2.6 Plasmonic Interferometer.....	18
1.3. Tamm plasmonic surface states .....	19
1.4. Beyond diffraction limit – Near-field imaging technique.....	20
1.4.1 Scanning near-field optical microscopy .....	20
1.4.2 Multi-heterodyne Scanning near-field optical microscopy (MH-SNOM).....	22
1.5 Contribution notification .....	27
1.6 Thesis outline .....	28
<b>CHAPTER 2 REVIEW ON BSW .....</b>	<b>31</b>
2.1. 2D polymeric gratings.....	31
2.2. Polymer ridges- BSW based waveguide sensor .....	32
2.3. Refraction of BSWs/Ultrathin ridge waveguides .....	33
2.4. 2D Plano convex Lens .....	35
2.5. 2D Prism and Gratings.....	36
2.6. 2D waveguide grating coupler.....	37
2.7. BSW based sensors – A proof of principle.....	39
2.8. Fluorescence emission enhancement by BSW platform .....	40
2.9. Bloch surface waves based bioprobes - Lab-on-fiber technology .....	41
2.10. On-chip phase-shifted Bragg grating for spatial differentiation of Bloch surface wave beams.....	43

2.11. Bloch-like surface waves in quasi-crystals and aperiodic dielectric multilayers .....	45
2.12. Theoretical study of Bloch surface waves ring resonators .....	46
2.13. Slow light Effect – Bloch Surface Waves .....	47
2.14. Grating coupler for Bloch surface waves .....	49
15. Tunable Bloch surface waves - lithium niobate thin films .....	49
<b>CHAPTER 3 PROPAGATION PROPERTIES OF BLOCH SURFACE WAVES .....</b>	<b>52</b>
3.1 Constituent material and multilayer platform design concept .....	53
3.2 Experimental set up for Bloch surface wave excitation and characterization methods .....	59
3.3 Impact of device layer on Bloch surface waves propagation properties .....	62
3.3.1 Propagation length analysis .....	62
3.3.2 Analysis of evanescent field in external medium .....	67
3.3.3 Effective refractive index analysis .....	68
3.4 Conclusion .....	72
<b>CHAPTER 4 BLOCH SURFACE WAVES BASED 2D DISK RESONATOR .....</b>	<b>75</b>
4.1 Fundamental concept of optical resonator .....	76
4.1.1 Quality factor (Q factor) .....	77
4.1.2 Free-Spectral Range (FSR) .....	77
4.1.3 Finesse .....	78
4.1.4 Waveguide coupling regimes .....	78
4.2 Simulation Results .....	79
4.3 Design concept .....	81
4.4 Fabrication technique .....	82
4.5 Near Field characterization .....	83
4.6 Conclusion .....	90
4.7 Appendix .....	91
<b>CHAPTER 5 BLOCH SURFACE WAVES BASED 2D BESSEL-LIKE BEAM GENERATOR .....</b>	<b>93</b>
5.1 Design concept and fabrication .....	95
5.2 Near-field measurement results and discussion .....	96
5.3 Conclusion .....	105

<b>CHAPTER 6 BLOCH SURFACE WAVES BASED 2D BRAGG MIRROR .....</b>	<b>107</b>
6.1 Design concept and fabrication .....	108
6.2 Near-field characterization.....	109
6.3 Conclusion.....	116
<b>CHAPTER 7 CONCLUSION AND FUTURE PROSPECTS .....</b>	<b>118</b>
<b>LIST OF ABBREVIATIONS .....</b>	<b>123</b>
<b>BIBLIOGRAPHY .....</b>	<b>126</b>
<b>ACKNOWLEDGEMENTS .....</b>	<b>135</b>
<b>LIST OF APPENDICES.....</b>	<b>138</b>
A. Publications and Conferences .....	138
B. Curriculum vitae .....	140





# CHAPTER 1

## Introduction

The motivation behind this thesis is a dielectric multilayer platform which sustains Bloch surface waves at the interface with external medium. This platform consists of a periodic stack of dielectric material which are easily available in semiconductor industry and coating technology. The platform is well known in sensing. However, we exploit it in the field of two-dimensional optics. The optical components can be produced on the top of this platform using standard patterning techniques such as e-beam writing or optical lithography. The surface waves interact with optical components. To observe this interaction we use scanning near-field microscopy. This is the most efficient tool to directly access the surface mode spatial distribution since a Bloch surface mode is bounded close to the surface of the multilayer platform and decays evanescently in the external medium which is air in our case.

In this chapter, we mainly emphasize the advantage and motivation of Bloch surface waves (BSWs) in comparison to other known surface waves to highlight BSWs as a more suitable candidate for two-dimensional (2D) optics. We begin with a brief introduction of Bloch surface waves followed by the advantages of BSWs based 2D optics. Later, we present the state of art of surface plasmons based 2D optics and scanning probe near-field optical microscopy. The fundamental feature and functioning of multi-heterodyne scanning near field optical microscope is presented. The thesis outline and contribution notification are presented at the end of this chapter.

### 1.1 Bloch Surface Waves

In 1978, Bloch Surface Waves on the surface of periodic dielectric multilayers were first time experimentally studied by Yeh, Yariv and Cho [1]. The Bloch surface waves are surface electromagnetic modes, which can be coupled at the interface of truncated dielectric periodic

multilayers and external medium at particular illumination condition. The electromagnetic field in the layered media has a form [1]

$$E(z, y, t) = E_k(z) \exp(iKz) \exp(i(\beta y - \omega t)) \quad (1.1)$$

Where,  $z$  axis is a normal to the air interface and  $E_k(z)$  is a periodic function of  $z$  with period equal to the period of multilayers, as shown in Fig.1.1.  $K$  and  $\beta$  are propagation vectors in  $z$  and  $y$  directions, respectively.

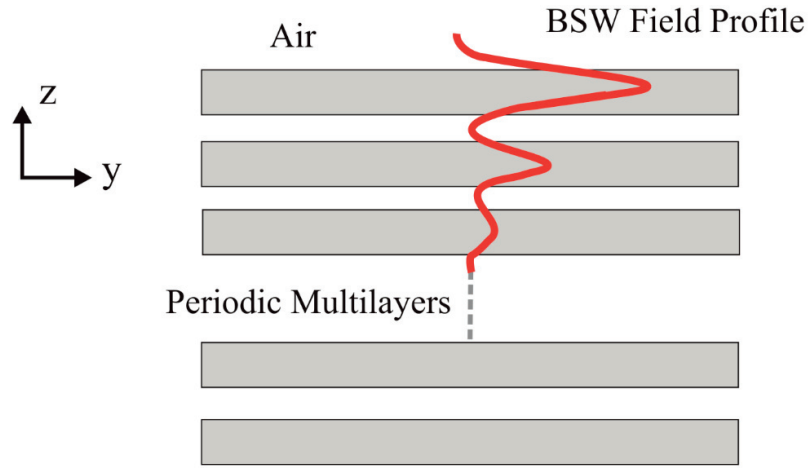


Fig.1.1. The schematic of BSW field distribution in transverse direction. The image shows exponentially decay inside air and multilayers.

At a given frequency, there are regions of  $\beta$  for which  $K$  is complex,

$$K = m(\pi/\Lambda) \pm iK_i \quad (1.2)$$

Where  $m$  is a positive integer and  $\Lambda$  is a period of the multilayers. If the periodic medium is finite, the solutions (Eq.1.1) with exponentially decaying field variation exist in side the forbidden band gap. The electric field amplitude is interpreted as an exponential decay in the homogeneous

medium (external medium) and as a standing wave with an exponentially decaying envelope  $\exp(-K_i z)$  in the periodic medium. Hence, the electric field is confined close to the interface of the multilayer. This vertical confinement makes BSWs a perfect candidate for the design of in-plane/two-dimensional (2D) integrated optics systems and sensors. The primary benefit of this in-plane approach leads to a relaxed fabrication of arbitrary shapes in comparison to standard three-dimensional (3D) integrated photonics structures. 2D optical elements can be produced and used in few other ways. One is absolutely elucidated by the use of wave guiding media wherein the light is confined and propagated inside a sandwiched structure. However, in case of slab waveguides, the light is almost completely buried in the inner layers of the waveguide. So it is almost impossible to carry out its direct spatial mapping. Besides waveguides, another way for 2D optics is represented by surface plasmon polaritons (SPPs) on smooth planar or structured metallic films [2], [3]. Surface Plasmons are electromagnetic waves excited on the proper metallic – dielectric interface, which have maximum electric field at the interface (on the top of metallic film) and are evanescent away from it. Surface Plasmons are studied extensively in past years and they have strong background in 2 D optics. In the next section, the literature about surface plasmons based 2D elements have been presented. However, because of high absorption losses of metals, SPPs 2D components limit their performance in terms of propagation losses.

The dielectric multilayer based BSWs have several advantages in comparison to that metallic layer based SPPs which make BSWs as a possible alternative to SPPs and a potential candidate for 2D optics. Some of them are following:

- ✓ For a particular wavelength range, dielectric material can be chosen with very low intrinsic losses. Hence, propagation length of BSWs are longer than SPPs. The propagation lengths of SPPs are limited by absorption in metal. Low losses corresponds to narrow reflection dip for sensing applications, which might increase the sensitivity in sensing application [4], [5].
- ✓ Multilayers are wavelength scalable and may be designed to sustain BSWs at a relatively broad range of wavelength from IR to near-UV, provide dielectric materials are transparent to desired wavelength range [4] .
- ✓ Multilayers are compatible for both TE and TM polarization based on initial design, while SPPs can be excited only with TM polarization. It has been stated in recent work that both TE and TM polarized BSWs can be excited simultaneously with superimposing locations in the dispersion band diagram in a particular multilayer design [6]. On the other hand SPPs can only be excited for TM polarization.

- ✓ The position of the surface mode within the forbidden band gap can be engineered as well by tailoring the top layer of the multilayer. BSW modes, located close to the center of the band gap are shown to be more localized, leading to significantly higher surface electromagnetic fields than modes located near the band edge [7]. Because it allows the segregation between the volume and the surface contributions from a sample. This is very appealing ability for sensing applications [8].
- ✓ The fabrication of a multilayer is fully compatible with the actual fabrication technologies of integrated photonic structures.

Considering the above mentioned advantages, in this work we present BSWs based multilayers as a platform for 2D optics. The main advantage of the platform concept is that the fabrication of thin film multilayers enables the wafer scale fabrication using standard plasma enhanced chemical vapor deposition (PECVD) technique. And further, the topmost layer can be structured to pattern 2D micro-optical components using patterning techniques such as e-beam writing and photolithography. To observe the interaction of surface waves with 2D structures on the top of multilayer platform and to characterize optical components we utilize Multi-heterodyne Scanning near-field optical microscopy (MH-SNOM), which is explained in section 1.4 of this chapter.

## 1.2. Surface Plasmons Polaritons (SPPs) - State of art

As discussed before, Surface plasmons polaritons are bounded states between metallic and dielectric interface. SPPs have been studied extensively in the domain of 2D optics. In this section we present the literature survey of 2D optics on surface plasmon polaritons. Different optical components have been presented and discussed in brief.

### 1.2.1 2D Bragg mirror

Jean-Claude Weeber et al. have studied first the 2D surface plasmonics Bragg mirror theoretically and experimentally [9]. The microgratings were engraved into subwavelength range wide metal ridge surface plasmon waveguides. A focused ion beam has been used to engrave microgratings into a 2.5  $\mu\text{m}$  wide gold waveguide. They used photon scanning tunneling microscopy to observe near-field distributions of the field around these structures. He has shown experimentally that finite length periodic arrangement of narrow slits can reflect a surface plasmon mode propagating along

a surface plasmon waveguide. It has been also demonstrated experimentally that the reflection efficiency of the micrograting is found to depend upon the, period of the grating, number of slits, and the illumination wavelength. They found the optimum reflection efficiency for a period of the micrograting equal to half the incident wavelength in vacuum. The reflection coefficient is deduced from the contrast of the interference fringes generated because of the interference of incident and back reflected light. The reported measured contrast at the Bragg wavelength is around 0.26 and the calculated reflection coefficient from the computed standing wave is equal to 25%. Therefore, they have demonstrated experimentally that microgratings engraved in a surface plasmon waveguide can perform as a Bragg mirror for properly designed microgratings. However, they discussed that the reflection efficiency of the mirror saturates for rather lower number of 10 slits. This is because of the dramatic damping of propagating surface plasmons through the microgratings. The metal absorption losses limit the reflection efficiency of the presented 2D plasmonic Bragg mirror. Bragg reflectors have been further studied by other groups [10], [11].

### 1.2.2 Non-diffracting plasmonic beams

Jiao Lin et al. have studied (theoretically and experimentally) a new kind of plasmonic surface wave, cosine-gauss beam, which propagates in a straight line (does not diffract) and remains tightly confined to the surface until up to 80  $\mu\text{m}$  [12]. These beams have been named as Localized long range non-diffracting surface plasmons. To map the two-dimensional SPP field distribution, they used a near-field scanning optical microscope working in the aperture mode which collects the in-plane field components. They have shown that the generation of these kind of waves is very straightforward and controllable in terms of transverse confinement and directionality. These beams can be generated by fabricating a plasmon launcher consisting of overlapping/non-overlapping metallic gratings. The constructive interference of two tilted plane waves propagating in phase along the symmetry axis results in a straight propagation of these non-diffracting beams. The results shows that the beam maintains its focus until a propagation distance of 80  $\mu\text{m}$ . This was one of the techniques to overcome the propagation losses of surface plasmons and achieve long range propagating plasmonic waves (80  $\mu\text{m}$ ) to be served as an optical interconnect in integrated optics. Because of their unique properties, these highly localized and non-diffracting beams find potential application in optical tweezing and optical interconnects. Later, Cesar E. Garcia-Ortiz and et al. has studied experimentally the generation of diffraction-free plasmonic beams utilizing SPP excitation by metal ridges at normal illumination [13]. The results shows transverse confinement of the order of one wavelength. The self-healing properties of the diffraction-free plasmonic beams, when beam encounter an obstacle along the propagation axis, have been demonstrate experimentally.

### 1.2.3 Plasmonic resonators

The resonator based on surface plasmon-resonance have been studied rigorously in the past for sensing applications for the optical detection of small chemical and biological entities. Sergey I. Bozhevolnyi et al. have studied the low propagation loss channel plasmon subwavelength waveguide ring resonators [14]. Keeping the problem of achieving sufficiently low propagation loss for practical applications with strong confinement, they opted for the approach to investigate subwavelength waveguide components based on channel plasmon polaritons. The channel plasmon polaritons are electromagnetic waves that are bound to V-shaped grooves milled in a metal film and propagate along the bottom of grooves. These modes are expected to exhibit relatively low propagation loss and subwavelength confinement. In their paper, they have experimentally realized ring resonators based on this approach with subwavelength V-shaped grooved waveguides. For the ring of 5  $\mu\text{m}$  radius, the measured quality factor is approximately 38 at telecommunication wavelengths.

Efforts are put on the improvement of the quality factor of the structure which is one of the main measures of the efficiency of ring/disk resonators. In the same direction, the ring resonators with hybrid waveguide consisting of a dielectric nanowire on a silver layer have been studied [15]. The advantage of surface plasmon based resonators is the strong confinement of the electric field which provides a footprint in the range of micrometer. However, because of the high absorption losses of metals, plasmon based resonator sensors suffer from very low quality factors, which limits the sensitivity of the device.

### 1.2.4 Plasmonic waveguides

For SPP based photonics devices, there are two types of fundamental waveguide structures: the insulator-metal-insulator (IMI) waveguide and the metal-insulator-metal (MIM) waveguide [16]. The IMI waveguide provide low losses and longer propagation lengths, however they suffer from poor ability to confine light into subwavelength scale which is not good for chip level integration. On the other hand a MIM waveguide has shown the ability of subwavelength manipulation and having acceptable propagation lengths, therefore seeking more attention towards implementation of future integrated systems. In the recent years, different kinds of plasmonic waveguide structures have been emerged. For example, coupled nanowires [17], metallic strips and nanowires [2] [18], metal-insulator-metal (MIM) waveguides [19], metallic grooves[20], dielectric-loaded plasmonic waveguides[21], as well as hybrid plasmonic waveguides [22]. Because of the best trade-off

between the propagation loss and the field confinement, hybrid plasmonic waveguides have drawn substantial research interest.

### 1.2.5 Plasmonic Lens

Zhaowei Liu et al. have investigated plasmonic lens theoretically and experimentally. They have shown that circular and elliptical structures milled in a metal film can behave as a lens [23]. The surface plasmons are launched with circular or elliptical slits. The propagating plasmons interfere and concentrate the electromagnetic field at the focal point. Another group studied focusing of surface plasmons with the arc shaped hole array fabricated into 50 nm thick Ag film [24]. It has been shown that SPP can be focused into an intense spot with subwavelength width. Further they have also shown the coupling of focused spots into metal strip waveguides. The combination of lens and the waveguide may serve as a basic element of 2D nano-photonics circuits. The near-field observation has been performed with the aid of near-field scanning optical microscopy.

### 1.2.6 Plasmonic Interferometer

A Mach–Zehnder interferometer employing surface plasmon polaritons was first studied theoretically by Zhanghua Han et al. The interferometer is designed by combining two identical optical directional coupler in MIM waveguide geometry [25]. The control of output power by changing the length of coupling region has been studied numerically. Later, Sergey I. Bozhevolnyi et al. have presented experimental demonstration of plasmonics Mach–Zehnder interferometer [14]. The presented design takes the advantage of low bending losses because of subwavelength confinement provided by V-grooved waveguide geometry, which has been discussed in the plasmonic resonator section. However, the output transmission remains limited to lower values because of metal damping.

We have summarized the intensive studies done on basic elements of plasmonic based 2D optical systems. They provide potential advantage of having a foot print of optical components in the range of micrometers. However metal absorption has unfavorably affected the performance of the 2D components in terms of propagation losses.

### 1.3. Tamm plasmonic surface states

There are other known surface waves, named Tamm plasmons (TP) [26] [27]. They are named in the analogy with the electronic states at a crystal surface proposed by Tamm. TP electromagnetic modes are confined at the boundary between a homogeneous medium with negative dielectric constant (normal metal below the plasma frequency) and a dielectric multilayers (Bragg Mirror). Similar to the BSWs, the confinement inside multilayers is achieved because of the photonic stop band of the Bragg mirror whereas confinement inside the metal is provided by its negative dielectric constant. They may exist for both TE and TM polarization states same as BSWs.

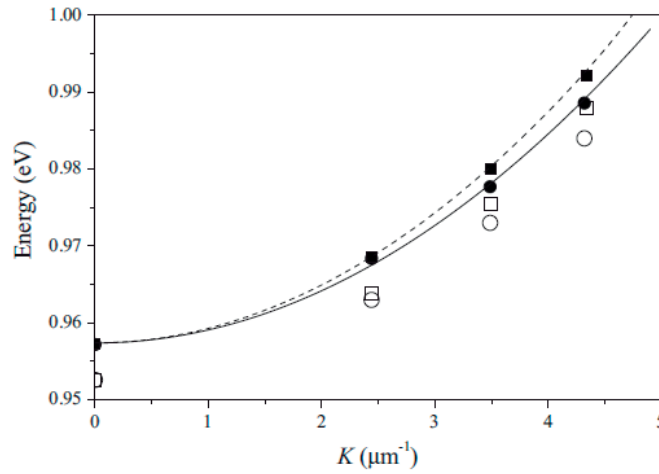


Fig.1.2. The dispersion curve of Tamm plasmons at the interface between a semi-infinite Bragg reflector (GaAs/AlAs layers) and a semi-infinite gold layer for the TE and TM polarization states represented by solid line and dashed line respectively [26].

The BSWs and SPPs can only be excited when wave vector matching condition is fulfilled which necessitates the use of prism or diffraction grating coupling. The approach of using a separate excitation system might not be convenient in a specific experimental or device applications. The TP modes take advantage here because they can be excited with normal incidence. As their dispersion curve lies within the light line and they can have a zero in-plane wave vector, therefore they can be produced by direct optical excitation (normal incidence), see Fig.1.2, [26]. The TP modes are characterized by a parabolic dispersion, as shown in Fig.1.2. This feature makes TPs an example of slow propagating photonics states which can be utilized for engineering optical slow light devices.



## 1.4. Beyond diffraction limit – Near-field imaging technique

We observe the magnified image of the object in conventional microscopy. The magnification is performed using a lens or a system of lenses. When the incident light interacts with the object/structure, it generates propagating and non-propagating field components in the vicinity of the sample. The non-propagating components carries the highly detailed features remains very close to the interface (near-field) of the structure, while propagating components reaches the imaging lens (far-field) and construct the image. The conventional microscopy imposes the Abbe's far-field diffraction limit which defines that the structures with lateral dimension larger than  $d_{min} = \lambda/2n\sin\theta$  can be imaged with accuracy, chapter 1<sup>st</sup> [28], where  $\lambda$  is the wavelength of the illuminating light,  $n$  is the refractive index of the medium in which the sample is placed and  $\theta$  is the aperture semi-angle of the imaging system. The resolution limit is only slightly smaller than the wavelength of illumination light. Therefore, for the subwavelength resolution the imaging system should be able to capture the evanescent field containing high spatial frequencies and present in the immediate vicinity of structure only.

Scanning near-field optical microscopy (SNOM) is a near-field optical imaging technique with a resolution beyond diffraction limit. It was born in 80's. There was a continuous development in the capabilities and performance of technique in later 30 years since it was invented. The capabilities of studying the optical phenomenon at nanoscale and characterizing photonics devices based on nanostructures have made SNOM an invaluable near-field imaging tool. In the subsequent section the overview of development of SNOM has been provided.

### 1.4.1 Scanning near-field optical microscopy

After the invention of Scanning Tunneling Microscope (STM) [29] and Atomic Force Microscope (AFM) imaging [30] techniques in early of 1980's, first Scanning Near-field Optical Microscope (SNOM) at a visible wavelength has been realized by D. Pohl from the IBM Ruschlikon Research Laboratory in 1984. He has shown image recordings with a resolution of  $\lambda/20$  [31] which is beyond the Abbe's far field diffraction limit. The SNOM uses AFM techniques, where nano-metric distance between probe and sample surface is controlled by inter-atomic forces, to position the probe close to the surface of the sample in order to detect the optical near-field.

SNOM probes can be operated in collection mode or in illumination mode as a subwavelength sensor or subwavelength emitter, respectively, or as both (in collection/illumination mode) [32], [33]. In our case the tip of the probe is used in collection mode. It collects the evanescent field

when the sample is illuminated in total internal reflection. The probe is very important part of SNOM. Indeed, the resolution and the quality of optical images are strongly depending on the type of the probe. There are different types of probes that exist. The types are defined by the method of probe production/fabrication. The tapered optical fiber is the simplest one. It provides an aperture size around 100 nm.

Furthermore, a coating of thin metal layer can be deposited on the probe in order to better define a small aperture. The metal coating provides the advantage of significantly suppressing unwanted background signals by reflecting spurious scattered light.

The SNOM is an important tool for many research domains in optics. The development of SNOM has made it possible to find the applications in different domains, which include biomedical field, surface chemistry, imaging surface at atomic level to study single molecule, sensing and 2D integrated optics. Nowadays, as SNOM opens up new ways to study different research fields, there is growing interest in investigating nanostructures, photonics devices, microsystems and characterizing 2D optical components on metallic or dielectric layers. To study the nanostructures thoroughly, for example to investigate the novel optical phenomenon appeared when light interacts with these elements, the amplitude, phase and polarization of the interacting light should be observed. These observations are not possible with conventional SNOM as it provides information only about field intensity. Phase contains very important information about refractive index, effective wavelength and direction of light propagation. Therefore, it can be said that with a conventional SNOM, the complete information of the specimen under study cannot be obtained. The phase measurement is one of the major concerns of interferometry.

The interferometry can be divided into two categories- quasi heterodyne interferometry and heterodyne interferometry [34]. Both of them are based on phase shifting techniques. In quasi heterodyne interferometry, the phase shift between two arms of interferometer is introduced in steps, using at least three different values. This techniques is good for moderate phase resolution ( $\lambda/100$ ). The image of two-dimensional interference pattern can be recorded and phase can be deduced at any point of the image. However, in heterodyne interferometry the step wise translation of phase shift is replaced with continuously increasing phase shift. This technique leads the phase resolutions up to  $\lambda/1000$  [35].

Further, heterodyne SNOM has been developed where amplitude and the phase of the light can be obtained simultaneously [36]–[38]. The images recoded with a heterodyne SNOM provide better understanding of the optical phenomenon.

## 1.4.2 Multi-heterodyne Scanning near-field optical microscopy (MH-SNOM)

In this section, we present the building blocks of MH-SNOM and its working principle in the consecutive sub sections.

### 1.4.2.1 MH-SNOM Setup

All the near-field experimental results presented in this thesis are obtained with the aid of the presented MH-SNOM. This near-field imaging tool was built in our lab (EPFL-OPT). The setup of MH-SNOM consists of following five building blocks. Each of them is described briefly in this section.

#### a) Optical interferometer

In this section, we describe the prominent part of MH-SNOM, the optical interferometer as shown in Fig.1.4. This is an all fibered setup. The yellow and blue fiber paths represent single mode fiber (SMF) and polarization maintaining fiber (PMF), respectively. The entire optical system is enclosed with plexiglass boxes to protect from air currents and lied on the vibration isolated table. This table has a pneumatic legs filled with compressed air. In addition, all the optics except SNOM head is covered with 6 cm thick polyurethane foam pads. The SNOM head will be described in this section later. This protection is to attenuate the acoustic vibrations and to slow down the thermal energy transfer.

The laser source used in the experiments is an external cavity tunable laser from Agilent technology (*Model 81682A*). The wavelength range of the tunable laser is 1460 nm to 1580 nm which can be produced with an accuracy of 10 pm. The output power of the laser can be stabilized at a particular desired value. The range of output power depends on the range of wavelengths. For 1460 – 1480 nm: the output power is greater than 1mW, for 1480 – 1520 nm: the output power is greater than 2.8 mW, for 1520 – 1580 nm: the output power is greater than 5.6 mW. The coherence length of the laser inside fiber medium is 640 m. The laser is mode hope free for the full range of wavelengths and output is linearly polarized in PMF.

The four different acousto-optic modulators (AOMs) are used to shift the object and reference channels to different frequencies. The AOMs (*IntraAction, Model FCM- 401E5C*) independently generate frequencies  $f_1$ ,  $f_2$ ,  $f_3$  and  $f_4$ , as shown in Fig.1.4. When these four frequencies from reference and object channels are combined to each other, they produce six beat frequencies among

which two are generated as a consequence of self-beating of object and reference channels. These two signals can be used to check the orthogonality of the beams.

Finally, the field at the sample is collected by a fiber probe (in collection mode). This commercialized probe (*Lovalite, Model E50-SMF28-AL70-200*) has an aperture diameter of 200 nm. The probe is coated with 70 nm thick aluminum layer to well define the aperture and also to reflect back the undesired scattered light. These are the only probes used in this work. The field collected by the probe is mixed with the reference signal and then superimposition of these four signals is sent to the detector. The detection system includes detector (*aboptic, Model DG100*), splitter and lock-in amplifiers (*Stanford Research, Models SR530 and SR830*).

The detection system consists of InGaAs photodiode (*Fermionics, Model FD100-FC*). The pass band (-3 dB) of the detector is 7.5 MHz which is well above the beat frequencies (<100 KHz) [39].

#### **b) Data acquisition**

Data acquisition includes the simultaneous data collection from significant number of signals from lock-in amplifier and other devices (piezo sensors and SNOM electronics). The Z motion of the probe is controlled by a commercial SNOM (shear-force feedback) software which is driven by one computer. However, a separate independent computer is used for X and Y motion control of probe and data acquisition. The probe motion is described in the next section. The data acquisition and X and Y probe motion control is performed by purpose-build software. This software has been developed in LabVIEW programming language. The flow chart explaining working principle of the software can be found in detail somewhere else [39].

#### **c) Probe motion**

The three dimensional probe motion is controlled by an XYZ piezo stage (*Physik Instrumente, Model P-517.3CL*). The movement range of X-Y and Z piezo stages are  $L_{x-y} = 100 \mu\text{m}$  and  $L_z = 20 \mu\text{m}$  respectively. The repeatability of the travel range of X-Y and Z stages are  $\pm 5 \text{ nm}$  and  $\pm 1 \text{ nm}$  respectively. The piezo actuator works on the principle of producing mechanical expansion or compression with the application of electric voltage. The piezo driven voltage and the movement of the actuator follows the relation: for the X, Y actuators,  $1 \text{ V} = 10 \mu\text{m}$  and for the Z actuator,  $1 \text{ V} = 2 \mu\text{m}$ . The X-Y and Z motion of the piezo state is driven by two independent computers as described in the previous section.

In the Z motion control, the feedback system is governed by the resonance frequency of the probe sensor (tuning fork + probe). The commercial system (*APE Research*) that drives the Z motion finds the resonance frequency of the sensor. Further the preamplifier determines the electric field amplitude of the probe sensor oscillations. The fraction of the peak oscillation amplitude (typically 95%) is set as a reference point for PID (Proportional Integral Derivative) feedback controller system.

When probe approaches to the surface of sample, the resonance frequency of the probe is deviated from the natural frequency due to interaction with inter-atomic forces. This leads to drop down the resonance amplitude. The interaction range of the probe and sample surface is 1 - 100 nm depending on the type of probe and specific experimental conditions for implementation, chapter 7<sup>th</sup> [40]. Further, the feedback system works on the Z piezo in order to maintain the sensor oscillation at the reference point. This way the probe maintains a constant distance from the sample surface and follow the topography of the surface structure. The piezo actuators provide the fine movement of the probe. However, for the course movement of the probe DC XYZ stepper motors have been installed which are driven by commercial SNOM system.

#### **d) SNOM head**

The SNOM head is a housing for the piezo stage. The piezo stage only provides nano metric movement to the SNOM probe. To approach the sample some additional mechanism is needed which can bring the sample and probe close enough to be in the range of nano metric movement of piezo stage. For this arrangement the illumination system and the sample are placed on the lab jack, as shown in Fig.1.3. Further, the piezo stage is fixed on the motorized stage (DC stepper motor) which provides course movement of probe in X, Y and Z direction. The motorized stages are hanged on a thick aluminum plate which is supported by three pillars, see Fig.1.3. The advantage of the lab jack is that it can support experimental set up which requires heavy and cumbersome apparatus. The probe sensor (tuning fork + probe) is built on yellow circuit board which is connected to pre -amplifier. A manual translational stage is fixed to yellow circuit board which is attached to the piezo stage.

Finally, to approach the sample to the probe takes few steps. In the first step, we lift the lab jack up until the sample is sufficiently close to the probe. Then, the coarse approach is carried out by employing translation stage holding the probe sensor. In the final step, the fine approach is realized by performing iterative trials of the Z motorized stage and vertical piezo stage.

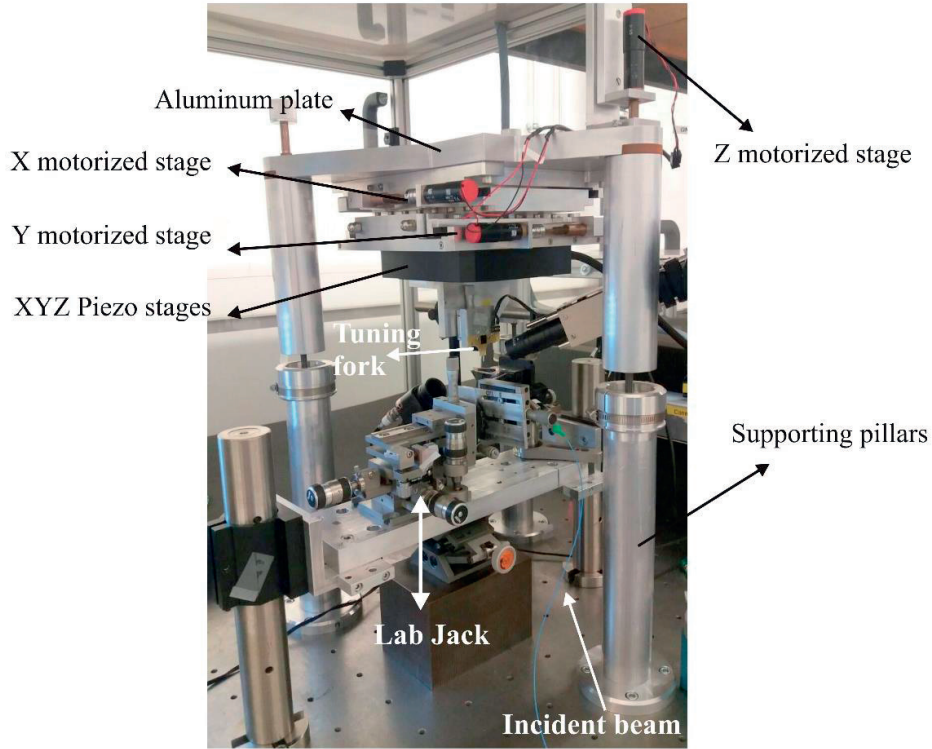


*Fig.1.3. Picture of the SNOM head demonstrating Piezo and motorized stages for the probe motion, tuning fork, lab jack and supporting mechanism.*

### 1.4.2.2 MH-SNOM Working Principle

In the present work, Multi heterodyne SNOM (MH-SNOM) is used to observe and measure the interaction effects of Bloch surface waves (BSWs) and 2D structures. This is an upgraded version of the classical heterodyne SNOM. Unlike heterodyne interferometer, object and reference beams are further divided into two orthogonally polarized object and reference beams, respectively. First, the laser beam is sent to a polarization controller before passing through a polarization beam splitter (PBS). The purpose of the polarization controller is to adjust the ratio of object and reference power at the output of the polarization beam splitter (PBS). Each of these beams are splitted again using 50/50 beam splitter (BS). The frequency in each of the four channels is then shifted to a different frequency. These frequencies are generated by Acousto-optic modulators (AOMs). Two object beams are recombined by the mean of a PMF (polarization-maintaining fiber) while the reference beams are recombined into SMF (Single mode fiber) with PBS. The state of polarization of illumination beam (TE or TM) can be controlled by rotating PMF. As the orthogonality and



linearity of the reference beams are well preserved up to the detector, they provide a basis ( $\hat{x}$ ,  $\hat{y}$ ) for the projection of the object beams in the detection plane. Two object and two reference beams are then recombined into SMF with a beam splitter of splitting ratio 99/1 (99% of object signal is coupled with 1% of reference signal because the signal collected by SNOM probe is very weak). The superposition of four different frequencies (two object beams, two reference beams) on the detector generate six different beat frequencies. These different beat frequencies can be detected with the help of lock-in amplifiers. Each of them is locked to the corresponding beat frequency. Among these six beat frequencies two beat frequencies are produced due to self-beating of reference-reference and object-object beams. These two beat frequencies can be used to check the orthogonality of the beams. The Schematic of MH-SNOM is shown in Fig.1.4.

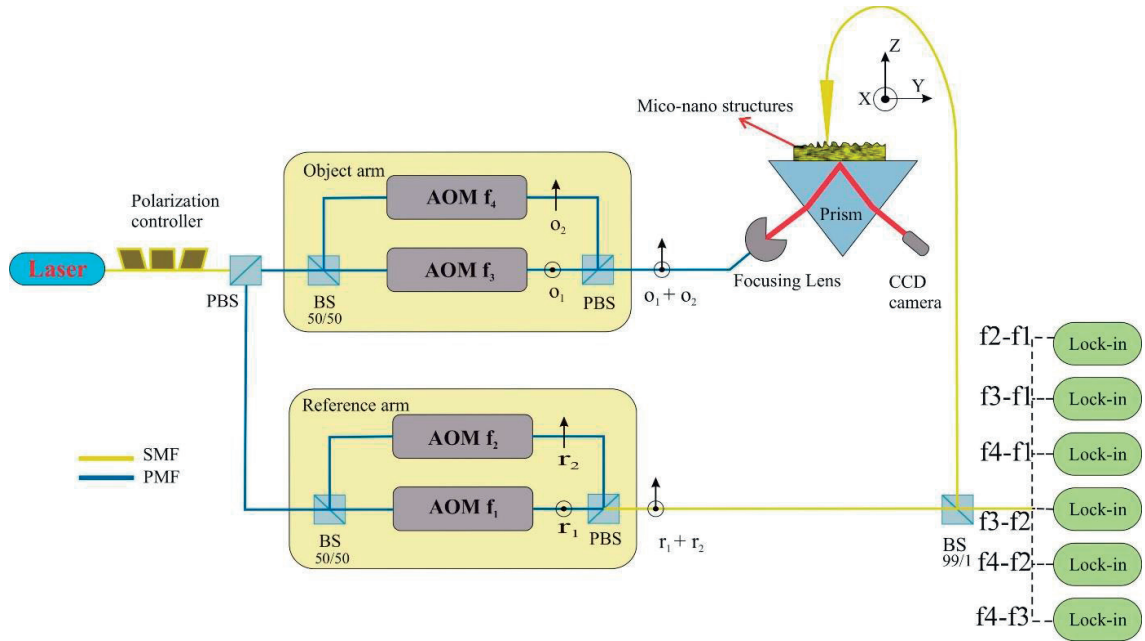


Fig.1.4. Schematic diagram of Multi-heterodyne SNOM (MH-SNOM) with four channels where object and reference arms are further divided into two orthogonally polarized object and reference beams. (AOM: Acoustic Optic Modulator, SMF: Single Mode Fiber, PMF: Polarization Maintaining Fiber, BS: Beam Splitter, PBS: Polarizing Beam Splitter).

MH-SNOM provides the flexibility to be used in different configurations for different applications. For example, if only one of the object (e.g.  $o_1$ ) and reference arms (e.g.  $r_1$ ) is implemented. In this case, two beams are combined and the projection can be detected by one lock-

in amplifier. This configuration can be simply referred as a heterodyne SNOM. The amplitude and phase of the one of the components of the object field can be obtained. However, if another reference arm (e.g.  $r_2$ ) is added, the projection of object beam on the two orthogonal reference basis can be detected. Hence, the amplitude and phase difference of the two components of the object field are obtained. Therefore, we retrieve the state of polarization of object field. This step is not direct. A SNOM simultaneously measures the amplitude and phase of two arbitrary orthogonal components of near fields. And then using a numerical approach, based on priori information about the field distribution, the field at the sample surface ( $E_x$ - $E_y$  components) can be retrieved. This configuration is addressed as Multi-heterodyne SNOM. Most of the work in this thesis has been performed using this configuration. Further, if another arm (e.g.  $o_2$ ) is added in the object channel, the simultaneous field response of the TE and TM state of polarization of the illumination beam can be obtained on the surface of the sample (see Fig.1.4).

In summary, conventional SNOM provides the intensity information while amplitude and phase can be obtained simultaneously using heterodyne SNOM. Moreover, MH-SNOM provided advantages as compared to simple heterodyne-SNOM. First, in MH-SNOM, the object signal is measured integrally because the basis (reference arm) is orthogonal. If the object signal does not interfere with a particular reference then the heterodyne signal will be maximum in the other reference. Second advantage in comparison to heterodyne SNOM is that: MH-SNOM enables the polarization resolved measurements. Third advantage lies in the simultaneous detection of the sample response to two orthogonal state of polarization (TE/TM) of the illumination beam. This feature can be used in particular applications when the sample has a specific response to one of the polarizations, then the other polarization can be used as a reference. This feature can find applications in florescence or to selectively excite different modes in waveguides [41].

## 1.5 Contribution notification

The transfer matrix code is written by Dr. Elsie Barakat of the OPT laboratory. The design concept of the 2D Bessel beam generator is proposed by Dr. Myun-Sik Kim of the OPT laboratory.

The fabrication of the multilayers is done in collaboration with the OPT laboratory members. Furthermore, we collaborate with Prof. Matthieu Roussey from the University of Eastern Finland for the fabrication of 2D optical components.



The thesis is structured to emphasize upon mainly my contribution.

- ✓ Different materials to be used as a device layer for optical components are studied. And the key optical properties of BSWs are investigated for different thicknesses of the device layer.
- ✓ Various optical components are studied and designed. To design the optical components simulations using CST microwave studio (Finite-difference time-domain (FDTD) method) are conducted. The near-field measurements of the optical components with the aid of MH-SNOM, experimental investigations and data analysis are performed.
- ✓ Experimental measurements involve dealing with the challenges of operating complex MH-SNOM.

**Remark:** During the relocation of the OPT laboratory, myself with Dr. Elsie Barakat were responsible for the transfer of the MH-SNOM to the new lab location. It involved disassembling of the complex system which consists of different optical, electronic and mechanical components and assembling the complete set-up with the proficiency to be able to perform near-field experiments again. This transferring process took around 6 months of the time period of my PhD duration.

## 1.6 Thesis outline

This thesis is composed of seven chapters. A brief summary of each chapter is given below.

In **Chapter 2**, the brief review of the study done in the BSW domain is presented. The chapter includes literature survey of BSW based devices for 2D optics and sensing studied by different research groups around the world. This chapter provides the knowledge and understanding of different aspects which have been investigated in BSW domain and how BSW can be exploited to design novel planer/integrated devices in future.

In **Chapter 3**, the design concept of the multilayer platform is studied. Further, the effect of different thicknesses of the device layer is demonstrated on BSWs properties, such as propagation length and effective refractive index. The results are compared in the near-field, far-field and in theory. The experimental and simulation results show a good agreement with each other. The concept of using the device layer of a specific thickness in order to design an application oriented multilayer platform is presented.

In **Chapter 4**, the first experimental demonstration of the BSW based resonator is presented. The chapter includes the fabrication technology and design concept of a disk resonator. Disk resonators of different radiuses are presented. The resonance state is demonstrated with near-field measurement at the through port and the periphery of the disk. The measurements results are also supported with simulations. Hence the chapter provides the good understanding of optical properties of BSW resonance.

In **Chapter 5**, we study 2D Bessel-like beam on Bloch surface wave platform. Such a beams are generated using a simple planer isosceles triangle (2D axicon). We present the different designs of 2D axicon where the height of the axicon varied from 20  $\mu\text{m}$  to 30  $\mu\text{m}$  with a step of 5 $\mu\text{m}$ . The purpose of studying different designs is to compare the optical performance of 2D Bessel-like beams, in particular propagation distance and full width half maximum. The results obtained from the experiments are in good agreement with the simulation results. We show that the beam propagates without significant spreading for considerable propagation distance. These beams can be used as a low loss (coupling) optical interconnects between on-chip components and optical tweezers.

In **Chapter 6**, we characterize the optical properties of gratings engraved in a single mode waveguide fabricated on top of a dielectric multilayer platform. The design concept of the waveguide grating, CST simulation results and near-field measurement results are presented. The near-field measurement results show that waveguide grating can be used as a 2D Bragg mirror for wavelength inside the photonics band gap.

In **Chapter 7**, we present the brief summary of this work along with the conclusion.



# CHAPTER 2

## Review on BSW

The BSWs have been studied extensively for sensing applications after twenty years of their invention in 1970. However, the work in the domain of 2D optics as a platform for different systems has recently been started – a few years back in our lab, the Optics & photonics technology laboratory at EPFL. The growing interest in BSWs has led many research groups around the world to study the field in order to explore the further possibilities and applications. In this chapter, we present a brief review on the research in BSWs domain performed by different groups. Mainly, the literature on BSWs based 2D devices and BSWs sensing is discussed in this chapter.

### 2.1. 2D polymeric gratings [42]

T. Sfez et al. have studied the behavior of 2D polymeric gratings on the top of a multilayer platform. The multilayer is composed of ten periods of alternating high index and low index layers of silicon nitride, where the refractive index of the layers is tuned by controlling the concentration of ammonia in the PECVD process. The dispersion diagram of the multilayer with the grating has been calculated and a band gap produced by the gratings has been observed. When the BSW is excited (TE polarized light) at the points corresponding to the band edge in the dispersion diagram, a standing surface wave (elongated distribution as compared to the TM-polarized field) - defined by two counter-propagating modes having almost identical amplitudes - is observed, as shown in Fig.2.1. However, away from the bandgap, either the 0 or the  $-1$  diffraction order of the grating can be used to selectively couple the two counter-propagating surface waves. MH-SNOM has been used for near-field mapping and the prism coupler is exploited for the BSW coupling.

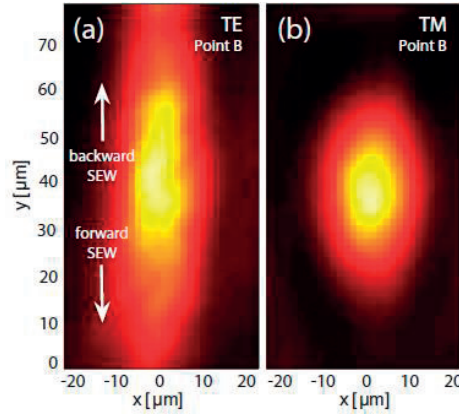


Fig.2.1. Near-field distribution of surface waves over the gratings, obtained from a MH-SNOM, simultaneously for TE and TM polarized incident beam at the band edge of the grating.

## 2.2. Polymer ridges- BSW based waveguide sensor [43]

E. Descrovi et al. have demonstrated a wavelength-selective coupling of BSWs inside and outside the ridge. For BSW coupling a conventional prism-based configuration has been used. They have demonstrated the selective coupling of BSW guiding in an ultrathin 30 nm thick teflon ridge. The wavelength selectivity has been performed by keeping the illumination angle constant but varying the wavelength according to the dispersion diagram. As shown in Fig.2.2 (a, b), SNOM mappings are shown for two different wavelengths corresponding to the coupling inside and outside of the waveguide, respectively. The waveguide configuration provides a micrometric lateral confinement while preserving the surface mode features. This is an advantage for sensing applications. They claimed that: as light could be selectively coupled in specific regions defined by nanometric ridges such a results can open interesting opportunities in surface wave based sensing applications.

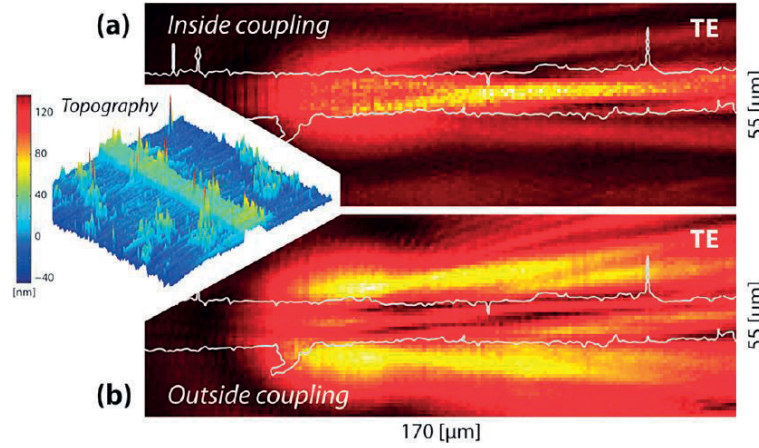


Fig.2.2. The measured SNOM near-field images showing wavelength-selective guided BSW coupling (a) inside and (b) outside the Teflon ridge, respectively. The topography of a 30 nm thick Teflon ridge is shown in the inset.

### 2.3. Refraction of BSWs/Ultrathin ridge waveguides [41], [44]

T. Sfez et al. have demonstrated that a thin dielectric structure deposited on the multilayer deflects the BSW propagation according to Snell's law. The Polymeric ridges were then deposited on top of the multilayer. The polymer was used as a positive photoresist. The width and height of the ridge are 10  $\mu\text{m}$  and 110 nm, respectively. The MH-SNOM has been used for near-field mapping and the prism coupler is exploited for BSW coupling.

The experiments were divided into two parts. In the first part, the BSWs were excited in the coated multilayer and by decreasing the angle of illumination of the BSWs. The transmission through the ridge waveguide and the total internal reflection of the BSWs have been demonstrated (see Fig.2.3). On the other hand in the second set of the experiments, the BSWs were excited in the bare multilayer. The deflection of the BSWs from the ridge obeying Snell's law has been demonstrated. They have proven that a thin dielectric structure deposited on the multilayer deflects the BSWs propagation according to Snell's law. It is reported that the mechanism responsible for the transmission of a BSW through a thin dielectric ridge is an energy transfer from the BSW mode of the bare multilayer to the BSW mode of the coated multilayer. They have proven that the reflection and refraction can be used for the conception of thin optical dielectric structures involving BSWs.

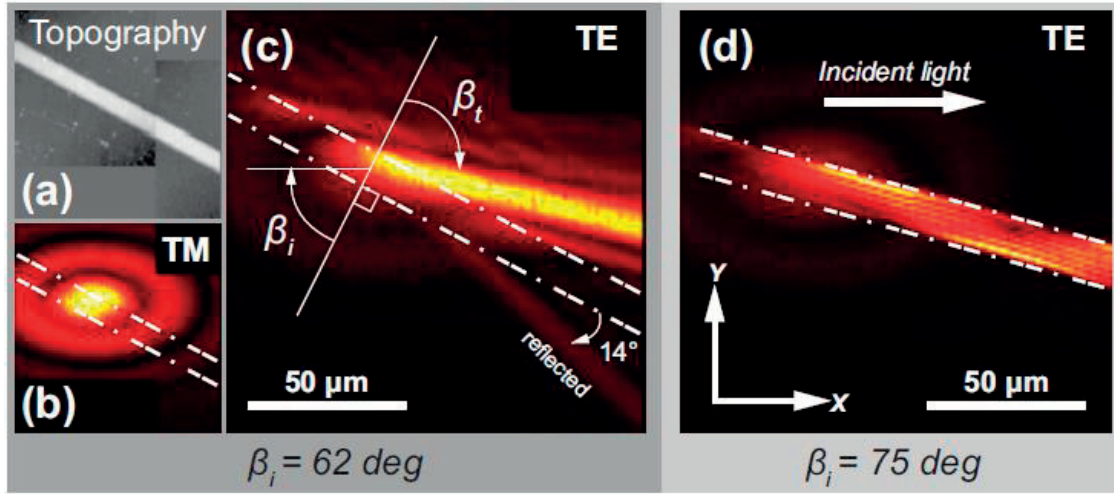


Fig.2.3. Simultaneously measured topography of (a) TM and (b) TE-polarized states of the near-field on the ridge. (c) The TE-light transmitted through the ridge at lower incident angles. (d) The incident angle exceeds the critical angle and the TE-polarized field is trapped in the ridge.

By the same group, further study has been carried out to investigate the modes that can exist in an ultrathin ( $\lambda/10$ ) ridge waveguide and how they can be excited selectively. The width and height of the ridge waveguide are  $4.5\ \mu\text{m}$  and  $140\ \text{nm}$ , respectively. It has been reported that BSW waveguide sustains three modes which can be excited selectively by tuning the wavelength and choosing the excitation polarization, as shown in Fig.2.4. Interestingly, the dispersion relations of the modes have been measured and it has been shown that they lie, as expected, between the dispersion curves of the bare and coated multilayer with photoresist. Furthermore, they have presented the numerical method to retrieve the field components of the modes at the sample surface. Thanks to MH-SNOM which has the capability to detect simultaneously the amplitude and phase of two arbitrary orthogonal components of the near-field. The measured transverse and longitudinal components of each of the modes were shown to have a good agreement with the simulation results.

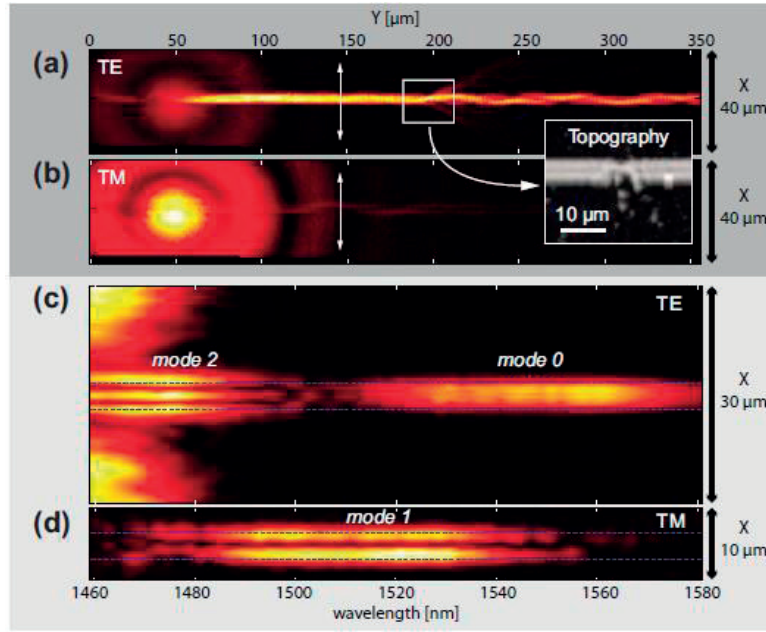


Fig.2.4 Near-field amplitude distribution over the waveguide under (a) TE- and (b) TM-polarized illumination, respectively. Wavelength scan in x direction at the marked white arrows in (a, b) for (c) TE and (d) TM polarization, respectively.

## 2.4. 2D Plano convex Lens [45]

L. Yu et al. have performed first fundamental investigation of 2D plano convex lens appended with a waveguide. The multilayer platform was consisted of six periodic stack of silicon oxide and silicon nitride. The presence of a polymer layer on the top of multilayer platform modified the local effective refractive index, enabled a direct manipulation of the BSW. Here, by adding a photoresist layer, a refractive index contrast  $\Delta n$  between photoresist layer and platform was introduced.  $\Delta n$  plays an important role in defining the optical properties of 2D components. The lens was patterned into a 100 nm thick layer of photoresist. The fabrication was done by UV lithography. The total internal reflection configuration (Kretschmann) was used to couple BSWs on the sample surface. The lens was positioned 100 μm away from the coupling spot. When the BSW illuminates the lens, it focuses the surface wave in a confined spot. To observe the near-field interaction of the BSW with the lens, MH-SNOM has been used. The simulated near-field distribution using CST microwave studio (FDTD method) and measurements results are shown in Fig.2.5. It has been reported that near-field measurement results are in agreement with rigorous calculations. The



measured resolution  $d$  was  $4.36\ \mu\text{m}$  and it is in good agreement with the theoretical prediction. It has been shown that optical properties of the lens can be modified by changing the refractive index contrast. The focusing property of a 2D lens plays an important role in the surface wave field enhancement. It has been shown that the near field intensity is enhanced by 500 times at the focal spot position for TE polarization in comparison with TM as a reference. The possibility to generate a localized spot with highly confined field on the surface for one polarization comparing with the other could be of special interest for sensing applications based on fluorescence or Raman spectroscopy.

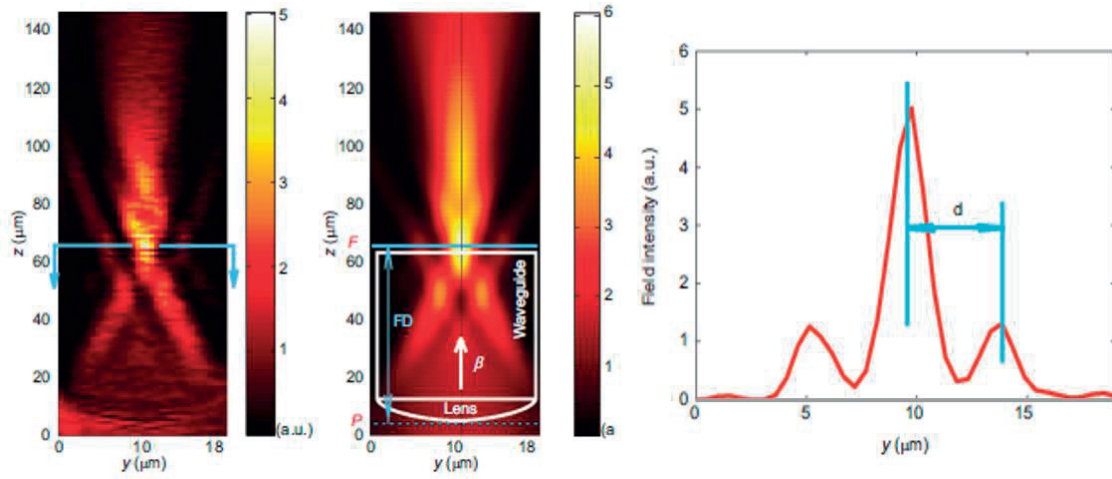


Fig.2.5. Measured MH-SNOM and simulated images of the near-field distribution showing surface wave propagating through a 2D plano convex lens. The cross section of the focus spot is also shown in the side.

## 2.5. 2D Prism and Gratings [46]

The focusing of BSWs has been shown in the preceding section. In this section reflection and diffraction, studied by L. Yu et al., of the BSWs using a prism is presented. The 2D prism was fabricated in 100 nm thick photoresist. The fabrication, BSW coupling and characterization techniques were the same as described in above section.

Two experimental observations have been made to investigate total internal reflection and diffraction. In the first one, the 2D right angled isosceles triangle ( $100\ \mu\text{m}$ ) was illuminated with a BSWs and total internal reflection was verified by studying the near-field amplitude-phase of the

reflected field on the hypotenuse, see Fig.2.6 (a). In the second one, diffracted field arose when the surface beam struck the edge of a right-angle bend at an oblique angle as shown in Fig.2.6 (b). Different diffraction orders of a 2D grating have been observed in near-field and analyzed, by varying the incident angle from 45 deg. to 32 deg. For a grating with period  $4\text{ }\mu\text{m}$ , one more diffraction order was introduced as expected from the theoretical calculations (see Fig.2.6 (c)). On the other hand keeping the incident angle the same but changing the grating period to  $6\text{ }\mu\text{m}$ , the effect of the grating period has been verified in the interference pattern.

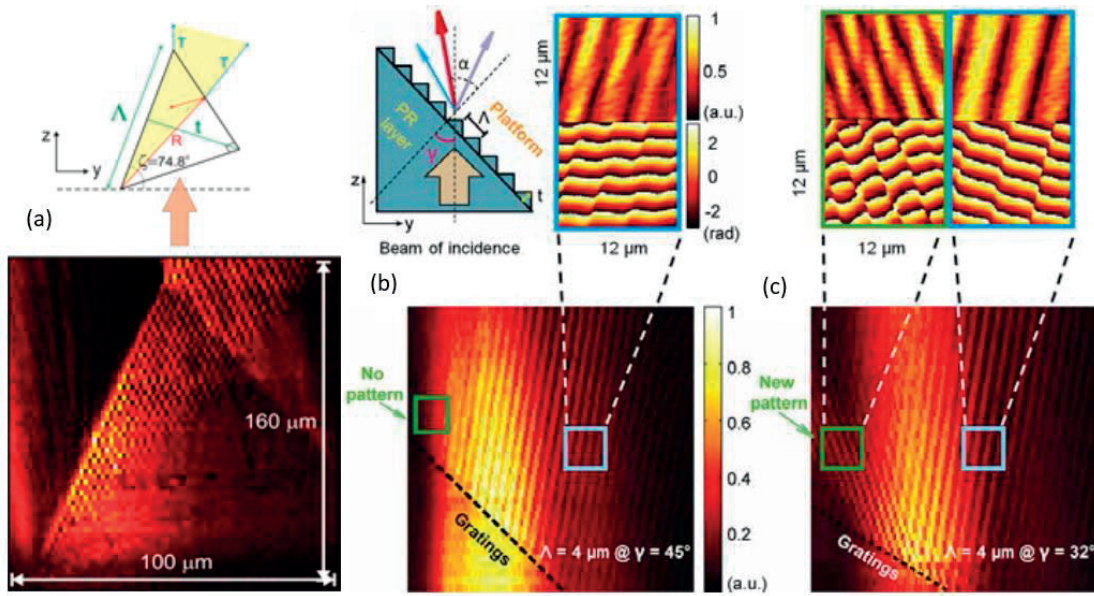


Fig.2.6 (a, b, c). Schematic and measured field amplitudes of 2D prism and grating demonstrating total internal reflection and different diffraction orders. The inset shows fine step scans of amplitude and phase at marked squares.

## 2.6. 2D waveguide grating coupler [47]

The optical waveguide coupler was composed of a parallel array of waveguides. When these waveguides were placed close enough to each other, the light from one waveguide to the other coupled evanescently and exchange of power took place. The optical couplers are of significant interest for optical power division and optical switches in integrated optics and thin film devices.

The optical couplers were patterned into a thin layer of photoresist same as the other devices discussed before.

Two different geometry of couplers have been studied experimentally and theoretically by L. Yu et al. In the first case, the fundamental mode was excited by coupling the BSWs to the left most waveguide as shown in Fig.2.7 (a, b). The total power transfer occurred at a total propagation distance of  $\sim 250 \mu\text{m}$ . In the second case Fig.2.7 (c, d), the second mode was excited. In both sets of experiments, the coupling and energy exchanging process was carefully observed through measurements of near-field amplitude and phase. The measurement results have shown good agreement with the simulation results. The simulations were performed with CST microwave studio using FDTD method. To study the mode propagation and confirm the nature of excited modes, 2D Fourier transform was performed. Besides, by studying theoretically the impacts of the index contrast, gap separation, and waveguide width on the coupling coefficient have been discussed.

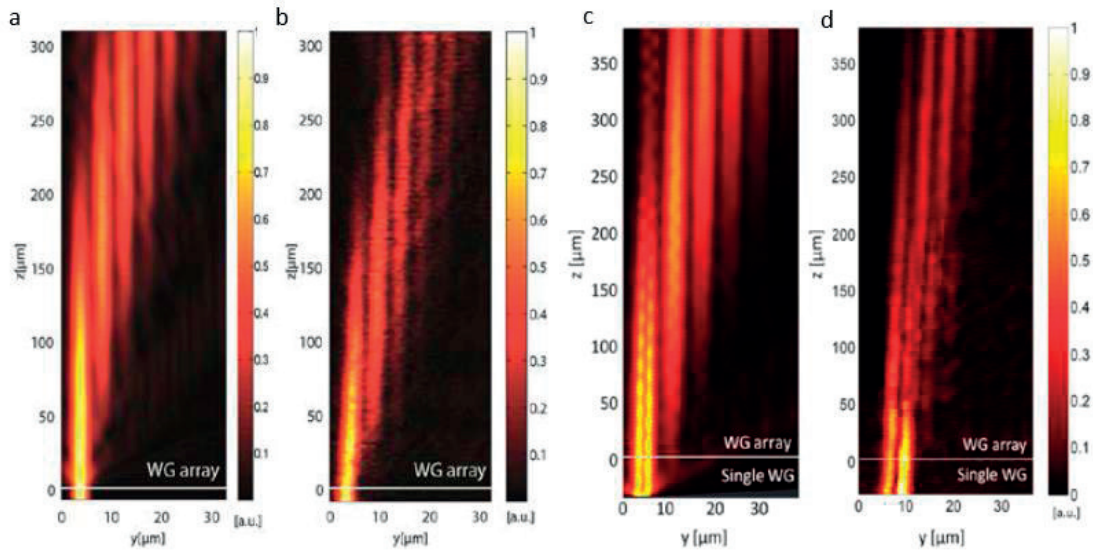


Fig.2.7. Near-field images of mode coupling in two different geometry of waveguide couplers in (a, b) and (c, d) respectively. The right side of each figure is the simulated field image from CST, FDTD method in comparison to the SNOM measurement images.

## 2.7. BSW based sensors – A proof of principle [48]

E. Descrovi et al. have studied and proposed the multilayer platform sustaining BSW as a sensor for surface sensing. It has been reported that Bloch surface wave sensors are strongly sensitive to surface modifications. They have claimed the Bloch surface wave sensors are more sensitive than surface plasmon and waveguide based sensors. The principle for a BSWs sensor has been proven by showing the direct real-time monitoring of the interactions of organic vapors with the multilayers. Finally, higher sensitivity of the surface wave based detection scheme has been presented as compared to a waveguide modes perturbations method.

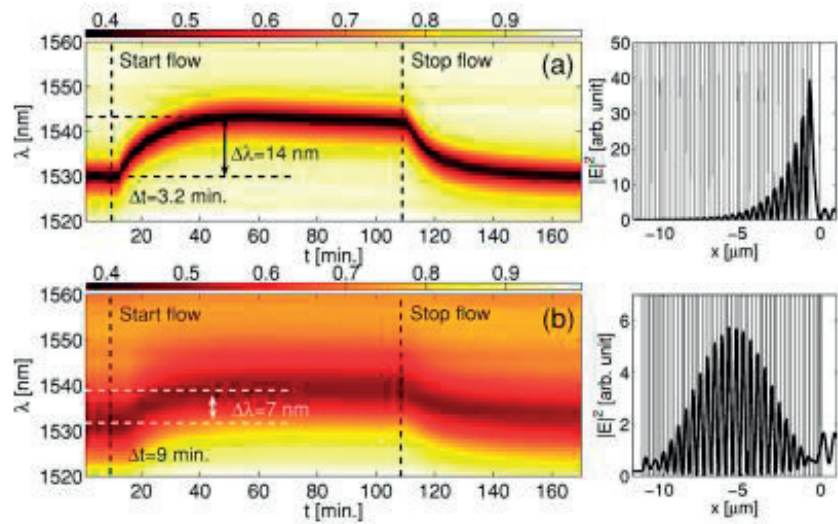


Fig.2.8. Real-time sensing measurement of ethanol vapor by collecting the reflected light from the *p*-Si multilayer, for the surface mode (top) and guided mode (bottom) selectively excited at different incident angles.

The multilayers presented in this work consist of twenty-five periodic stacks of porous silicon. The BSWs coupling and measurements have been performed with Otto coupling configuration. The study provides deep understanding of coupling mechanism. For example, by adjusting the gap between prism and sample the guided or surface modes can be excited selectively. The results are very well presented with the evidence of demonstrating the surface wave based sensing with several improved features than guided mode-based, as shown in Fig.2.8. For example, the resonance dip is much narrower in BSW sensing as compared to the guided mode, the shift of the resonance

wavelength is larger for surface waves, and a shorter delay from the initial vapor in-flow time for surface wave sensing.

Furthermore, some other groups have studied BSWs extensively for sensing applications. Some of these are: experimental sensitivity determination of BSW sensors [49], comparison of Bloch surface wave and surface plasmon polariton based sensors [50], sensitivity improvement of optical biosensors by means of Bloch surface waves [5], diffraction-based biosensors [51], detection of protein aggregation with a BSW based sensor [52] and enhanced surface Raman scattering in the presence of multilayer dielectric structures [53], [54].

## 2.8. Fluorescence emission enhancement by BSW platform [55]

I. V. Soboleva et al. have investigated another fascinating property of BSWs, named field-enhancement. They have reported that the fluorescence emission of Rhodamine 6G (R6G) dye is significantly increased by exploiting the local field enhancement on the surface of multilayer platform sustaining BSWs.

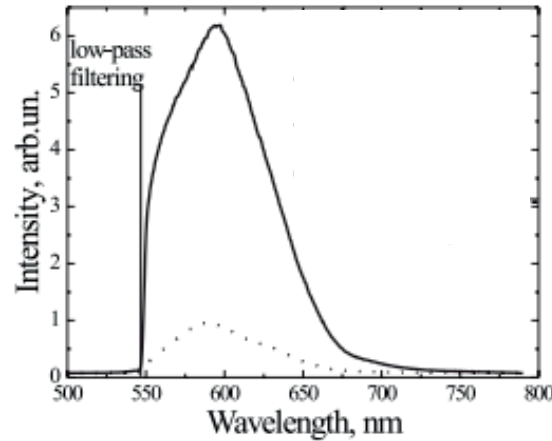


Fig.2.9. The measured fluorescence spectra of R6G dye on the multilayer surface. The solid line and dotted line correspond to TE and TM polarization states of the incident light, respectively.

The multilayers were made up of periodic layers of amorphous silicon nitride. The refractive index of the layers were tuned by changing the content of ammonia in  $\text{SiH}_4+\text{NH}_3$  plasma. The BSWs were simply excited with a BK7-glass prism in the Kretschmann configuration. The far-field fluorescence microscopy has been used to collect the intensity spatial distribution of the surface waves.

Figure 2.9 shows the estimated enhanced fluorescence spectra. The experiment were done for two orthogonal polarization states, TE and TM. The solid line represents a spectrum measured when the BSW is excited with TE polarized laser beam, while the dotted line corresponds to the reference spectrum with TM polarization excitation. The spectrum was measured in the center region of the BSW distribution. The TM polarization ensures the absence of BSW coupling. It can be observed (Fig.2.9) that fluorescent enhancement is about six times higher in magnitude for BSW coupling. The authors state that the divergence of the illumination beam plays a crucial role in the field enhancement effect. Hence, the fluorescent enhancement can be further increased by using collimated beams.

## 2.9. Bloch surface waves based bioprobes - Lab-on-fiber technology [56]

M. Scaravilli et al. have investigated theoretically the excitation of Bloch surface waves on the tip of single-mode optical fibers. The authors claim that this study paves the way for a high-resolution label-free optical biosensing using miniaturized high-performance surface-wave fiber-optic devices, and it provides an important step ahead towards the “lab-on-fiber” technology. The low loss dielectric materials have the advantage of much narrower resonances which lead to larger overall figures of merit than the metallic counterpart for sensing applications. However, reduced confinement capability of the BSW evanescent tail, yields a lower sensitivity than SPPs.

The multilayers considered in this work were consisted of silicon monoxide ( $\text{SiO}$ ) and silica ( $\text{SiO}_2$ ) as high and low contrast materials. As in a single-mode optical fiber the fundamental mode propagates along the core axis (leads to normal incidence at the fiber tip), to couple the BSWs on fiber tip grating-coupling-based scheme has been studied. The calculations have been performed using rigorous coupled-wave approach (RCWA). The zeroth-order of the reflected light for a TE-polarized incident plane-wave has been examined to calculate the reflectance spectrum. The



resonance arose due to superimposition BSW resonance and the resonance due to interaction between the zeroth-order reflected mode and the multilayers.

They study two configurations of gratings on multilayer. In the first one, multilayers are placed on the top of gratings. Considering fabrication-related non idealities, they discussed that corrugated shapes of the gratings can partially propagate and may perturb the subsequently deposited multilayer. Therefore, they numerically simulated a structure in which all layers possess a periodic pattern the same as the diffraction grating with a fraction of the height of the original gratings, in order to estimate the effect of corrugation. They found that the linewidth ( $Q$ -factor) of the resonance increases (decreases) up to 23 times in comparison to the ideal case. These results led them to study another configuration in which the diffraction gratings are designed on the top of the multilayer which has been proven more reliable considering effects of the fabrication process.

A well-defined study to show the effect of grating parameters on BSW properties resonance has been presented. The grating period has been chosen to define a particular coupling wavelength. The height, duty-cycle and number of periods can be selected to optimize the characteristics of the resonance in sense of linewidth and the visibility of resonance amplitude in the spectral range. It has been shown that there is a trade-off between visibility and linewidth of the resonance if the grating height and duty-cycle is varied. By decreasing the height/duty-cycle the spectral selectivity gets enhanced (linewidth decreases) but the resonance amplitude decreases. Similar conclusion has been drawn for changing the number of periods of the multilayer. By increasing the number of periods, the reflectivity of the dielectric mirror was increased and 100% of the power coupled back with the zeroth-order reflected mode which provides the optimum characteristics of the resonant lineshape. Basically, the number of periods did not affect the linewidth of the resonance, but the resonance amplitude increased significantly. Instead of the increasing number of periods, the higher refractive index contrast dielectric materials can be used for the multilayers to enhance its efficiency as a dielectric mirror.

They have also investigated the sensing performance of a BSW tip. The bulk sensitivity has been defined as the shift of the BSW resonance wavelength with respect to variations of refractive index of external medium. The longer field exponential tail of the surface wave in the external medium provides stronger interaction with the environment (higher field enhancement) and hence higher sensitivity. The length of the exponential tail varies inversely to the difference between the coupling angle and the critical angle. Based on this theory, they proposed a new design where the excitation angle has been chosen very close to the critical angle. Therefore, the calculated enhancement factor was obtained 35% higher in comparison to previous design and the evaluated

sensitivity in linear regime was found to be higher over a factor of four. The new design has been proven to be more robust against material losses in multilayer. The numerically calculated sensitivities are in line with those of plasmonic bioprobes. However, BSW based bioprobes always add the key advantage of offering much narrower spectral resonances. This study provides deep understanding of the design rules for label-free bioprobes based on BSWs, integrated on optical-fiber tips.

## **2.10. On-chip phase-shifted Bragg grating for spatial differentiation of Bloch surface wave beams [57]**

Another planar structure to manipulate the properties of BSWs has been studied. L. L. Doskolovich et al. have studied theoretically phase-shifted Bragg gratings (PSBG) for spatial differentiation of BSW beams. The spatial differentiation and integration of optical beams is an import operation of analog signal processing. As BSWs are considered as prospective information carrier in integrated circuits, this device can be exploited as an integrated information processing system with BSW pulses and beams carrying information.

The conventional PSBG consists of two symmetric Bragg gratings separated by a defect layer. To design analogous on-chip PSBG, the ridges of the grating were made in the top most layer of BSW multilayers. Further, the lengths of the ridges and the grooves between them was kept the same as the layer thicknesses of the conventional PSBG. As the effective refractive index of the BSW is defined by the thickness of the topmost layer of the multilayers, the values of the heights of the ridges were chosen to match the BSW effective refractive indices with corresponding refractive indices of the conventional PSBG layers. At particular thickness of the defect layer, the reflection of PSBG vanished for a specific wavelength and incident angle. Because of the presence of a zero in the reflection spectrum, PSBG can be used as spatial and spectral filters and for the different transformations of optical beams.

They have compared the results of on-chip PSBG with free space conventional PSBG using the rigorous coupled-wave analysis method. It has been shown that the reflection spectrum of on-chip PSBG and of free space conventional PSBG is in good agreement with each other. However, the position of the minimum of the reflection coefficient of BSW PSBG was found to be slightly shifted from conventional PSBG.



Further, the effect of the number of periods of the grating and the width of the incident BSW on the characteristics of the resonance spectrum has been demonstrated. It has been said that a trade-off can be achieved between the differentiation quality and the maximum amplitude of the reflected light. For example, increasing the number of layers led to increased maximum amplitude, but decreased differentiation quality. On the other hand, as the width of the incident BSWs increased the maximum amplitude decreased. However, the behavior of the differentiation quality was a bit complex. It was increased or decreased depending upon the number of grating periods.

Figure 2.10 (a) shows the incident Gaussian BSW beam (dotted black curve) and the corresponding reflected beam (solid blue curve). The exact derivative of the incident beam profile is also presented in the red dashed curve. Figure 2.10 (b) represents the simulation image of the field distributed over PSBG on the top of the multilayers. The incident BSW and its corresponding differentiated BSW can be seen clearly. They reported that the beam shape of the reflected light is almost retained upon propagation. This study can be applied to design a BSW based integrated system for optical information processing.

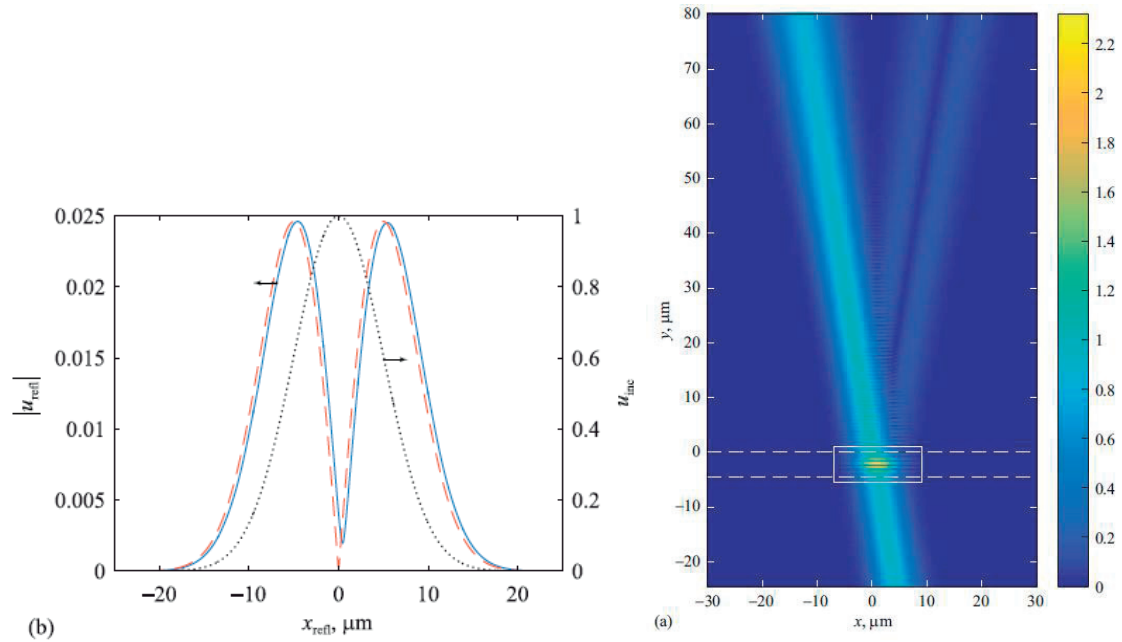


Fig.2.10 (a) The incident beam profile (dotted black curve), the absolute value of the reflected beam (solid blue curve) and the absolute value of the exact derivative of the incident beam profile (red dashed curve). (b) The field distribution of the incident and reflected light (differentiated) over PSBG is shown with white dashed lines.

## 2.11. Bloch-like surface waves in quasi-crystals and aperiodic dielectric multilayers [58]

Until now, we have studied the existence of Bloch surface waves in periodic multilayers. Recently, V. Koju et al. have numerically studied the presence of BSWs in quasi-crystals and aperiodic dielectric multilayers. In their work, this kind of surface modes are addressed as Bloch-like surface waves (BLSWs). The Bloch-like surface waves have been excited in Fibonacci quasi-crystals (FQC) and Thue-Morse aperiodic dielectric multilayer (TMADM) using the prism coupling configuration.

They have reported two advantages of using this kind of structures over conventional periodic multilayers. First – the field enhancement at the surface due to BLSWs (FQC/TMADM) was significantly improved compared to the one produced by BSWs (periodic multilayer). This improved field enhancement is good for designing efficient optical slow light devices and enhancing surface detection based techniques, for example surface-enhanced Raman spectroscopy, fluorescence-based detection and biosensing based on enhanced diffraction. Second – the penetration depths of the exponentially decaying tail of BLSWs were increased in external medium which leads to stronger interaction of the surface mode with the outer environment and hence higher sensitivity. This feature combining with high field enhancement can be utilized to design sensitivity enhanced biosensors.

The quasi crystal (FQC) was designed with 34 layers of  $\text{TiO}_2$  and  $\text{SiO}_2$  for around visible wavelength spectrum. The considered FQC pattern was ABAABABAABAABABAABAABABAABAAB where A and B were high and low index layers. This sequence is aperiodic. It can be rearranged in periodic subgroups, for example  $\text{XYXYXZ}$ , where  $X = \text{ABAABA}$ ,  $Y = \text{BAABAAB}$ , and  $Z = \text{AB}$ . Therefore, the complete sequence can be treated as periodic layers of X and Y with Z as a defect layer. This structure exhibited two BLSW modes. The maximum obtained field enhancement (FE) and penetration depth (PD) were  $\sim 1500\times$  and 533 nm respectively.

Another structure TMADM was designed with 32 layers of  $\text{TiO}_2$  and  $\text{SiO}_2$  for the same wavelength range. The TMADM pattern was ABBABAABBAABBBABAABBBABAABBAABAAB. If the sequence was rearranged in subgroups, only near-periodic patterns can be achieved. The discussed TMADM design has shown four BLSW modes. The maximum achieved FE and PD were  $\sim 2450\times$  and 960 nm respectively.

For the sake of comparison the results for periodic dielectric multilayers (PDMs) were also presented. The PDM was consisted of 32 periodic layers of  $\text{TiO}_2$  and  $\text{SiO}_2$ . The maximum obtained values of FE and PD were  $\sim 600\times$  and 55 nm, respectively.

In summary, FCQ and TMADM structures have demonstrated several advantages over conventional periodic multilayer structures. These include, the field enhancement at the surface folds many times, the penetration depth inside the air is significantly increased and the field energy density is strongly confined at the surface because the field density decays rapidly inside the structure. Among all three designs, TMADM has shown maximally improved FE and PD. It should be noted that PDM has exhibited only one BSW mode for the same range of working wavelengths. Unlike, BSW modes the field profile of BLSW modes neither decayed exponentially inside multilayers nor strictly varied with periodicity. These structures possess the flexibility in the design of the optical device with enhanced optical properties.

## 2.12. Theoretical study of Bloch surface waves ring resonators [59]

M. Menotti et al. have studied theoretically Bloch surface based ring resonators at visible wavelengths. They considered the multilayers consisting of 10 periods  $\text{TiO}_2$  and  $\text{SiO}_2$ . The ring resonator was designed in polymethyl-methacrylate (PMMA) ridges on the top of multilayer. In order to reduce the computation time and memory, they have adapted an approach to reduce the dimensionality of the problem. They have opted effective index approach which is executed by decomposing the 3D problem into two independent 1D and 2D problems. The first problem dealt with the vertical field confinement (because of surface state) in an effective multilayer, on the other hand the second problem solved the resonant modes by simulating an effective 2D system using an FDTD method.

The quality factor (Q) of the resonance mode was defined by the two independent loss mechanisms. One defines leakage of surface mode through the substrate because of finite number of periods in the multilayer ( $Q_{\perp}$ ), while the other deals with the bending losses due to ring radius ( $Q_{\parallel}$ ). The total quality factor (Q) has been calculated adding  $Q_{\perp}$  and  $Q_{\parallel}$  in parallel. They have demonstrated the dependence of the quality factors on  $Q_{\perp}$  and  $Q_{\parallel}$  on the multilayer parameters, such as number of periods and ring radius, respectively, as shown in Fig.2.11. It should be noted that scattering losses at the interface between layers due to surface roughness and fabrication

imperfection are neglected in the calculations. The results have shown that a Q factor  $\sim 10^7$  can be achieved with a footprint of  $\sim 250 \mu\text{m}^2$ . The authors claim that even allowing scattering losses, the Q factor would still remain upto  $\sim 10^4$ . This study provides the limiting parameters of the Q factor and the understanding of the design of BSW based ring resonators for sensing and integrated optics applications.

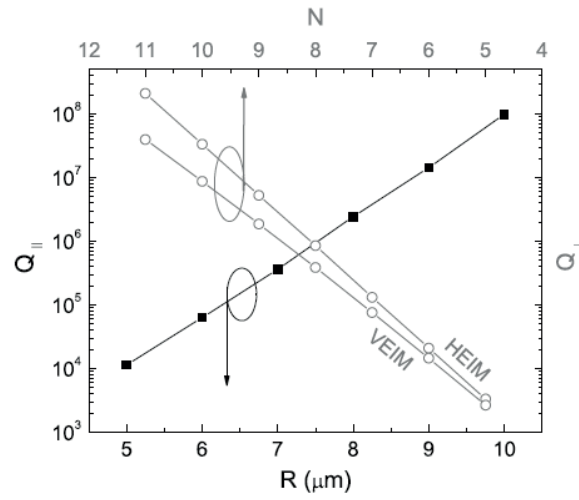


Fig.2.11. In plane and perpendicular quality factors as a function of ring radius and number of periods of multilayer calculated using the effective index method and FDTD simulations.

### 2.13. Slow light Effect – Bloch Surface Waves [60]

Recently, it has been demonstrated that in a specific configuration Bloch surface waves can be used to slow down the light for the applications where slow light effect is exploited to make optical buffers and enhanced surface detection based techniques. V. Koju et al. have studied theoretically the slow light effect in BSWs using double prism tunneling configuration. They have reported that this method is simple and practical compared to other techniques studied in past. The set up was consisted of two prisms separated by an air gap.  $\text{TiO}_2$  –  $\text{SiO}_2$  multilayers structure was deposited on the face of one of the prism and the second prism placed on the top of multilayers maintaining an air gap in between. The second prism allowed the evanescent field of BSW in the air to couple into radiative mode of the prism and transmit through it. This process was governed by the frustrated total internal reflection. The light was stored temporarily on the surface as a BSW before

being transmitted through the second prism. This process provides the time delay to the transmitted light (see Fig.2.12). And the strength of the coupling from surface mode (BSW) to radiated mode (transmitted light) was defined by the air gap. They have considered a Gaussian temporal pulse profile as incident beam (through prism) in simulations.

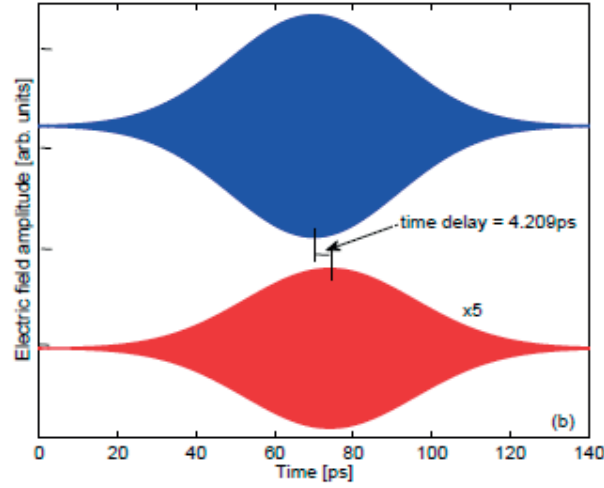


Fig.2.12. The delay of 4.209 ps shown between incident and transmitted pulses, at the top and bottom, respectively.

The group index (time delay) and the transmittance have been studied for different air gap spacing and different number of multilayer periods. It was observed that at smaller air-gap thickness, the group index is low while transmittance is high. Gradually, an optimum value of the air gap was achieved and a desired group delay with acceptable transmittance was obtained. Furthermore, increasing the air-gap thickness did not increase the group index, however it started decreasing because increasing the air-gap thickness decreases the transmittance significantly. The similar behavior has been shown when varying the number of periods of multilayers. The results reported that light can be slow down by a factor of up to 400 using BSW based double prism coupling configuration. The slow down factor can further be increased by choosing the material of multilayer with high refractive index contrast. As an illustration, a time delay of 4.209 ps ( $n_g \sim 350$ ) with the optimum air gap thickness of 1600 nm has been shown in Fig.2.12.

## 2.14. Grating coupler for Bloch surface waves [61]

The intercrossed gratings have been used as a highly miniaturized BSW launcher and beam splitter for on-chip integrated systems. T. Kovalevich et al. have demonstrated experimentally the coupling of BSW through in-plane grating coupler. Further, the direction of BSW propagation can be tuned by changing the polarization of the incident light. The illumination had normal incidence. The wave vector matching condition to couple BSWs was attained by the grating vector. The groove size in the grating has been optimized to have a maximum of BSW coupling using RCWA simulations. The designed gratings were fabricated with focused ion beam milling.

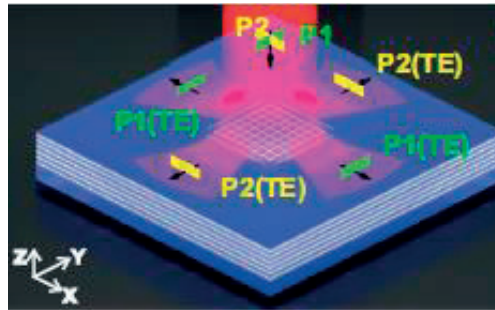


Fig.2.13. Schematic showing BSW coupling at the intercrossed grating for two orthogonal polarizations.

The polarization of incident beam was rotated using a half wave plate. The light with the polarization direction (E-field) parallel to the grating direction (perpendicular the period of the grating) passed through the grating while light with perpendicular polarization was blocked (see Fig.2.13). In this way, by designing two grating crossing each other perpendicularly the direction of the BSW propagation can be tuned in two perpendicular directions with a control on power division in both directions. The reported theoretical coupling efficiency of the presented in-plane BSW coupler is 18%.

## 15. Tunable Bloch surface waves - lithium niobate thin films [62]

The Bloch surface wave integrated system can be improved by adding tunable components. Lately, Tatiana Kovalevich et al. have reported that it is possible to obtain active tunability in BSW

sustaining systems. The optical properties of BSWs may be controlled by the effective index change of the top most layer of the multilayers. They have used thin film of lithium niobate ( $\text{LiNbO}_3$ ) as a high index material top layer. The electro- and thermo-optical properties of  $\text{LiNbO}_3$  can be used to design novel tunable and active planar optical components for BSW based 2D integrated optics. The refractive index of a thin film of  $\text{LiNbO}_3$  can be changed using the electro or thermos optical properties of the film. The other way to approach the same problem is to rotate the sample such that BSW couples along either ordinary or the extraordinary axis of  $\text{LiNbO}_3$ . Both axes offer different refractive indexes,  $n_o$  and  $n_e$  for ordinary refractive index and extraordinary axes, respectively. They have demonstrated different BSW coupling angles corresponding to ordinary or the extraordinary axes, owing to anisotropic property of the multilayer +  $\text{LiNbO}_3$  system.





# CHAPTER 3

## Propagation Properties of Bloch Surface Waves

In this chapter, we study experimentally the propagation properties of Bloch surface waves at the interface of a dielectric multilayer platform. We use thin layers ( $\sim\lambda/25$ ) of titanium dioxide as a device layer of high index material. The refractive index of the surface mode has been studied theoretically and experimentally. We exploit multi-heterodyne scanning near-field optical microscopy and far-field characterization in our study. The longest propagation length is achieved when the multilayer is designed to have the dispersion curve positioned close to the middle of the photonics band gap. This study paves a way to realize efficient and compact two-dimensional components and systems.

The propagation length  $L_{BSW}$  and effective refractive index  $n_{eff}$  are the key parameters of BSWs, which determine the losses associated with the multilayer platform and the optical properties of the surface modes and optical components, respectively. We study  $L_{BSW}$  and  $n_{eff}$  for different thicknesses of device layer. The purpose is to be able to determine the thickness of the 2D optical components (based on the results obtained) which are patterned into device layer.

The decay of the amplitude of the surface mode along the propagation direction results from absorption in the material, surface scattering and leakage into the multilayer because of prism coupling. However, due to the low absorption of dielectric materials (constituent material) and to the low roughness of the multilayer surface, absorption and scattering do not have a significant contribution to the losses [63], [64]. Hence, the BSW is mainly decaying by the leakage into the prism. The decay coefficient of the surface mode due to leakage losses into the multilayer (neglecting the absorption and surface scattering losses) decreases exponentially as the number of periods of the multilayer increases [1].

For a particular design of multilayer, the thin high refractive index layer on top of the BSW platform tends to increase  $n_{eff}$  and hence the electromagnetic field confinement. The position of

the surface mode inside the bandgap can be altered by tuning the thickness of this layer. This provides a better control of the optical properties of the surface mode, such as high propagation length and tight confinement to the surface. Furthermore, the thickness of this layer plays a key role in determining the BSW frequency (propagation vector), which can thus be tuned within the photonic band gap. The concept of using a thin layer enables the fabrication of customized 2D photonic elements at the surface of a standard multilayer. The main advantage is the ease of fabrication of 2 D structures compared to 3D and the standard fabrication techniques used for the platform [44]–[47], [65].

In addition to the design of the multilayer, optical properties of BSW depend strongly on the coupling configuration. In our case, we are using a prism coupling system to couple a Gaussian beam with a given divergence in order to create a coupling zone on the surface of the multilayer. Based on Ulrich's paper [66], one can estimate the coupling efficiency; this latter depends on the beam waist of the illuminated spot. For the prism coupling configuration, Ulrich defines the ratio propagation length /beam waist as a coupling parameter which is controlled, among other means, by changing the number of periods in the multilayer design. It has been reported that for very weak coupling, when coupling parameter  $\gg 1$ , less energy is coupled to the surface of the multilayer. On the other hand it decays slowly due to low leakage. Therefore the coupled surface mode has longer propagation length. Coupling can be improved by using a collimated beam of incidence.

### 3.1 Constituent material and multilayer platform design concept

The multilayer platform consists of a dielectric stack, equivalent to a Bragg mirror, with periodically alternating high and low refractive index materials. The periodic structure consists of six periods of silicon dioxide ( $\text{SiO}_2$ ) and silicon nitride ( $\text{SiN}_x$ ) having a refractive index of 1.45 and 1.79 at  $\lambda=1550$  nm, respectively. The periodicity of the multilayer is terminated by a 50 nm-thick terminating layer (top layer) of  $\text{SiN}_x$ . The thickness of the top layer determines the field profile of the BSW mode inside the multilayer [67]. The thicknesses of the  $\text{SiO}_2$  and  $\text{SiN}_x$  layers are 472 nm and 283 nm, respectively. The complete structure (Bragg mirror + top layer), called Bare Multilayer (BML), is deposited on a glass wafer as shown in Fig.3.1. We exploit the BML as a platform for integrated optics which enables the wafer scale production and hence the low cost fabrication technology (see Ref. [45]). The BML exhibits a photonic band gap at telecom wavelengths and a BSW can be excited with TE and/or TM polarization. In the present work the multilayers are designed for TE polarization at the wavelength around 1550 nm.

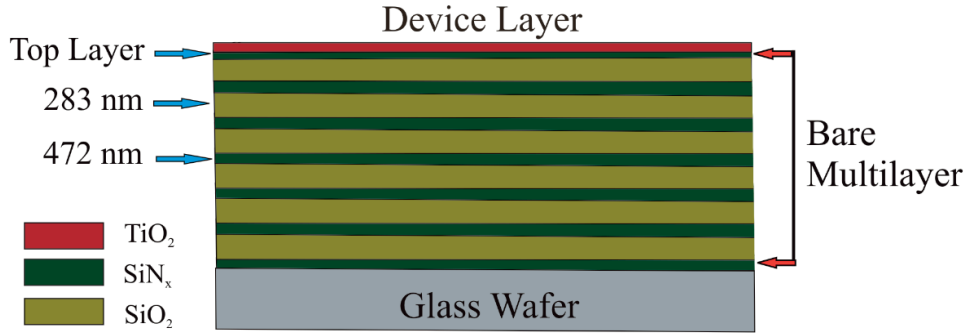


Fig.3.1. Schematic of BSW platform consists of periodic stack of dielectric multilayers (silicon dioxide and silicon nitride) deposited on a glass wafer.

As already mentioned, a topmost layer of a high refractive index material, which will be addressed as a device layer hereafter, can be deposited on top of the BML. It can serve as an efficient device layer to shape micro/nano-photonic structures for further integrated optics applications. We use titanium dioxide ( $\text{TiO}_2$ ) as a device layer of high refractive index material. It has a refractive index of 2.23 at the wavelength of 1550 nm. The material is transparent in the visible and near-IR regions of light [64]. High refractive index provides strong in-plane confinement of the light and enables the development of compact and low loss complex shaped integrated 2D photonic devices. Here we study the effect of different layer thicknesses of  $\text{TiO}_2$  deposited on the BML on the BSW characteristics.

To design a multilayers, one should know thickness of the alternative layers of given refractive indexes and their number of periods. In this section we will discuss the reason of choosing particular thicknesses and number of layers. The thicknesses should be chosen to acquire maximum transmission (coupling strength) per length at a given indices, wavelength and incident angle. The condition for maximum transmission, which makes it possible to minimize the overall thickness of multilayer platform, is derived somewhere else using impedance approach [68]. Very interestingly it can be seen that the commonly held opinion that quarter wavelength thickness of the layers provide maximum transmission per length is not correct. In particular, for the larger incident angle (grazing incidence), the quarter wavelength thicknesses are not optimal thicknesses. Figure 3.2 shows the transmission coefficient diagram as a function of thicknesses of  $\text{SiN}_x$  and  $\text{SiO}_2$ . It is calculated for refractive indexes  $n_1 = 1.79$  and  $n_2 = 1.45$  of  $\text{SiN}_x$  and  $\text{SiO}_2$ , at wavelength  $\sim 1550$  nm and at 58.26 deg. incident angle (BSW coupling angle for device layer of 60 nm  $\text{TiO}_2$ ). The point marked with diamond represents the thicknesses of the alternating layers used in this work. It can be noticed that the chosen thicknesses fall inside the maximum transmission region.

To demonstrate the effect of choosing quarter wavelength thickness on the BSW coupling strength, we plot the reflectance of multilayers with respect to incident angle for two different thicknesses of alternating layer. For example, quarter wavelength thicknesses are chosen for the largest angle used in experiments presented in this work. The one dimensional periodic multilayer stack can be dimensioned as a quarter-wavelength [69].

$$d_1 = \frac{\lambda}{4n_1 \cos \theta_1} \quad (3.1)$$

$$d_2 = \frac{\lambda}{4n_2 \cos \theta_2} \quad (3.2)$$

Where  $n_1/d_1$  and  $n_2/d_2$  are refractive index/thicknesses of  $\text{SiN}_x$  and  $\text{SiO}_2$  respectively,  $\theta_1$  and  $\theta_2$  are incident angle inside  $\text{SiN}_x$  and  $\text{SiO}_2$  layers respectively and  $\lambda$  is an operating wavelength. At incident angle (inside prism)  $\theta = 58.26$  deg.,  $n_1 = 1.79$  and  $n_2 = 1.45$  and  $\lambda = 1550$  nm, the obtained  $d_1$  and  $d_2$  are 308 nm and 562 nm.

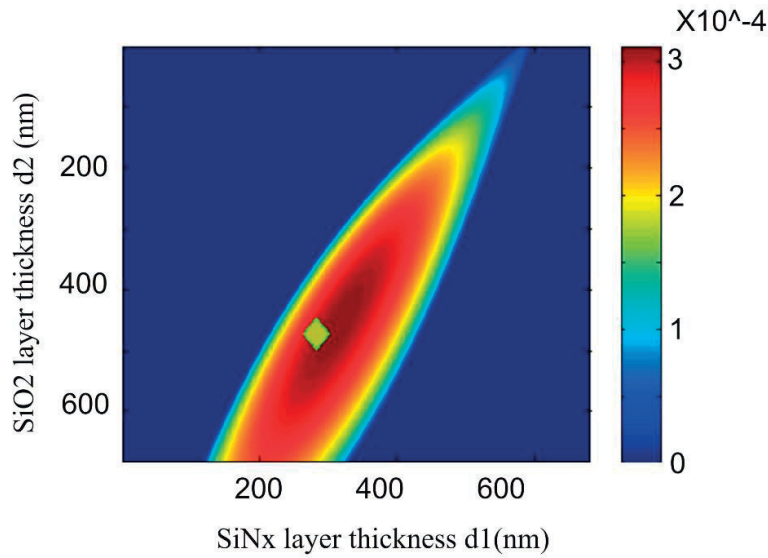


Fig.3.2. The diagram of band gap extinction of multilayers as a function of layer thicknesses.

We calculate the reflectance plot for 6 periods of  $\text{SiO}_2$  and  $\text{SiN}_x$  for the optimally chosen thicknesses ( $\text{SiO}_2 = 472$  nm and  $\text{SiN}_x = 283$  nm) than quarter wavelength thickness ( $\text{SiO}_2 = 562$  nm

and  $\text{SiN}_x$  – 308 nm), as shown in Fig.3.3. The stronger coupling (deeper reflection dip) can be observed for the optimally chosen thicknesses of alternating layers.

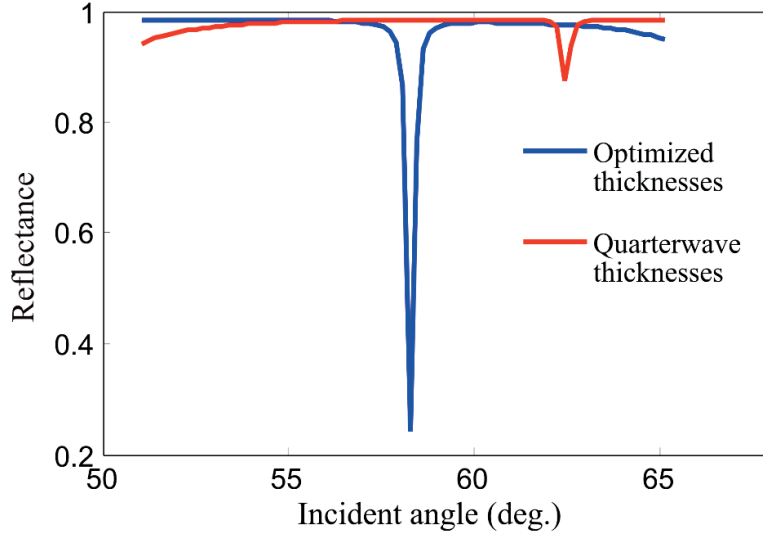


Fig.3.3. Reflectance curve of multilayer platform as a function of incident angle for two different thicknesses of alternative layers. The blue curve represents optimally chosen thicknesses while red curve corresponds to quarter wavelength thickness.

The particular number of layers have been chosen to achieve optimum BSW excitation condition and low leakage losses. On one hand, decreasing the number of layers increases the coupling strength but on the other hand it increases the leakage losses and vice versa. We have optimized our design with six periods of  $\text{SiO}_2$  and  $\text{SiN}_x$ .

Please note that in practice, material absorption is too low to be measured accurately from ellipsometry. However, the depth of the BSW resonance depends on the material absorption losses. For an ideal multilayer platform, all the light coupled to BSW under resonant conditions will couple back to the prism. On the other hand losses also cause the broadening in resonance width. Therefore, for the design purpose minimum losses are required in order to find a balance between observing the resonance and width of resonance. From literature, the estimated value of imaginary part of both layers is approximately  $10^{-4}$  [70]. However, in calculations, we adjust the imaginary part of the refractive indexes of  $\text{SiO}_2$  and  $\text{SiN}_x$  to observe the resonance dip clearly.

The BML platform is fabricated using Plasma-Enhanced Chemical Vapor Deposition (PECVD, PlasmaLab 80+ by Oxford Instruments), while Atomic Layer Deposition (ALD, TFS 200 by Beneq) is used for  $\text{TiO}_2$ . This device layer has to be only a few tens of nanometers thick

and ALD is an ideal method to deposit a homogenous coating all over the surface of the BML. The accuracy in thickness, the conformality of the film, and the quality of the material possible with ALD technique is ideal for nanophotonic structures [71]. As previously demonstrated, the last layer has a crucial importance in the confinement and propagation length of the BSW [67], making the precision of the deposition of this last layer a key point of the fabrication process.  $\text{TiO}_2$  has been deposited using titanium tetrachloride and water as precursors at a process temperature of  $120^\circ\text{C}$ . At this temperature, the deposited material is amorphous reducing risks of intrinsic scattering and thus reducing losses. The deposition rate is  $0.07 \text{ nm/cycle}$ , which explains the high accuracy of the layer thickness.

The dispersion diagram of the semi-infinite multilayer is plotted in Fig.3.4. It shows the radiative (black) zones and non-radiative zones for propagation within the multilayer. The surface modes exist within the white zones that correspond to the photonic bandgap of the dispersion diagram. This means that the BSW cannot radiate in air and have frustrated radiation into multilayer. The dispersion band diagram of the underlying multilayer is calculated with the transfer matrix method [72].

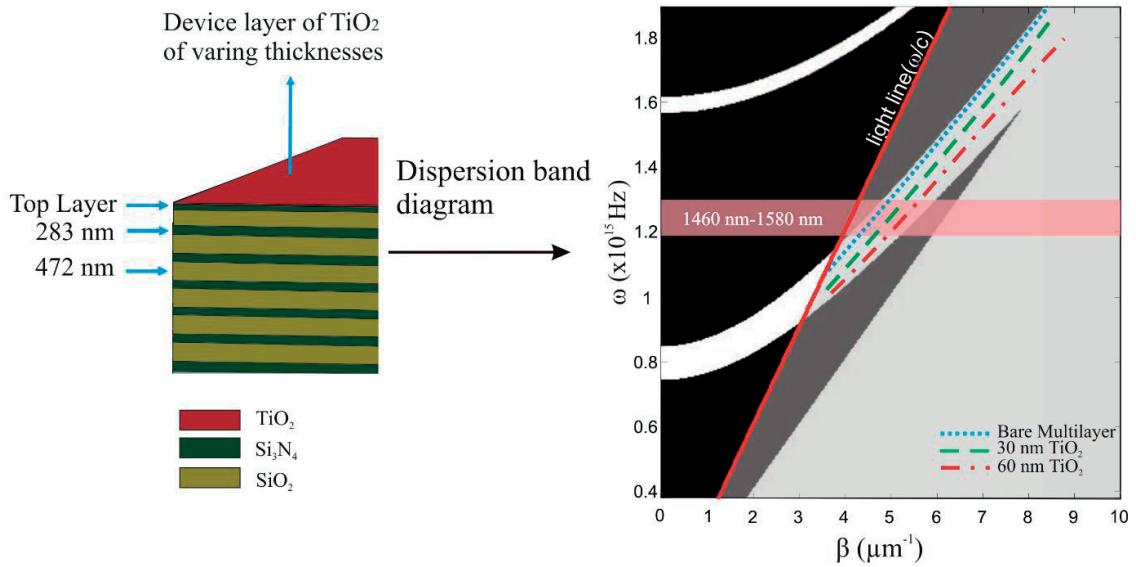


Fig.3.4. Dispersion band diagram of the underlying multilayer with semi-infinite stacks for TE polarization. The white zones represent the photonic bandgap of periodic multilayer. Inside photonic bandgap, the dispersion lines of different colors correspond to different thicknesses of  $\text{TiO}_2$ .

The  $\beta$  axis is the propagation constant  $\beta = (2\pi/\lambda) n \sin\theta$  of the incident light which is parallel to multilayers and the  $\omega$  axis represents the angular frequency  $\omega = 2\pi c_0/\lambda$ , where  $\lambda$  is the wavelength

of incident light in vacuum,  $n$  is the refractive index of the prism,  $\theta$  is the incident angle and  $c_0$  is the speed of light. The chosen parameters of the platform are such that the dispersion relation of the surface mode lies in the photonics band gap. The propagation properties of the surface mode on the platform can be altered by changing the thickness of the top layer or the device layer. Their thicknesses define the location of the dispersion line in the band gap. It is revealed in the dispersion diagram, Fig.3.4 that by increasing the thickness of the device layers, the BSW dispersion line moves towards the right side edge of the band gap which means higher propagation constant at a fixed wavelength.

One can see in Figure 3.4 that the dispersion relation of the BML and the 60 nm device layer appear near the upper and lower edge of the bandgap, respectively, whereas the dispersion relation of the 30 nm layer of  $\text{TiO}_2$  lies in the middle of the bandgap. For the Bloch surface modes that occur near the center of the bandgap, the attenuation by the periodic multilayer stack is stronger and the mode is tightly confined to the surface (see Fig.3.5 (b)). For the modes close to the edges, the attenuation is relatively weaker and the evanescent field penetrates much further into the multilayer [7], [67]. Therefore, the PBG based platform can be designed based on the application behind. Strong field enhancement is needed for sensing and nonlinear applications while modes with longer propagation length are required for integrated optics.

Figure 3.5 (a) shows the relation of the BSW dispersion line in the photonic bandgap for different thicknesses of top layer (red curve) and device layer (blue curve). It should be noted that the calculations with the device layer has been performed with fixed thickness of top layer (50 nm). One can see that by increasing either the device or the top layer thickness, the corresponding propagation constant of the BSW mode increases. Since the device layer has a higher refractive index, the propagation constant of BSW changes remarkably with the thickness. The imaginary part of the BSW wave vector ( $\text{Imag}(K)$ ), which is in the direction perpendicular to the multilayer interface, controls the exponential damping of the electric field inside the multilayer [59]. In Fig.3.5 (b), we plot (in red) the absolute value of the product of the period of multilayer and  $\text{Imag}(K)$  with respect to the effective index ( $n\sin\theta$ ). One can see that the values are higher in the middle of the bandgap which refers to the fact that attenuation by the PBG material is stronger. Consequently the evanescent field cannot penetrate deeper into the multilayer. The blue stars refer to the values of the ( $\text{Imag}(K)$ ) for different thicknesses of the  $\text{TiO}_2$  layers. In green, we show the reflectivity spectrum of a platform with a device layer of 60 nm-thick  $\text{TiO}_2$  with respect to  $n\sin\theta$ . The dip position in the reflectivity spectrum depends on the chosen parameters. Therefore, the device layer and the top layer thicknesses can be tuned in order to modify the effective index of BSW depending on the targeted application.



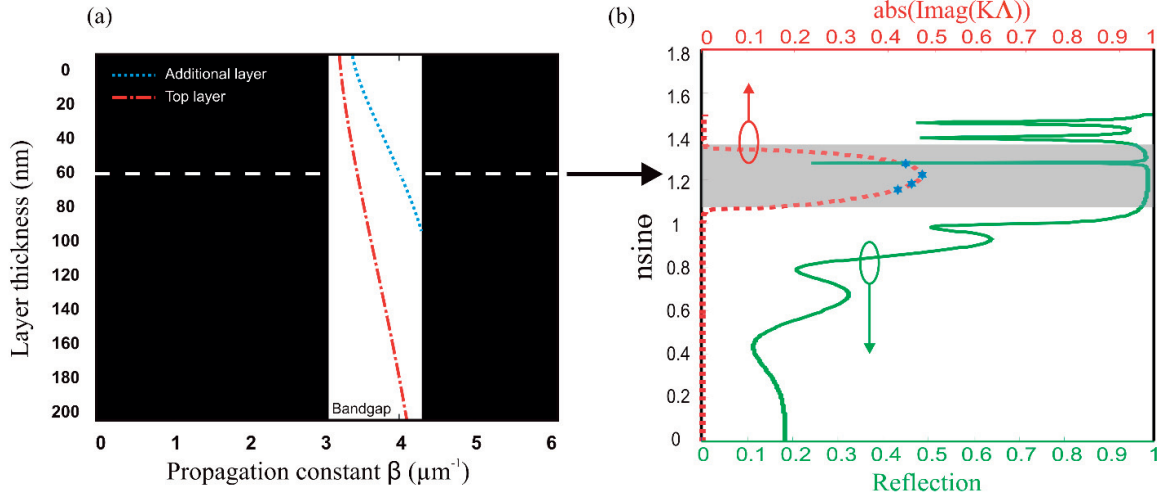


Fig.3.5 (a). Evolution of the propagation constant of the BSW mode with respect to the top layer thickness (red) and the device layer thickness (blue). (b) Reflection spectrum (green line) of 60 nm device layer  $\text{TiO}_2$  and position in the photonic bandgap (greyed surface). The red spectrum shows the product of the period of multilayer and the absolute values of the imaginary part of the BSW wave vector (in the multilayer) which is perpendicular to the direction of BSW propagation. The values are lower at the edges of the bandgap. Blue stars correspond to the values of the imaginary part of the BSW wave vector for 60 nm, 30 nm, 15 nm and 0 nm thicknesses of device layer of  $\text{TiO}_2$  in the direction toward decreasing  $n\sin\theta$  scale respectively.

### 3.2 Experimental set up for Bloch surface wave excitation and characterization methods

For the experiments done in this thesis, a total internal reflection (TIR) configuration is used for BSW coupling. The TIR configuration is needed for BSW excitation since its wave vector lies beyond the light line. Thus, it is not possible to couple the surface wave directly in air. A schematic of the total internal reflection configuration is shown in Fig.3.6. A BK7-glass prism is used for the coupling ( $n = 1.501$ ). The laser beam incidents at the prism at an angle  $\theta$  which is higher than critical angle. At a particular angle and wavelength, the incident light is coupled to BSW which can be seen as a reflection dip of the angular reflectance plot in the far-field (FF). The incident angle  $\theta$  is chosen so that the parallel component of the wave vector of the incident light matches the following condition,  $\beta = K\sin\theta$  where,  $K = 2\pi n / \lambda$  is the wave vector of the incident beam,  $n$  is the refractive index of the prism,  $\lambda$  is the wavelength of the incident light in vacuum and  $\beta$  is the propagation constant of the surface mode. The laser source is an external cavity diode laser



(Agilent, Model 81682A) tunable for wavelengths ranging from 1460 nm to 1580 nm. We use a focused Gaussian beam to couple light onto the surface of the multilayer. An incident beam illuminates the prism at an incident angle  $\theta$  at a specific wavelength. In our case, the horizontal spot diameter in the coupling zone is around  $30\ \mu\text{m}$ . The surface wave propagates in the  $x$ - $y$  plane as shown in Fig.3.6.

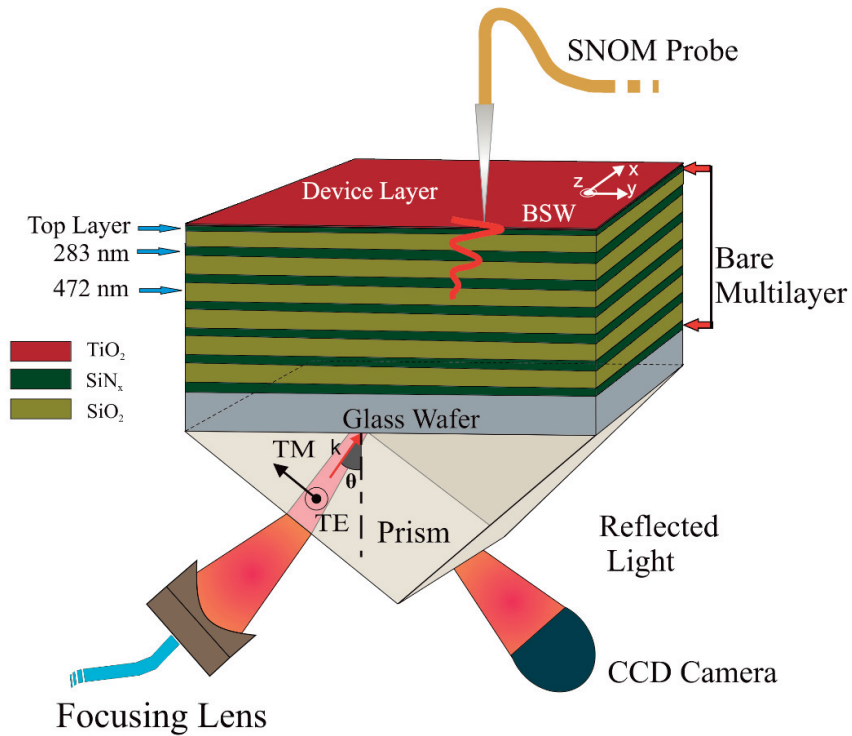


Fig.3.6. BSW coupling is performed with total internal configuration using a BK7-glass prism. The SNOM probe collects the evanescent field on top of the 2D structures. On the other side of prism, there is a CCD camera to collect the light reflected in the far-field.

Since a BSW is an evanescent mode, the near-field (NF) is collected by a MH-SNOM with a subwavelength aperture probe (in collection mode) appended to a single mode fiber. The working principle of MH-SNOM has been described in ‘Introduction’ chapter.

A schematic of the far-field experimental setup is shown in Fig.3.7. A collimated and TE-polarized beam is used to illuminate the sample through the input slant facet of a glass prism. The angular divergence of the collimated incident beam is measured (from the spot size) to be  $\phi = 0.0024$  rad. The sample is contacted with the prism flat facet using a proper index matching liquid. On the other side of the prism, the reflected light is collected by a Germanium photodiode detector.

The sample and the detector are placed on a rotational stage, which is driven by a stepper motor controller. The rotational stage is being used to rotate the sample with respect to the incident beam. The angle ' $\theta$ ' is measured between the normal to the multilayer planar interface and the direction of the incident beam at the prism. The angular reflectance profiles at a fixed wavelength are obtained by scanning a range of angles ( $\theta$ ).

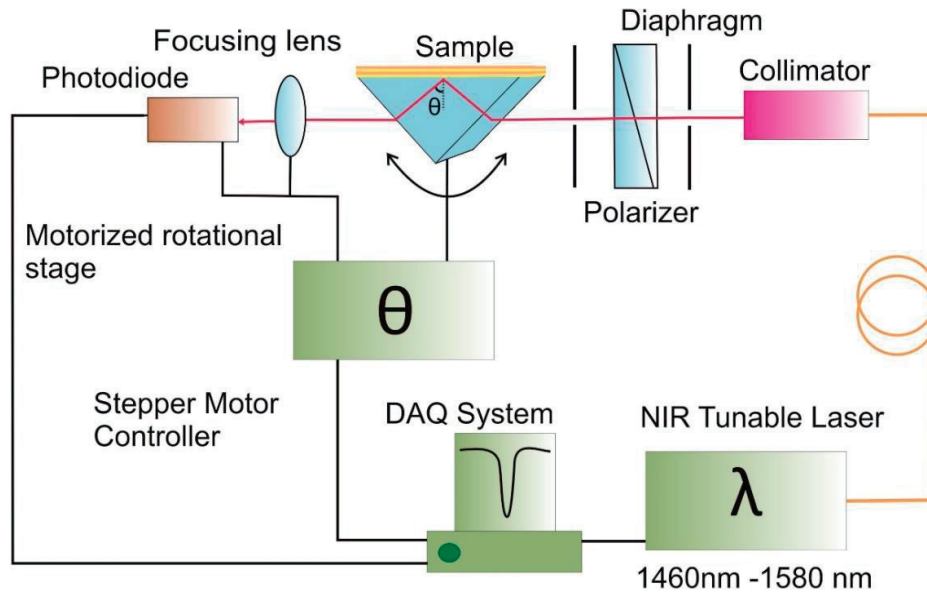


Fig. 3.7. Schematic of the far-field experimental set up in total internal reflection configuration used for far-field characterization of BSWs.

To design and study 2D optical components on the top of multilayer platform, we use commercial CST Microwave studio simulations based on the FDTD method. As 3D numerical simulation using FDTD method can be extremely time consuming on a medium sized server, the effective index approach is implemented to decompose the 3D model into two independent 1D and 2D models. Considering the fact that in the 2D devices, under investigation in this thesis, the vertical confinement dominates the lateral confinement of the surface mode, the properties of the surface mode are mainly determined by the vertical structure of the multilayer. Therefore, we opt for the vertical effective index approach to define the 1D model as an effective multilayer due to vertical confinement of surface mode. Further, 2D components are modeled considering the effective indices of BML and BML + device layer as an indices of background and the components, respectively. The simulations are performed with open boundary conditions and in-plane TE polarization state. The open boundary conditions define the finite expansion of the structure by

using a perfectly matched layer boundary. The simulations are adapted for mesh (hexahedral) size of  $\lambda/10$  wavelength.

### 3.3 Impact of device layer on Bloch surface waves propagation properties

#### 3.3.1 Propagation length analysis

As described in the constituent material section, the presented multilayer design supports TE polarization. In Figure 3.8 (a, b), the near-field image of BSW coupling for TE and TM polarization demonstrate this fact. The BSW propagation is only supported by TE polarization while TM-polarized field appears as an elongated Airy pattern of the focused illumination spot. The Airy field distribution is aroused because of the diffraction at the focuser entrance pupil. The illumination spot appears elongated because of the projection of the incident beam onto the multilayer surface. For TE polarization BSW propagates far from the coupling region in y direction. The shift in positive y direction of the maximum field amplitude of TE and TM polarizations can be noticed in Fig.3.8 (c). The Goos-Hanchen effect, which induces a spatial displacement of the focused light beam totally reflected from the interface of dielectric surface, is the reason behind aforementioned shift [73]. We visualize, in Fig.3.8 (c), the Goos-Hanchen shift which is enhanced by the coupling of BSWs for TE polarization [73]. For a particular coupling parameter, the positive shift can be estimated according to reference [66]. In our case, the coupling parameter propagation length /beam waist is  $\frac{L_{BSW}^{BML}}{w_0} \approx \frac{1350}{15} \approx 90$ . Based on the Ulrich's prediction at the given coupling factor, the positive shift in peak of field distribution is approximately  $y_m = 1.9 * w_0 = 28.5 \mu m$  [66]. The calculated shift is very close to the one observed experimentally which is  $30 \mu m$  (see Fig.3.8 (c)). The measurements for deducing  $L_{BSW}^{BML}$  are presented in the below paragraph. The calculated coupling parameter is very high ( $\frac{L_{BSW}^{BML}}{w_0} \approx \frac{1350}{15} \approx 90$ ) the estimated coupling efficiency is approximately 5 % according to [66].

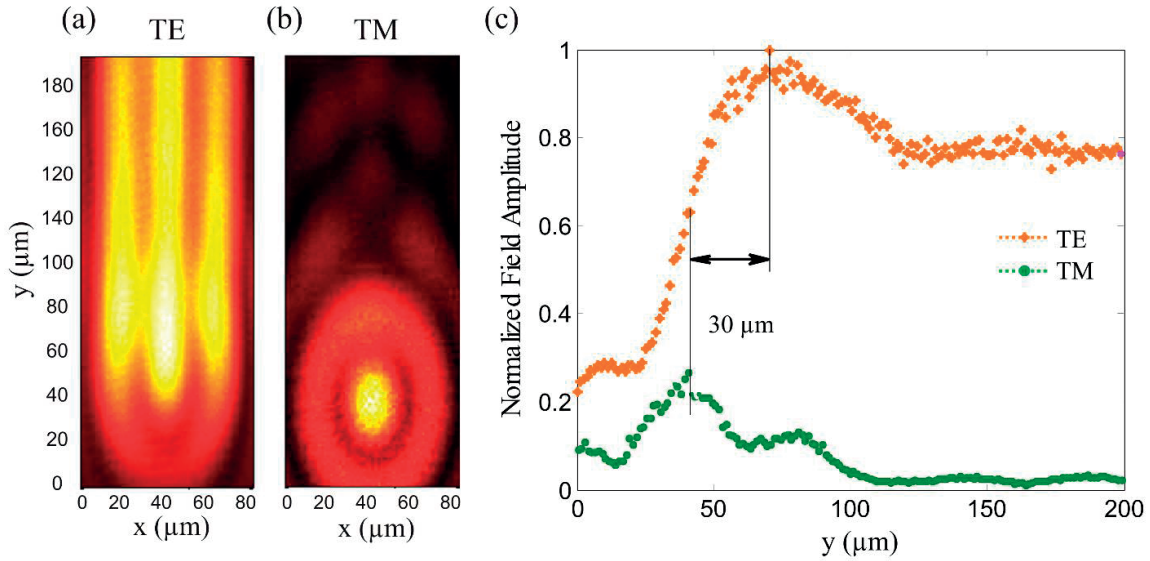


Fig.3.8. Near field MH-SNOM images of BSW propagation (a). When excited with TE polarization (b). When excited with TM polarization (c). The cross section of measured electric field amplitude for TE and TM polarizations as a function of propagation distance at coupling area.

As a BSW propagates along the surface, it loses energy to the multilayer system. Thus, the propagation length is an important property of a BSW. It is the distance where the amplitude of the propagating field drops down exponentially  $\left(\exp\left(-y/L_{BSW}\right)\right)$  to  $1/e$  of its maximum value. As described in the introduction, the main source of mode loss is the leakage into the multilayer because of the presence of the prism. The multilayer design is optimized for low losses by appropriately choosing the thicknesses and number of periods. The propagation lengths for the BML and BML with different thicknesses of the device layer ( $\text{TiO}_2$ ) are estimated by measuring the near-fields.

A near-field image of BSW propagation at wavelength 1558 nm is shown in Fig.3.9 (a). The image represents the field amplitude distribution of BSW propagation, where the evanescent field is collected by a MH-SNOM probe. The amplitude distribution map is analysed to deduce the BSW beam divergence and propagation length in  $x$  and  $y$  direction, respectively, as shown in Fig.3.9 (a).  $L_{BSW}$  is obtained by exponentially fitting the decrease of the field amplitude of the surface wave along the propagation direction where the region with maximum field amplitude represents the coupling zone, as demonstrated in Fig.3.9 (b). For 30 nm thickness of  $\text{TiO}_2$ , we achieve a propagation length of around  $L_{BSW}^{NF} = 3.24 \pm 0.13$  millimeters in the near-field, which is nearly 40 times longer than the recently obtained “Long-Range SPPs” studied by J. Lin *et al.* [12] and 5 times longer than the one studied by L. Yu *et al.* [45]. We have calculated an error margin using a standard

absolute error analysis method. Mainly, the divergence of the BSW and the surface quality influence the propagation length. Hence, error calculations include the divergence of the BSW, surface non-uniformity and also the reproducibility of the results. To determine the divergence of the propagating BSW, the full width half maximum (FWHM) of the measured beam profile (in x direction, Fig.3.9 (a)) is calculated at equidistant positions along the direction of propagation for one millimeter. For BML, the measured value of the divergence angle in the near-field is approximately 0.27 deg. Note that the perfect conformal coating provided by ALD insures a homogeneity of the layer thickness all over the sample even in tiny apertures. A small reduction of the surface roughness can also be observed for thicker layer [64] .

In the similar manner as explained above, the propagation lengths of the BSW, without a device layer (BML) and for other thicknesses of  $\text{TiO}_2$  are also measured at  $\lambda = 1558$  nm. Different thicknesses of the  $\text{TiO}_2$  layer are deposited on different BML samples with the same multilayer platform design. The measured propagation lengths for the BML, with 15 nm of  $\text{TiO}_2$ , 30 nm of  $\text{TiO}_2$  and 60 nm of  $\text{TiO}_2$  are  $1.35 \pm 0.09$ ,  $2.77 \pm 0.15$ ,  $3.24 \pm 0.13$  and  $2.53 \pm 0.14$  millimeters, respectively. The corresponding propagation losses in dB/mm ( $8.68/L_{BSW}$ ) are 6.42, 3.13, 2.68 and 3.43 dB/mm for the BML, with 15 nm of  $\text{TiO}_2$ , 30 nm of  $\text{TiO}_2$  and 60 nm of  $\text{TiO}_2$ , respectively. The propagation lengths with error margins are plotted against different thicknesses of  $\text{TiO}_2$  in Fig.3.9 (c). The rigorous calculations to deduce the  $L_{BSW}$  have been performed by M. Menotti *et al.* [59]. It has been explained that  $L_{BSW}$  is directly related to the  $\text{Imag}(K)$  and the number of periods of the multilayer. In the present design of the multilayers the value of  $\text{Imag}(K)$ , which controls the damping of the electric field in the multilayer, is maximum at the middle of the PBG (Referring to Fig.3.5 (b)). This implies, the evanescent field cannot penetrate deeper into the multilayer close to the middle of the band gap. Therefore  $L_{BSW}$  is longest in the middle of the PBG, since the leakage is the dominating propagation loss mechanism. For example, referring to the propagation length plot and the dispersion band diagram [Figs.3.4 and 3.9 (c) inset], the propagation length for a 30 nm-thick  $\text{TiO}_2$  layer is the longest compared to other thicknesses and the dispersion line lies at the middle of the bandgap.

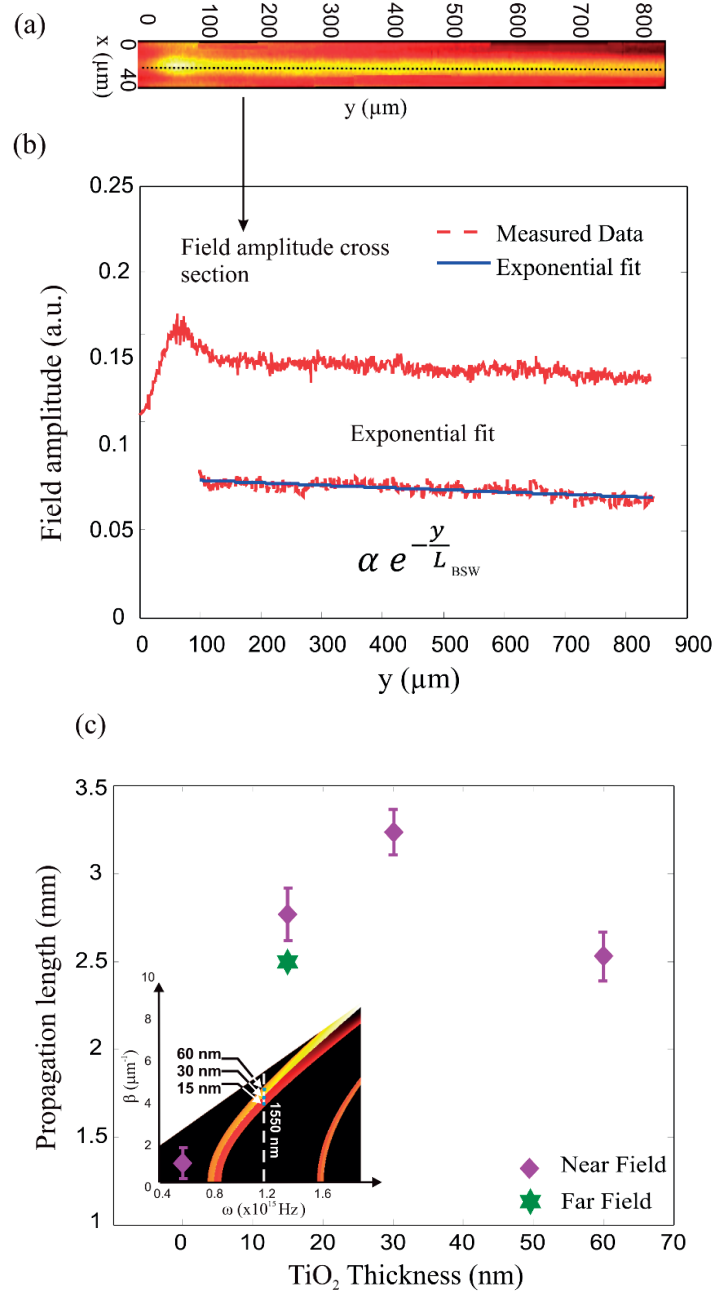


Fig.3.9 (a). MH-SNOM image demonstrating BSW propagation in the near-field. (b) Exponential fit of the field amplitude along the direction of propagation to measure the propagation length. (c) Near-field measurement of propagation lengths with the error margin for BML (0 nm TiO<sub>2</sub>), 15 nm of TiO<sub>2</sub>, 30 nm of TiO<sub>2</sub> and 60 nm of TiO<sub>2</sub> thicknesses.

The propagation length of prism-coupled waveguide modes can also be deduced from the bandwidth of reflectance anomalies, as described by Ulrich in [66]. The reflectance spectrum as a function of the incident angle  $\theta$  is measured using a far-field set up as explained under the methods section (see Fig.3.7). Notwithstanding, measured reflectance dips broaden significantly due to the angular divergence of the illuminating beam. In fact, for the given coupling system, the reflectance anomaly is a result of the convolution of the multilayer waveguide transfer function and the angular spectrum of the incident beam. In the far-field characterization method, we use a Gaussian beam whose measured angular divergence is about  $\phi = 0.0024$  rad. The corresponding beam waist is around  $w_0 = \lambda/\phi\pi = 206 \mu\text{m}$ . We remove the effect of the finite size of the beam width and estimate the FWHM of the reflectance curve, which is around  $\sigma = 2 \times 10^{-4}$ . As an example, we show here the propagation length of the BSW mode for the device layer of 15 nm  $\text{TiO}_2$ . The estimated value in the far-field for prism-film coupling systems is following [66] :

$$L_{BSW}^{FF} = \lambda/\pi\sigma = 2.5 \text{ millimeters} \quad (3.3)$$

Which is very close to the near-field propagation length of 15 nm of  $\text{TiO}_2$  ( $\sim 2.7$  millimeters).

As shown in Fig.3.6, the CCD IR camera is used to collect the reflected light in the far-field. The m-line pattern can be observed in a prism coupling arrangement [74]. These m-lines intersect the focused spot produced by total internally reflected incident light and generate the specific fringe pattern, as shown in Fig.3.10.

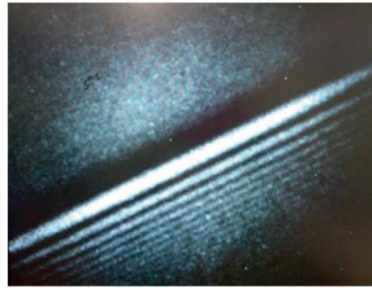


*Fig.3.10. M-line pattern observed in far-field image of the reflected light captured in CCD camera in TIR coupling set up.*



With increasing coupling strength these lines become first brighter and then broader [74]. The fringe pattern can also be understood as an interaction of total internally reflected incident beam and leaky propagating surface wave [75]. The reflected beam is a divergent Gaussian beam while the leaky surface wave is more flat. The intersection of two wave-fronts having different curvatures produce the interference pattern. More the waist difference of these two interfering beams, larger would be the difference in wave-front curvatures of these beams after propagating some distance and hence more pronounced fringes pattern.

### 3.3.2 Analysis of evanescent field in external medium

As discussed in chapter 1, the BSW decays exponentially in the external medium. The strong evanescent field content indicates the strong interaction with the external medium and hence enhanced sensitivity [56]. Here, the sensitivity is defined as the shift in the resonance wavelength of BSW with respect to the variation in refractive index of the external medium. The length of the exponential tail depends on the difference between the coupling angle  $\theta$  and the critical angle  $\theta_C$ , the smaller the difference the longer the field tail, according to following formula [8].

$$L_{PD} = \frac{\lambda}{2\pi\sqrt{(n_P \sin \theta)^2 - (n_e)^2}} \quad (3.4)$$

Where,  $n_P$  and  $n_e$  are the refractive indices of prism and external medium (which is air in our case) respectively, and  $\theta$  is the incident angle for BSW coupling for different thicknesses of TiO<sub>2</sub> and  $\lambda$  is a wavelength of incident light.  $n_e$  can be reformulated as :  $n_e = n_P \sin \theta_C$ .

We calculate the penetration depths,  $L_{PD}$ , of the evanescent field in the air for BML, 15 nm layer of TiO<sub>2</sub>, 30 nm layer of TiO<sub>2</sub> and 60 nm layer of TiO<sub>2</sub>. The calculated values are 436.8 nm, 398.13nm, 363.6 nm and 312.8 nm for BML, 15 nm, 30 nm and 60 nm of TiO<sub>2</sub> respectively at  $\lambda = 1558$  nm. It can be inferred that the sensitivity to the external medium would be more for BML than the multilayer with device layer of TiO<sub>2</sub> 60 nm. The field profile of the surface mode as a function of multilayer platform thickness for different thicknesses of TiO<sub>2</sub> layer is presented in Fig.3.11. The field profile has been calculated using CST simulations (FDTD method). It can be noticed in the zoomed image that evanescent tail decays fastest for 60 nm layer of TiO<sub>2</sub>. As the coupling angle of TiO<sub>2</sub> 60 nm is largest, the field profile showing short penetration depth is in accordance with theory.



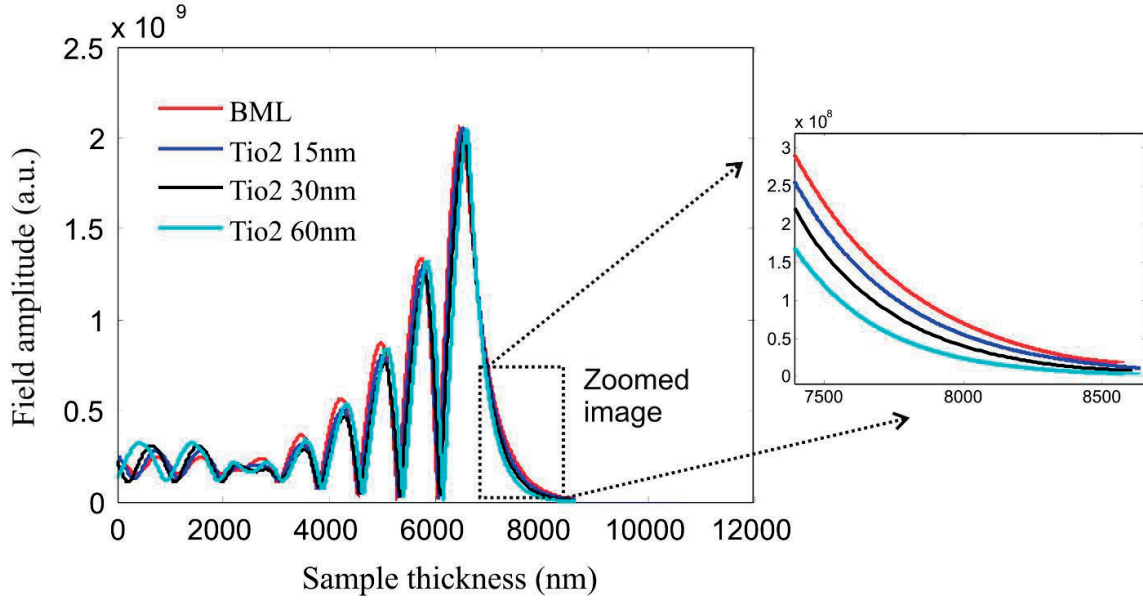


Fig.3.11. The Simulated field- profile of the BSW as a function of multilayer platform thickness for different thicknesses of  $\text{TiO}_2$  layer. The simulation are performed using CST microwave studio.

It is known that the amplitude of the electric field on the multilayer interface depends on the vertical confinement of BSWs. The vertical confinement can be increased by tailoring the device layer thickness properly. The tighter confinement results in an electromagnetic field enhancement [76]. We measure the field enhancement associated to BSW coupling. It can be measured in different ways. In general, TM polarization can be used as a reference to measure the field enhancement when BSW is excited for TE polarization. This may not be the correct method to measure the absolute value of field enhancement as TM polarization may have a particular response to the multilayers. However, for the relative comparison study of the field enhancement for BML and BML with device layer, TM polarization can be used as a reference. Therefore, we measure the field enhancement of TE polarized light with respect to TM polarization. For BML, the field amplitude on the surface is enhanced nearly 4 times more than the field for TM polarization (see Fig.3.8). However, for 60 nm thickness of  $\text{TiO}_2$  layer the field enhanced 3 times.

### 3.3.3 Effective refractive index analysis

An effective refractive index  $n_{\text{eff}}$  is introduced by the propagation constant of surface waves. When the multilayer is coated with ultra-thin films, the effective refractive index shifts to a higher value creating a contrast between the BML and the coated multilayer. The refractive index contrast ( $\Delta n$ ) mainly affects the capability to manipulate the BSW. The refractive index contrast, produced by

optical elements on the top of the multilayer, plays a key role in determining the optical properties of the surface photonic devices and hence their efficiency in the manipulation of the BSW. High  $\Delta n$  provides strong lateral confinement of the light inside the waveguide structures and enables the development of compact and low loss integrated 2D photonic devices. Here, we measure  $\Delta n$  of the propagating BSW for different thicknesses of  $\text{TiO}_2$  in near-field and far-field at  $\lambda = 1558$  nm. To perform this measurement in the near-field, a high resolution map of the phase is acquired using the MH-SNOM. From a phase cross sectional profile, shown in Fig.3.12, one can calculate the effective refractive index contrast using simple transformations in the Fourier domain:

$$\lambda_{eff} = \frac{1}{f_s} = \delta,$$

$$n_{eff} = \frac{\lambda}{\lambda_{eff}} = \frac{\lambda}{\delta} = \lambda * f_s, \quad (3.5)$$

$$\Delta n = n_{\text{TiO}_2} - n_p,$$

where  $f_s$  is the spatial frequency,  $\delta$  is the period of the phase diagram,  $n_{\text{TiO}_2}$  and  $n_p$  are the effective refractive indices with and without the  $\text{TiO}_2$  layer (BML platform), respectively.

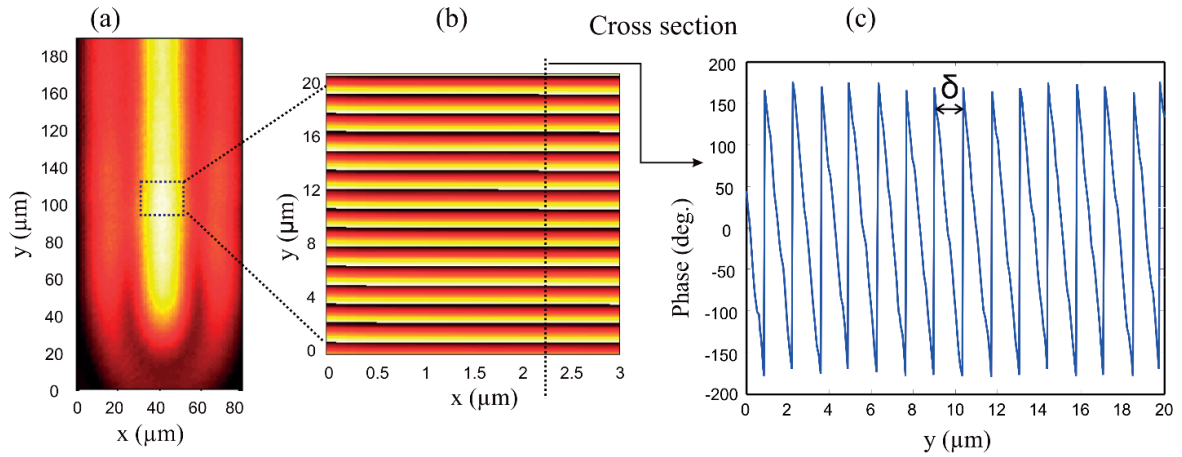


Fig.3.12 (a). Near-field MH-SNOM image of BSW propagation. (b) High resolution (400 points in  $20\mu\text{m}$  scan length) map of phase along the direction of BSW propagation. (c) Cross section of BSW phase along the propagation direction.

The spatial frequency ( $f_s$ ) can be deduced by performing Fourier transformation of high resolution 2D data [39]. The accuracy in the values of  $f_s$  depend on the scan length  $L$  as,  $\Delta f_s = \frac{1}{L} = \frac{1}{20\mu m} = \pm 0.05\mu m^{-1}$ . In the near-field, a  $\Delta n$  of 0.15 has been obtained for a 60 nm thick  $TiO_2$  layer which is significantly higher than the 100 nm thick layer of photoresist [45].

The values of  $n_{eff1}$  (BML) and  $n_{eff2}$  (BML + 60 nm  $TiO_2$  layer) used in the thesis are 1.14 and 1.26, respectively.

In addition,  $n_{eff}$  has also been measured in the far-field. The far-field set up has been discussed under the methods section (see Fig.3.7). Figure 3.13 (a) shows a typical reflectance spectrum as a function of the prism incident angle  $\theta$ . The red curve corresponds to the bare multilayer where there is no device layer. The yellow and green curves correspond to the 15 nm and 60 nm-thick  $TiO_2$  device layers, respectively. The result plots only a small angular range in the vicinity of the reflectivity dip. The dips correspond to the Bloch surface modes propagating at the multilayer-air interface. By adding the device layer, the surface mode is moved to the middle and to the lower edge of the bandgap thus to larger parallel wave vectors expressed with a high incident angle.

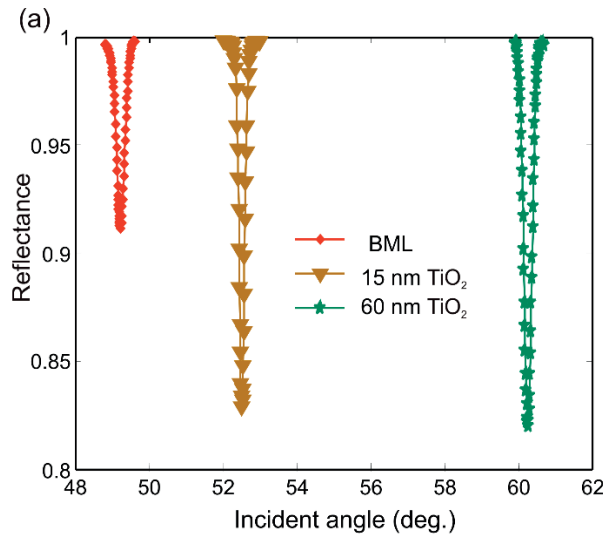


Fig.3.13 (a). Reflection as a function of the incident angle for different  $TiO_2$  layer thicknesses, measured in the far-field.

The effective refractive index,  $n_{eff} = n \sin \theta$ , can be deduced from the dip of the reflectance for the different  $TiO_2$  layer thicknesses. A maximum effective refractive index contrast  $\Delta n = 0.16 \pm 0.01$  is obtained for 60 nm thickness of  $TiO_2$ . The error margin is introduced from the calibration

of the incident angle  $\theta$ . The resolution of the stepper motor is 0.0025 deg/step. The calculated error in  $n_{eff}$  is,  $\Delta n_{eff} = n \Delta \theta \cos \theta$ .

Using matrix transfer method, the far-field reflectance spectrum of the multilayer platform with different set of  $\text{TiO}_2$  thicknesses is calculated at  $\lambda = 1558 \text{ nm}$ , as shown in Fig.3.13 (b). The  $n_{eff}$  and  $\Delta n$  are deduced from the reflection dips for different thicknesses of  $\text{TiO}_2$ , using similar method as explained in far-field measurement section.

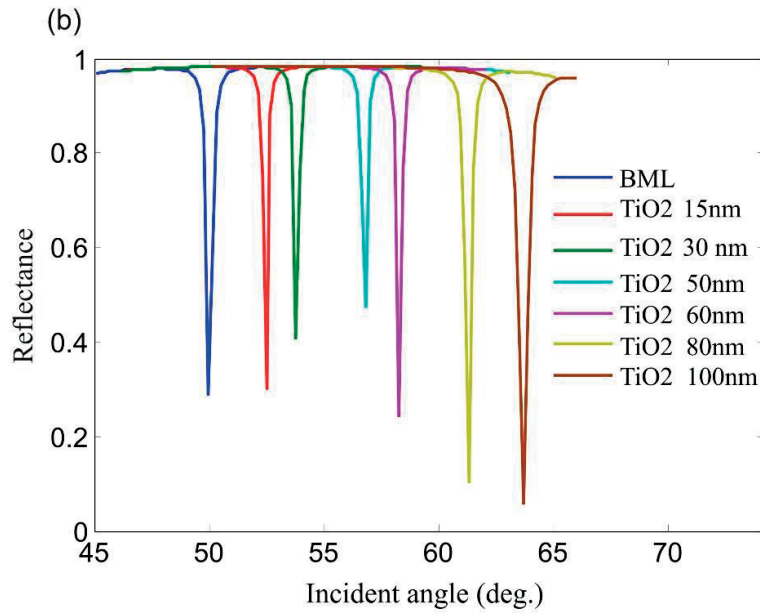


Fig.3.13 (b). The reflection spectrum calculated using matrix transfer method for different thicknesses of  $\text{TiO}_2$  on the top of multilayers platform. The  $\text{TiO}_2$  layer thickness is varying from 0 – 100 nm.

We plot the theoretical (matrix transfer method), the near-field and the far-field measurement results of  $\Delta n$  as a function of the  $\text{TiO}_2$  thicknesses in Fig.3.13 (c). The experimental and theoretical results show a good agreement with each other. The simulation results show that a  $\Delta n$  close to 0.2 can be achieved for 100 nm of  $\text{TiO}_2$  thickness.

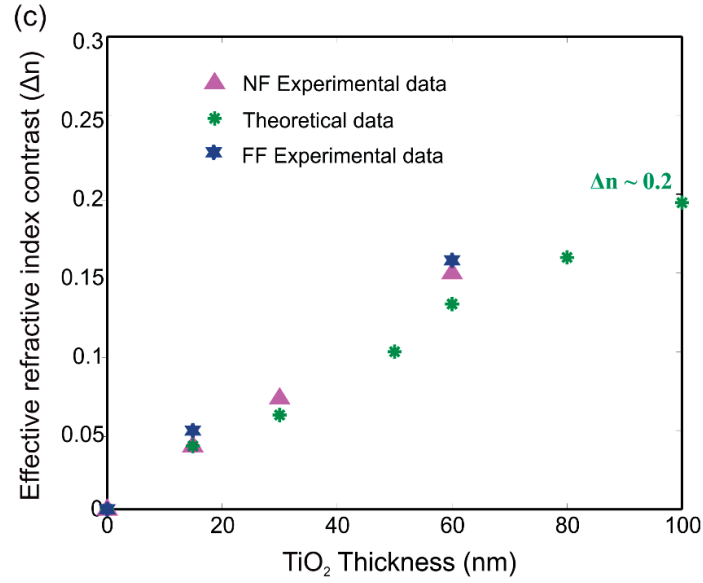


Fig.3.13 (c) The effective refractive index contrast of a BSW for different thicknesses of TiO<sub>2</sub> layer (from 15 nm to 100 nm) in near-field (NF), theory and far-field (FF).

### 3.4 Conclusion

The propagation lengths of Bloch surface waves at the interface of a multilayer platform are studied experimentally. The objective of the study is to have more insight to design BSW based 2D optical integrated systems. Different device layer thicknesses of a high refractive index material, in our case TiO<sub>2</sub>, are investigated. Another important property of BSW, for example the effective refractive index, is studied and presented. These properties are measured in the near-field and far-field. The near-field characterization is done with the aid of a multi-heterodyne scanning near field optical microscope and the far- field by measuring the incident angle at resonance. We measure the influence of the thickness and refractive index of the device layer on the propagation properties of BSWs. A longer propagation length (3.24 millimeters) is achieved near to the middle of the photonic band gap where theory suggests the stronger attenuation. However, this is not the limit, higher values (in the order of centimeters) might be achieved using grating couplers. Most importantly, by tailoring the thickness of the device layer a surface mode can be shaped according to the application, for example integrated optics or sensing. High refractive index is preferred for low loss and compact photonic devices. We achieve a  $\Delta n$  close to 0.15 for 60 nm of TiO<sub>2</sub>. The theoretical results demonstrate that we can reach a  $\Delta n$  close to 0.2 for 100 nm thickness of TiO<sub>2</sub>. The experimental results show a good agreement with the theoretical results. In addition to the

valuable increase of the propagation length of the BSW, we also demonstrate that a device layer allows fine tuning of the BSW frequency, which can thus be positioned at any place within the photonic band gap. These novel features make the BSW based multilayer platform more efficient for further integrated photonics applications. Considering the strong interest in BSWs, we believe that the presented results can provide a better perception to design application oriented devices.

Most of the results of this chapter are published in Paper [2] of journal publications in the list of appendices.



# CHAPTER 4

## Bloch Surface Waves based 2D disk resonator

This chapter presents the first experimental investigation of a two-dimensional disk resonator on a dielectric multilayer platform sustaining Bloch surface waves. The disk resonator is patterned into a few tens of nanometer thin ( $\sim\lambda/25$ ) titanium dioxide layer deposited on the top of the platform. We characterize the disk resonator by multi-heterodyne scanning near field optical microscopy. The low loss characteristics of Bloch surface waves allowed us to reach a measured quality factor in an order of three for a disk radius of 100  $\mu\text{m}$ .

Dielectric micro-ring and disk resonators are the part of the key building blocks of nowadays integrated optical systems. They have been extensively studied theoretically [77], [78] and demonstrated later experimentally[79]. These structures can indeed be used as channel-drop filters, all-optical logic gates, optical frequency division multiplexers and light sources [80], [81]. Moreover, resonators also find application in sensing [82].

The resonator based surface plasmon-resonance (SPR) sensors, which use surface plasmon waves to probe the interactions between molecules and sensor surfaces, have been studied rigorously in the past for optical detection of small chemical and biological entities. These include the low propagation loss channel plasmon subwavelength waveguide ring resonators [14], nanoscale rectangular resonators utilizing zero sharp bend loss, Metal-Insulator-Metal (MIM) waveguides [83], and plasmonic ring resonator with array of silver nanorods as waveguides [84]. Efforts are put on the improvement of the quality factor of the structure which is one of the main measures of the efficiency of the ring/disk resonators. For example, dielectric-loaded plasmonic waveguide-ring resonators have been introduced where dielectric stripes deposited on a smooth metal film are used as waveguides[85]. A high-Q plasmonic cavity composed of a silica core where light is trapped inside the thick disk has been realized [86]. Finally, ring resonators with hybrid waveguide consisting of a dielectric nanowire on a silver layer have been studied[15]. The advantage of SPR is the strong confinement of the electric field. However, because of the high



absorption losses of metals, SPR sensors suffer from very low quality factors, which limits the sensitivity of the device.

In this study we utilize this low loss dielectric platform as a foundation for the design of BSW based resonators. The resonator devices based on the surface waves take advantage of the light confinement on the surface and hence achieve high sensitivity for the surface environment. One advantage of our BSW based resonator is the possibility of a high  $Q_0$  factor, in comparison to plasmonic based resonators exhibiting  $Q_0$  factors on the order of  $10^2$  [15], [84], [85], [87]. This is mainly due to the low loss characteristic of BSW.

## 4.1 Fundamental concept of optical resonator

An optical resonator is basically a closed loop waveguide which acts as a cavity to localize the energy at certain wavelengths for a considerably long time compared to the photon time period. The localization of the light can be distributed in two different categories: spatial and temporal localization.

The spatial localization of the light is represented by field distribution of the resonator mode, localized at the perimeter of the cavity. A smaller mode volume can be obtained with high refractive index contrast between the resonator and its surrounding media.

The temporal localization of energy in a resonator is defined by photon lifetime ( $\tau_0$ ) inside the cavity. Photon life time can be also related to the quality factor ( $Q_0$ ), which will be discussed later. The photon life time is limited inside the cavity. The limiting factors to have long photon life time are: first, resonator geometry which can not completely confine the propagating mode. The mode inside the cavity propagates following total internal reflection (TIR) mechanism at the sidewall of the cavity. Because of the finite curvature of the sidewall of the resonator, TIR is not perfect and as a result of which there is always some energy leaking outside the cavity through sidewalls. Second, leakage losses related to BSW propagation in our case, where BSW coupled back to prism while propagating on the surface of multilayer. Third, fabrication imperfections which causes scattering losses. The prominent point in designing a resonator is to minimize the losses, maximize the photon life time and increase the  $Q_0$  factor.

The spectral linewidth of the resonance spectrum for the resonator corresponds to temporal localization of energy. In other words, narrower spectral linewidth ( $\Delta\omega$ ) means larger  $Q_0$  factor and hence a longer temporal localization of energy as [88]

$$\Delta\omega = \frac{\omega_0}{Q_0} = \frac{2}{\tau_0} \quad (4.1)$$

The constructive interference or resonance in the cavity occurs at a specific wavelength and at the following condition:

$$2\pi R * n_{eff} = m\lambda, \quad (4.2)$$

Where  $\lambda$  is the resonance wavelength,  $n_{eff}$  is the effective index of the mode propagating inside the cavity, and  $m$  is the azimuthal mode number. This state is called On-resonance condition.

#### 4.1.1 Quality factor ( $Q$ factor)

The quality factor is a figure of merit of resonator. It is defined as

$$Q_0 = \omega_0 \frac{\text{Stored energy}}{\text{Power lost}} \quad (4.3)$$

$$Q_0 = \frac{\omega_0 \tau_0}{2} \quad (4.4)$$

The derivation of the equations can be found elsewhere [88].

#### 4.1.2 Free-Spectral Range (FSR)

The resonance wavelength/frequency spacing for two consecutive  $m$  numbers is called free-spectral range (FSR) of the resonator. It is defined as follows [88]:

$$FSR = \frac{\lambda_0^2}{n_g 2\pi R} = \frac{\lambda_0^2}{c T_{roundtrip}} \quad (4.5)$$

Where  $n_g$  is a group index and  $T_{roundtrip}$  is total time of round trip, and  $c$  is a speed of light in vacuum.

### 4.1.3 Finesse

The ratio of the FSR and the spectral linewidth of the resonance of the resonator is defined as Finesse [88].

$$Finesse = \frac{FSR}{\Delta\lambda} \quad (4.6)$$

Where  $\Delta\lambda$  is spectral linewidth of the resonance.

### 4.1.4 Waveguide coupling regimes

In our case, we use waveguide coupling configuration with a disk. The waveguide is placed enough closed to the disk that light from the waveguide evanescently coupled disk. Similar to intrinsic quality factor  $Q_0$ , we can define a quality factor for the waveguide-resonator coupling as  $Q_c = \omega_0 \tau_c / 2$  [88]. The total quality factor  $Q$  can be expressed as

$$\frac{1}{Q} = \frac{1}{Q_0} + \frac{1}{Q_c} \quad (4.7)$$

$Q_c$  depends on the coupling coefficient between waveguide and the disk. Based on the coupling coefficient and hence the ratio of  $Q_0/Q_c$  different coupling regimes can be defined.

#### 4.1.4.1 Critical coupling regime

When  $Q_0 = Q_c$ , the magnitude of the transmission spectrum approaches to zero at resonance. The resonance condition is called critical coupling.

#### 4.1.4.2 Under-critical coupling regime

In under-critical coupling regime,  $Q_0 < Q_c$ . In this regime, the magnitude of transmission is non-zero at resonance and the spectral linewidth of the transmission becomes narrower than the case of critical coupling regime.

#### 4.1.4.3 Over- critical coupling regime

The over-critical coupling regime is characterized with  $Q_0 > Q_c$ . Similar to under-coupling regime, here the magnitude of transmission is non-zero at resonance, however the spectral linewidth of the transmission gets broader than the case of critical coupling regime.

## 4.2 Simulation Results

We perform CST simulations using an FDTD method to calculate the resonance spectrum of the disk resonator. The simulations exploit effective index approach to design 2D system. The resonator has been designed with material with  $n_{eff\_2}=1.26$  (effective index of BML+ device layer) embedded in a surrounding medium with  $n_{eff\_1}=1.14$  (effective index of BML).

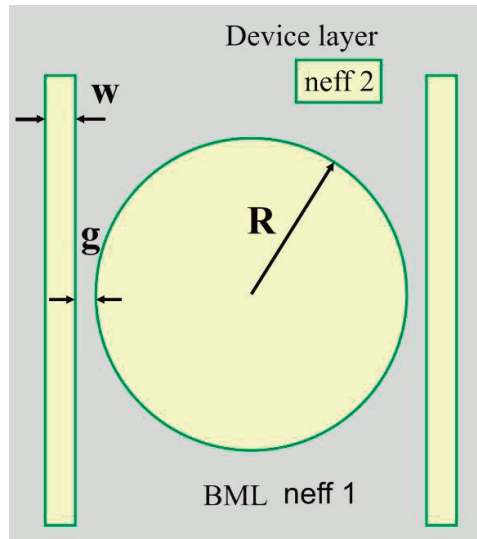


Fig.4.1. Schematic of disk resonator in two waveguide geometry.  $R$  is the radius disk,  $w$  is waveguide width and  $g$  is gap spacing between waveguide and disk. The resonator is fabricated in a device layer of  $\text{TiO}_2$ .

The disk resonator studied in this article consists of a disk having a radius  $R$  coupled to two straight bus waveguides of width  $w$ . The distance separating the disk and the waveguides is defined as the gap  $g$  (see Fig.4.1). The value of the measured effective refractive index for 60 nm of device layer of  $\text{TiO}_2$  layer is  $\Delta n$  ( $n_{eff\_2} - n_{eff\_1}$ ) approximately 0.12, which is sufficient to guide the BSW inside the disk of radius 100  $\mu\text{m}$  without significant bending loss.

The simulations are performed for disk radii of  $R = 40 \mu\text{m}$  and  $100 \mu\text{m}$ . For a disk radius  $R = 40 \mu\text{m}$ , waveguide width  $w = 2 \mu\text{m}$  and a gap of  $g = 500 \text{ nm}$ , the calculated  $Q_0$  factor from the transmission spectrum is approximately  $2 \times 10^3$ . Further, the transmission spectrum for the disk  $R = 100 \mu\text{m}$ , waveguide width  $w = 2 \mu\text{m}$  and  $g = 500 \text{ nm}$  is calculated (see Fig.4.2). The transmission at the through port has been calculated for the wavelength range of  $1540 \text{ nm} - 1580 \text{ nm}$ .

$$Q_0 = \frac{\lambda_0}{\Delta\lambda} \approx 2 \times 10^4 \quad (4.8)$$

$$FSR = 3.0 \text{ nm} \quad (4.9)$$

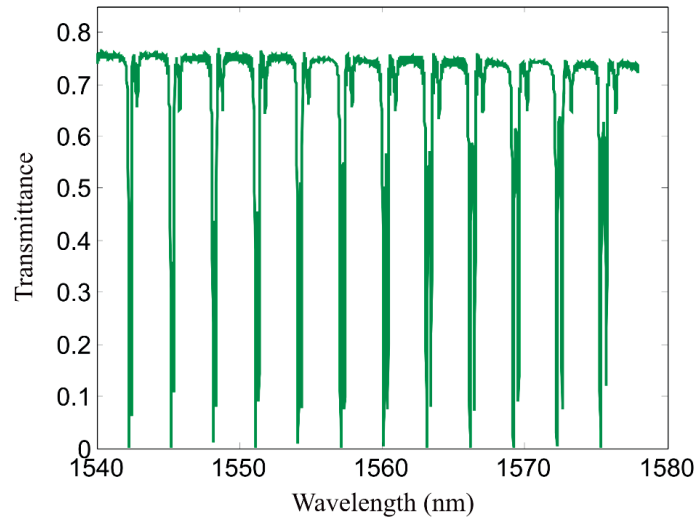


Fig.4.2. The calculated transmission spectrum at through port of disk radius  $R = 100 \mu\text{m}$  and gap  $g = 500 \text{ nm}$  resonator using FDTD method, CST simulations.

The resonance-splitting effect (in Fig. 4.2) is the result of coupling between degenerated modes of the resonator [88]. The coupling between degenerated modes is originated due to segmental structure of the periphery of the disk in simulation design. The simulated field amplitude distribution over the complete disk at On/Off-resonance condition ( $\lambda_0 = 1554.1 \text{ nm} / \lambda_0 = 1556 \text{ nm}$ ) is shown in Fig.4.3 (a, b). The calculated FSR and  $Q_0$  factor for the disk of radius  $100 \mu\text{m}$  and a gap of  $g = 500 \text{ nm}$  is following:

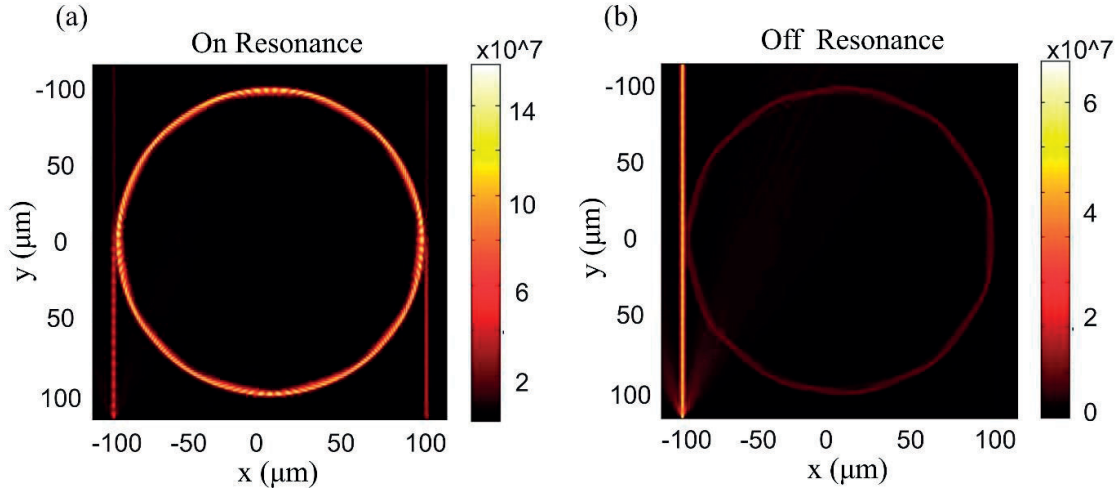


Fig.4.3. The CST simulation images of field amplitude distribution over the disk of radius  $R=100$  waveguide and  $g=500$  nm, (a) at On-resonance,  $\lambda_0 = 1554.1$  nm (b) at Off- resonance  $\lambda_0 = 1556$  nm.

It should be noted that in simulations scattering losses, fabrication imperfections and leakage losses are neglected. In experimental condition, which allows all types of losses, the quality factor might be degraded strongly. To study the effect of gap spacing on the performance of the disk resonator, the simulation with gap spacing of  $1\text{ }\mu\text{m}$  has been performed. We observed that the extinction ratio dropped significantly for  $1\text{ }\mu\text{m}$  gap spacing. The results can be found in appendix Fig.1. As a result of simulations, a disk radius  $R=40\text{ }\mu\text{m}$  and  $100\text{ }\mu\text{m}$ , a bus waveguide width  $w=2\text{ }\mu\text{m}$ , and a gap  $g=500$  nm are considered for experimental investigation.

### 4.3 Design concept

A 2D micro-disk resonator is patterned into  $60\text{ nm}$  thick device layer of  $\text{TiO}_2$ . The thickness of the device layer is chosen to compromise between refractive index contrast and propagation length with the present configuration and material. Note that the value of the refractive index contrast is not a limitation. The platform and the resonator are constitute of dielectric materials with low absorption in the near-infrared wavelength range. However, BSW may leak out of the multilayer because of the presence of prism [66], which is the predominant cause of the damping of the resonating surface mode.

A disk resonator is introduced because it has less losses compared with a ring resonator. As in disk resonators light interacts only with one sidewall (in comparison with ring resonators), the travelling mode suffers less scattering losses from the sidewall roughness. As a result we expect

that the quality factor of a disk resonator should be higher than its ring resonator counterpart. In optical resonators with high refractive index contrast between cavity and ambient (like silicon photonics) resonators with smaller bending radius and high quality factors can be realized [89]. In these cases, ring resonators have the advantage of restraining higher-order radial modes, because the electromagnetic field propagating inside the cavity is circumscribed by two sidewalls of the ring and higher-order radial modes are pushed to interact severely with the inner sidewall of the ring and forcibly radiate [88].

Since in BSW based optical resonators the refractive index contrast is much lower than silicon photonics, the radius of the resonator needs to be much larger. For the same reason, higher-order radial modes are strongly radiative and lossy. As a result, it is expected that a disk resonator, patterned into  $\text{TiO}_2$  layer, with a radius of  $100\text{ }\mu\text{m}$  does not severely suffer from higher-order radial modes. The experimental results, which will be presented, in the near field characterization section verify this fact.

## 4.4 Fabrication technique

The disk resonator studied in this article is fabricated on the top of dielectric multilayer platform into a  $60\text{ nm}$  thick  $\text{TiO}_2$  device layer. The scanning electron microscope (SEM) image of the fabricated resonator is shown in Fig.4.4. To realize the final etching of the disk resonator pattern, a chromium (Cr) mask has been used. The Cr layer was evaporated (LAB18 by Kurt. J. Lesker) and a resist (HSQ) layer was spun on the deposited multilayer. The structures were patterned to the resist by electron beam (EBL, Vistec EBPG 5000+ ES HR). After that, development of the resist was done in a solution of AZ 351: $\text{H}_2\text{O}$  (1:3) developer. The mask was created by etching the Cr layer by Inductively Coupled Plasma Reactive Ion Etching process (ICP-RIE, PlasmaLab 100 by Oxford). The ICP-RIE process involved chlorine ( $\text{Cl}_2$ ) and oxygen ( $\text{O}_2$ ) as process gases. Finally, the thin  $\text{TiO}_2$  layer was etched by ICP-RIE process (PlasmaLab 80 by Oxford) with sulfur hexafluoride ( $\text{SF}_6$ ) and argon (Ar) as etching gases. The remaining Cr was finally removed by wet etching.



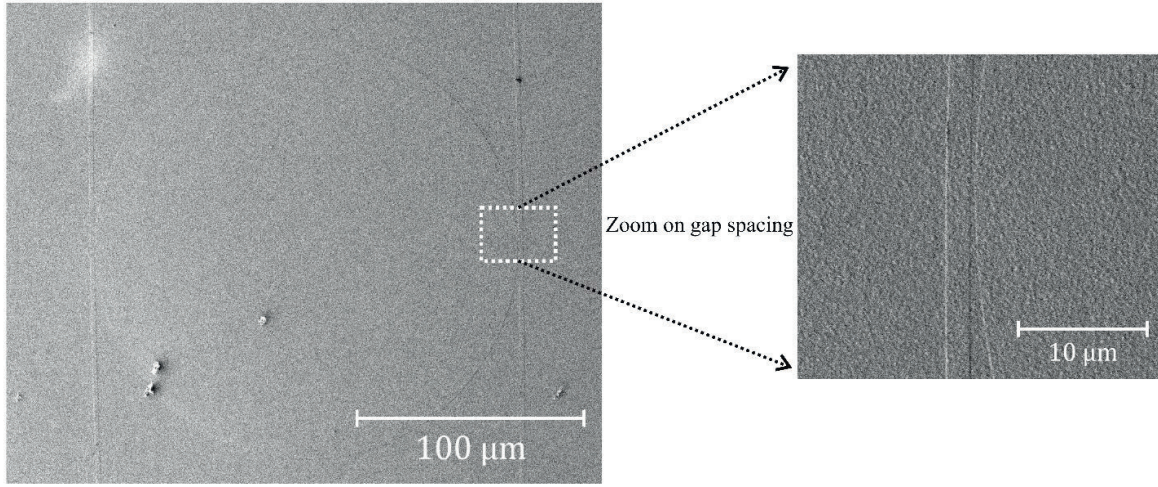


Fig.4.4. SEM image of disk resonator of  $2\ \mu\text{m}$  waveguide width and  $100\ \mu\text{m}$  disk radius, with a zoom on  $500\ \text{nm}$  gap spacing.

## 4.5 Near Field characterization

The incident beam illuminates the multilayers through prism at an oblique incident angle which is higher than critical angle,  $58.26^\circ$ . At this chosen angle, the incident beam is coupled to the BSW for  $60\ \text{nm}$  thick of  $\text{TiO}_2$  layer. Further, the generated BSW itself coupled to the first waveguide (input port). We keep the BSW coupling zone around  $100\ \mu\text{m}$  away from the coupling area between the waveguide and the disk (see Fig.4.5). This allows the incident light to propagate some distance in order to arise as a BSW mode, therefore to increase signal to noise ratio. The BSW propagates through the waveguide and couples to the disk at the coupling area, evanescently through the gap. Constructive interferences occur when the optical path of a round trip of the disk resonator is an integer multiple of the wavelength (Eq.4.2) and hence light builds up inside the disk. The On-resonance condition yields a dip in the signal collected at the through port.

The field amplitude distribution over the disk resonator is detected with a MH-SNOM in collection mode, where the subwavelength aperture probe is connected to a single mode fiber. To measure the transmission spectrum at the through port, we perform a scan, in wavelength and space, across the bus waveguide ( $x$ -direction) at a distance around  $100\ \mu\text{m}$  away from the coupling area along the  $y$ -direction, see Fig.4.5.



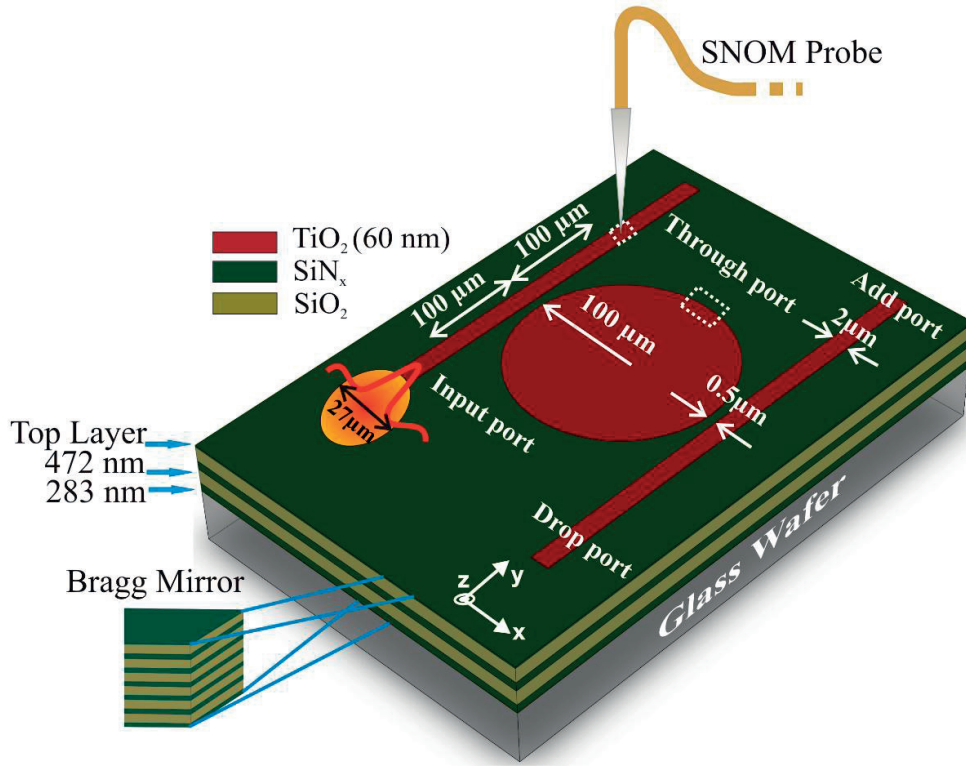


Fig.4.5. Schematic of the dielectric multilayers platform with 2D disk resonator designed on the top of it. The disk resonator has been patterned into 60 nm thick layer of  $\text{TiO}_2$ . BSW coupling zone is shown in red, which is 100  $\mu\text{m}$  away from the gap area. SNOM probe in collection mode is used for near field characterization of the disk resonator.

The near field SNOM image of the field amplitude distribution over the cross section of the waveguide for different wavelengths is shown in Fig.4.6 (a). The range of wavelengths spans from 1551 nm to 1561 nm which covers five FSR of the resonating BSW mode. The transmission spectrum at the periphery of the disk is measured in the same manner as described for through port, where fringes in  $x$  direction presents the azimuthal mode distribution of the resonating wave along 6  $\mu\text{m}$  length of disk periphery, refer to Fig.4.6 (b). Each row represents the field amplitude distribution of the azimuthal mode at corresponding wavelengths, in the image of periphery scan (see Fig.4.6 (b)). The slight difference in the positions of maxima in each row, in the amplitude distribution at the periphery, indicates the effect of different wavelengths on azimuthal mode number (see Eq. (4.16)).

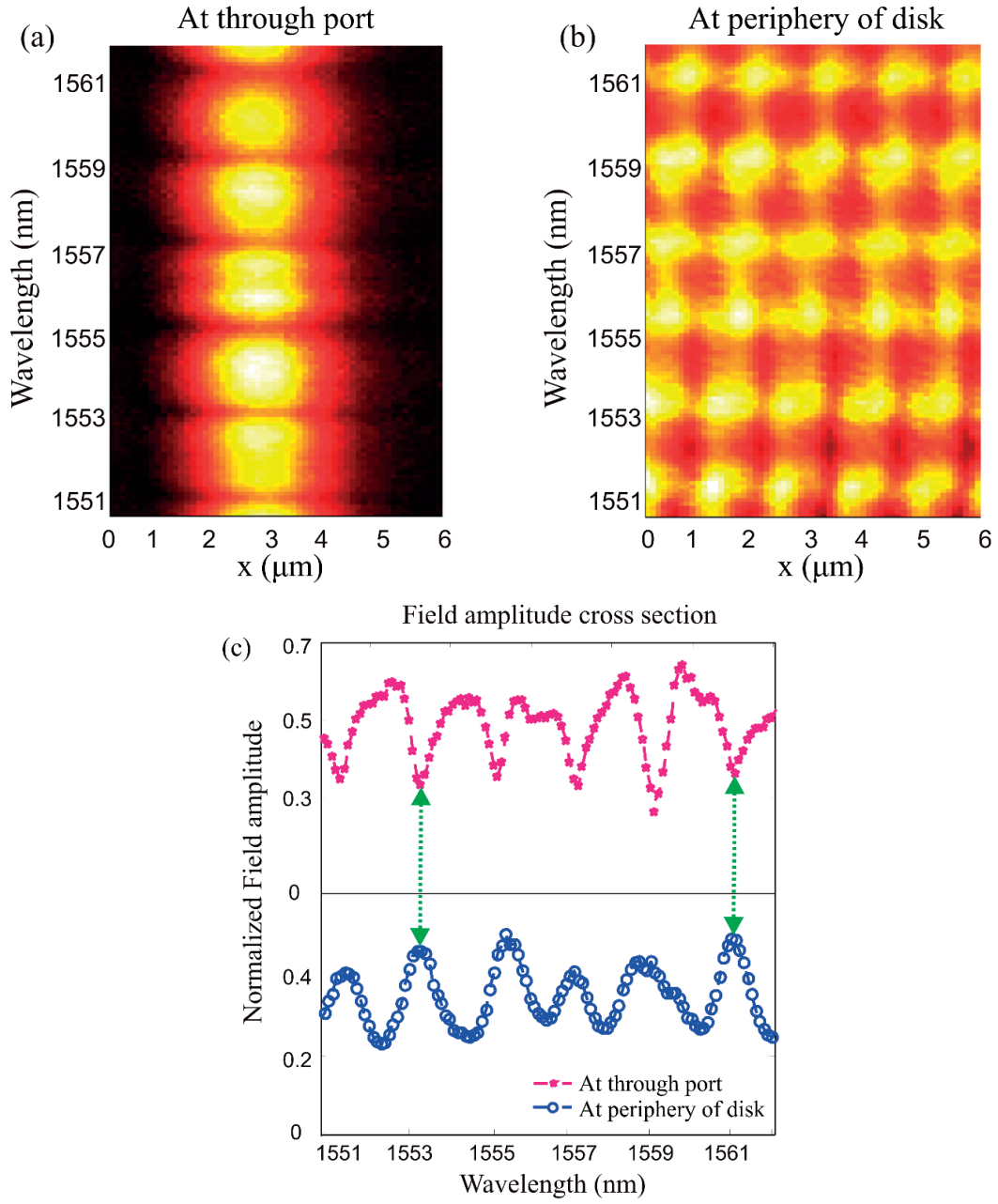


Fig.4.6. Near field image of wavelength scan taken by MH-SNOM. (a) At the through port. (b) At the periphery of the disk. The scanning is performed over 6  $\mu\text{m}$  across the waveguide in  $x$  direction. (c) Normalized transmission spectrum at the through port and the periphery of the disk as a function of the wavelength. The field amplitude is normalized with respect to the amplitude at the input port. The scanned areas are shown in Fig. 4.4 (dotted rectangular area).

The transmission spectrum of the through port and the trapped light inside the disk is obtained by plotting the cross section of the field amplitude at a particular position of the through port and periphery of the disk with respect to the wavelength, see Fig.4.6 (c). The amplitude is normalized with the field amplitude measured at the input port. The dips in the field amplitude cross section of through port and the peaks in the field amplitude cross section of periphery correspond to the On-resonance condition of the resonator and vice versa for Off-resonance condition. It can be seen that the dips in the field amplitude at the resonance wavelengths at the through port appears as the peaks at the same wavelengths at the periphery of the disk in Fig.4.6 (c).

After deducing On- and Off-resonance wavelengths from measured wavelength scan at output port, we map the field distribution over the complete waveguide and disk area in space (Fig. 4.7). For the fine positioning of SNOM probe, we use piezo stage which allows the maximum lateral displacement scan of 100x100  $\mu\text{m}$ . Therefore, the mapping of larger area, 250x250  $\mu\text{m}$ , is performed by series of several spatially overlapping sub maps stitched together with error margin. To image the different sub maps, the coarse positioning of the SNOM probe is performed using motorized stage. Figure 4.7 (a, c), for instance, is composed of nine sub-maps. The near field distribution over the complete disk at On/Off-resonance condition ( $\lambda_0 = 1555.4 \text{ nm}/ \lambda_0 = 1554.5 \text{ nm}$ ) is shown in Fig.4.7 (a, c). The pixel size is 1  $\mu\text{m}^2$ . One can observe the expected response of a disk resonator: a portion of the field is passing straight to the through port, indicating that it does not operate at critical coupling and this is the reason of low extinction ratio. However, an important part of the field is still coupled to the disk and coupled out to the drop port, and no light can be observed in the add port. In the background one can see a focusing effect of the part of light which is not coupled to the bus waveguide. This focusing comes from the refractive index change and the shape induced by the disk, as it has been demonstrated in [45]. We indicate the near field distribution around the coupling area between the waveguide and the disk for Off-resonance condition at  $\lambda_0 = 1554.5 \text{ nm}$  and compare it with the corresponding scan at On-resonance at  $\lambda_0 = 1555.4 \text{ nm}$ , see Figs.4.7 (b) and (d), respectively. One can see the propagation of the BSW in the through port at Off-resonance while it is coupled to the disk at On-resonance. However, at On-resonance BSW mode does not couple critically to the disk. The measured  $Q_0$  factor which is deduced from the transmission spectrum of through port is approximately:

$$Q_0 = \frac{\lambda_0}{\Delta\lambda} = 2 \times 10^3 \quad (4.10)$$

For a disk radius of 100  $\mu\text{m}$ , the calculated  $Q_0$  factor, when using the finite-difference time-domain (FDTD) method, is  $2 \times 10^4$ . In the experiments, scattering losses due to fabrication

imperfections and leakage losses because of prism coupling are the main reasons of the degradation of the  $Q_0$  factor by an order of magnitude. Nevertheless, the  $Q_0$  factor of our BSW resonator remains significantly higher than a classical plasmonic based resonator ( $Q_0 \sim 122$ ) [84] .

The measured FSR deduced from Fig.4.6 (c)

$$FSR = 2.0 \text{ nm} \quad (4.11)$$

The difference in the calculated and measured FSR arises from the BSW group velocity (group index).

The group index can be calculated from FSR at resonance wavelength 1555.4 nm as following:

$$n_g = \frac{\lambda_0^2}{FSR * 2\pi R} = 1.92 \quad (4.12)$$

The measured Finesse (from Fig.4.6 (c)) is 2.8 which means light is traveling in the disk for more than 2 full roundtrips.

$$Finesse = \frac{FSR}{\Delta\lambda} = 2.8 \quad (4.13)$$

The quality factor of the resonator can also be described as the number of field oscillations in the disk before the field amplitude drops down to the factor  $1/e$  [59], [89].

$$L_{BSW} = Q_0 * \frac{\lambda_0}{n_{eff2}} = 2468.9 \text{ } \mu\text{m} \quad (4.14)$$

$$Finesse = \frac{L_{BSW}}{2\pi R * n_g} = 2.0 \quad (4.15)$$

It can be seen that the value of Finesse calculated from different methods remains close to each other. Moreover, the propagation length calculation demonstrate that the calculated  $L_{BSW}$  from  $Q_0$  factor of the disk resonator shows a good agreement with the measured propagation length for 60 nm of device layer of  $\text{TiO}_2$ , which is approximately 2500  $\mu\text{m}$  (see chapter 3). It should be noted that  $L_{BSW}$  can be estimated more accurately from the intrinsic quality factor, however we measure total quality factor. As our resonator operates in under-critical coupling regime, it is not possible to deduce intrinsic quality factor from the measured quality factor. Nevertheless, the coupling out losses from the disk to waveguide are significantly low, due to large gap spacing, to consider total quality factor in the calculations of  $L_{BSW}$  estimation.

From the azimuthal mode distribution of the resonating wave along 6  $\mu\text{m}$  length of disk periphery (see Fig.4.6 (b)),  $n_{eff\_2}$  inside the disk can be calculated at resonance wavelength 1557 nm as following:

$$\text{Length of disk periphery} * n_{eff_2} = \text{azimuthal mode} * \lambda_0 \quad (4.16)$$

$$n_{eff_2} = 1.29 \quad (4.17)$$

The calculated value of  $n_{eff_2}$  is very close to the measured one, which is 1.26 for 60 nm device layer of  $\text{TiO}_2$  (see chapter 3).

The disk resonator with radius 40  $\mu\text{m}$  has been also studied in near-field. The transmission spectrum at the through port and field distribution over the complete waveguide and disk area in space, mapped by SNOM is shown in the appendix Fig.2 (a, b). However quality factor  $Q_0$  drops down to the order of hundreds in comparison to the calculated  $Q_0$  factor in simulations ( $\sim 2 \times 10^3$ ). This might be because of scattering losses due to fabrication imperfections and leakage losses into the multilayer because of prism coupling.

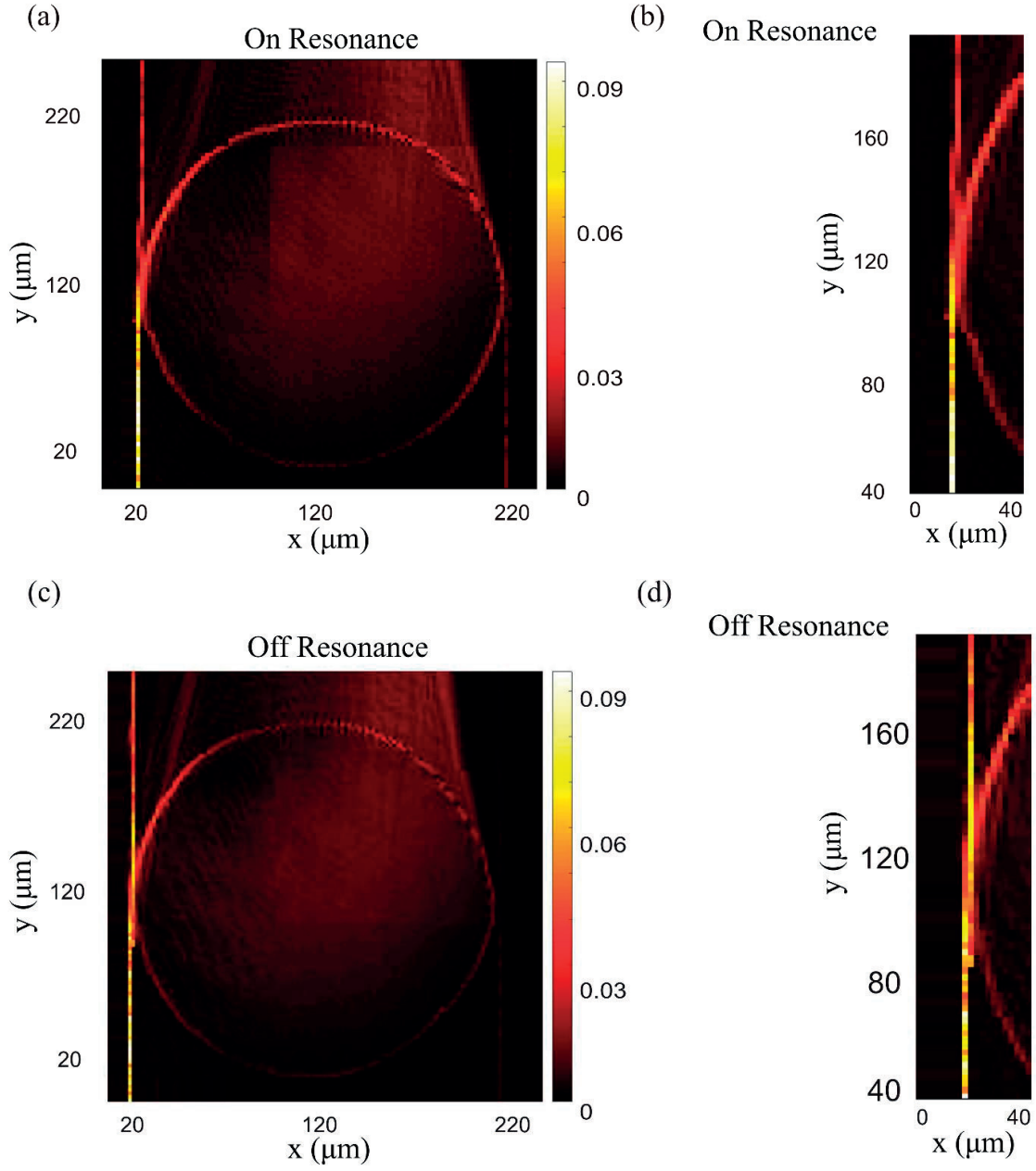


Fig.4.7. SNOM images of field amplitude distribution (a) over the complete structure of disk resonator at On-resonance at  $\lambda_0 = 1555.4 \text{ nm}$ , (b) Near the waveguide and disk coupling area at On-resonance, (c) over the complete structure of disk resonator at Off-resonance at  $\lambda_0 = 1554.5 \text{ nm}$ , (d) Near the waveguide and disk coupling area at Off-resonance.

## 4.6 Conclusion

For the first time a 2D disk resonator is demonstrated experimentally on BSW dielectric multilayer platform. A thin layer ( $\sim\lambda/25$ ) of  $\text{TiO}_2$  is used as a high refractive index device layer on the top of a dielectric periodic stack to form the 2D disk resonator. Considering the evanescent character of BSW, to observe the near field interaction of the BSW with the resonator, we map the field amplitude distribution images with a MH-SNOM. The results show that higher quality factor BSW resonators respect to plasmonic resonators are achievable, principally because of the low loss dielectric multilayer platform in comparison to SPP based devices. For a disk radius of  $100\text{ }\mu\text{m}$ , the measured  $Q_0$  factor is  $2\times 10^3$ . The calculated  $Q_0$  using CST simulations (FDTD method) is approximately  $2\times 10^4$ . The scattering losses, fabrication imperfections and leakage are the dominant reasons reason of degradation of experimentally obtained  $Q_0$  factor. The quality factor can be further improved using grating coupler. With the present design, we compromise the footprint of disk resonator in terms of high  $Q_0$  factors. The resonators with more compact size can be realized by using higher refractive index materials as a device layer, for example Silicon. Further study is needed to improve the design to achieve higher extinction ratios and more compact design.

The main results of this chapter are published in Paper [1] of journal publications in the list of appendices at the end of thesis.

## 4.7 Appendix

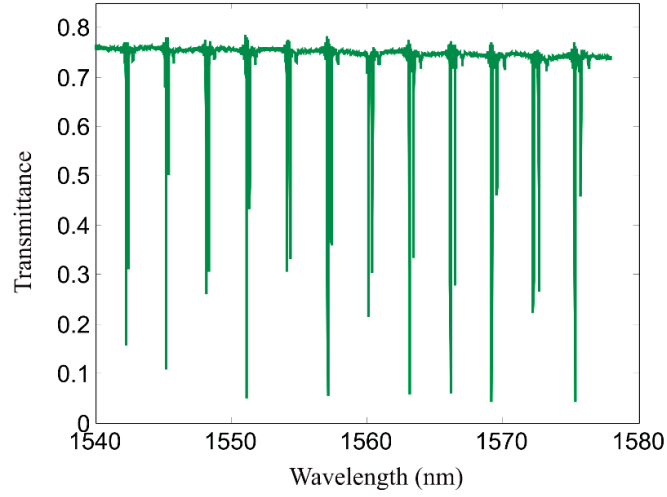


Fig.1. The simulated (FDTD method CST studio) transmission spectrum of a disk radius  $R = 100 \mu\text{m}$ , a bus waveguide width  $w = 2 \mu\text{m}$ , and a gap  $g = 1.0 \mu\text{m}$ . The drop in the extinction ratio can be observed.

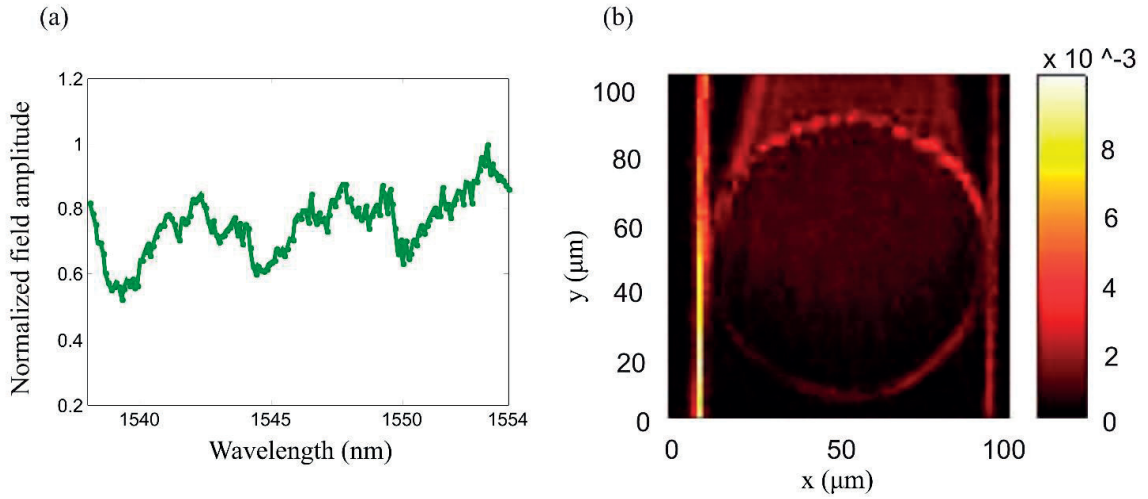


Fig.2. The near-field measurement of disk resonator of radius  $40 \mu\text{m}$ , obtained by SNOM (a). The transmission spectrum at the through port for the wavelength range of 1540 nm to 1580 nm. (b) The field distribution over the complete waveguide and disk area in space at wavelength 1550 nm.





# CHAPTER 5

## Bloch Surface Waves based 2D Bessel-like beam generator

In this chapter, we study the generation of 2D Bessel-like quasi-non-diffracting beams. To produce such a beam, a planar isosceles triangle is fabricated into a thin layer ( $\sim \lambda/25$ ) of a titanium dioxide layer deposited on the top of the multilayer platform. The optical properties of the 2D Bessel-like beams are investigated in the near-field with the aid of multi-heterodyne scanning near field optical microscopy. For the better understanding and control of the optical properties, we study different designs of 2D triangles. Thanks to the low loss characteristics of BSWs, the presented beams can be used as a low loss (coupling) long optical interconnects between on-chip components and optical tweezers.

The diffraction is fundamental phenomenon in optics. This affects all classical wave fields such as sound waves, electromagnetic, and even matter waves. Diffraction induces the expansion of the transverse dimension of a propagating wave when wave encounters an obstacle. The characteristic distance beyond which diffractive spreading becomes increasingly noticeable is the Rayleigh range  $r^2/\lambda$ , where  $r$  is a radius of finite area in which field was initially confined before starting propagating.

The beams whose transverse field profile is invariant along the propagation direction are called diffraction-free beams. These beams are characterized with well-defined narrow beam widths, in the order of a wavelength. The Beam remain tight confined while propagating without being subject to diffractive spreading. The beams also exhibit an ability to reconstruct itself if an obstacle is placed along the propagation axis. Because it requires infinite energy and an infinite spatial extent, ideally such a beam cannot be realized experimentally. However, quasi-diffraction-free beams can be generated in a spatially limited region. In 1987, Durnin et al. have studied for

the first time diffraction-free mode solutions of Helmholtz equation and realized them experimentally [90]. These non-spreading mode solutions are called Bessel beams [91], [92]. In his very first experiment, Durnin has used a circular slit (diameter  $d$  and width  $\Delta d$ ) placed in the focal plane of a lens (focal length  $f$  and radius  $R$ ) to generate diffraction-free Bessel beams, as shown Fig.5.1. Each point of the slit acts as a point source. The lens transforms these point sources into plane waves. The set of plane waves formed this way superimpose over each other and generate a quasi-diffraction-free beam with maximum propagation distance  $Z_{max\_prop}$  (see  $Z_{max}$  Fig.5.1). The transverse profile of these beams is the zero-order Bessel function of the first kind.

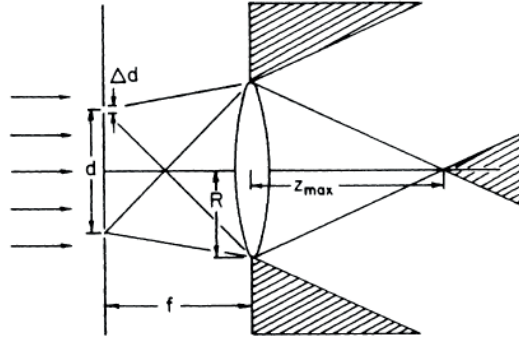


Fig.5.1. The experimental set-up of Bessel beam generation in free space using circular slit and focusing lens [90].

The above discussed beams are the solutions to the free space three-dimensional (3D) Helmholtz equation. The 2D solutions of diffraction-free beams are not straightforward. However, the numerical studies show that the 2D quasi-diffraction-free beams that resembles the profile of Bessel function can be generated by tailoring the diffraction [13]. We address these beams as a 2D Bessel-like beam.

In on chip interconnects coupling spreading of beams in transverse direction is a source of coupling losses. The 2D Bessel-like beam with a long and tight focus spot can be used efficiently of this purpose. These beams can also find applications as an optical tweezers and in transportation and patterning of nano particles [93], [94].

## 5.1 Design concept and fabrication

In 3D, the most practical way to generate nondiffracting Bessel beams is an axicon lens, such as a conical-shaped prism [95]. For 2D axicon design, we take an advantage of long distance propagating BSWs. We utilize a simple isosceles triangle as a 2D form of a 3D axicon lens which allows the generation of Bessel-like beams using simple refraction phenomenon. In theory, the length of the overlapping diamond region, which is produced due to the interference of the two refracted beams from the sides of axicon, defines the maximum propagation distance ( $Z_{max\_prop}$ ).

The 2D axicon is fabricated into a 60 nm thick device layer of  $\text{TiO}_2$  on the top of multilayer platform. The SEM image of fabricated triangle with 50  $\mu\text{m}$  base and 25  $\mu\text{m}$  height is shown in Fig.5.2. The structure is patterned with e-beam lithography (EBL). The process and steps of e-beam patterning have been explained in the fabrication section of chapter 3. The different designs where the height of the axicon varied from 20  $\mu\text{m}$  to 30  $\mu\text{m}$  with a step of 5  $\mu\text{m}$  are fabricated. The purpose of studying different designs is to compare the performance of an axicon in terms of  $l/e$  propagation length and full width at half maximum (FWHM) of the transverse field profile.

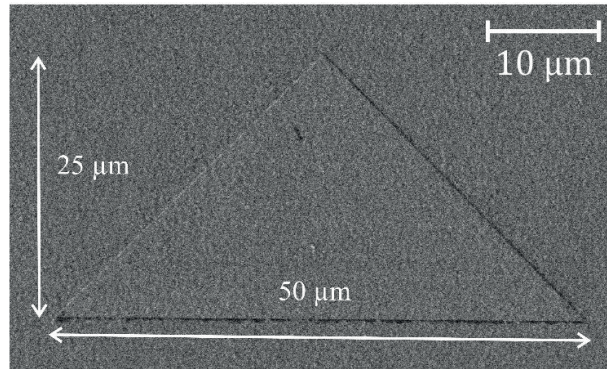


Fig.5.2. SEM image of a 2D axicon (isosceles triangle) with base = 50  $\mu\text{m}$  and height = 25  $\mu\text{m}$ , fabricated into 60 nm thick  $\text{TiO}_2$  layer.

We simulate the 2D axicon (isosceles triangle) with base = 50  $\mu\text{m}$  and height = 25  $\mu\text{m}$ , which leads to the axicon base angle ( $\theta_b$ ) equal to  $45^\circ$ . The simulation are performed using CST microwave studio based on FDTD method. The 2D system has been simulated with the effective index approach ( $n_{eff\_2}=1.26$  and  $n_{eff\_1}=1.14$ ). In simulations, the 2D triangle is illuminated with plane wave. After refraction from the sides of the triangle, the wave fronts interfere and generate a diamond shape long focus region. Figure 5.3 (a) shows the field distribution of a Bessel-like beam with long confined focus. The  $l/e$  propagation distance ( $L_{Bessel}$ ) is approximately 140  $\mu\text{m}$ , as shown

in Fig.5.3 (a). The transverse field amplitude profile at the peak amplitude position ( $z = 93 \mu\text{m}$ ) shows the full width at half maximum (FWHM) of  $2.6 \mu\text{m}$  (see in Fig.5.3 (b)).

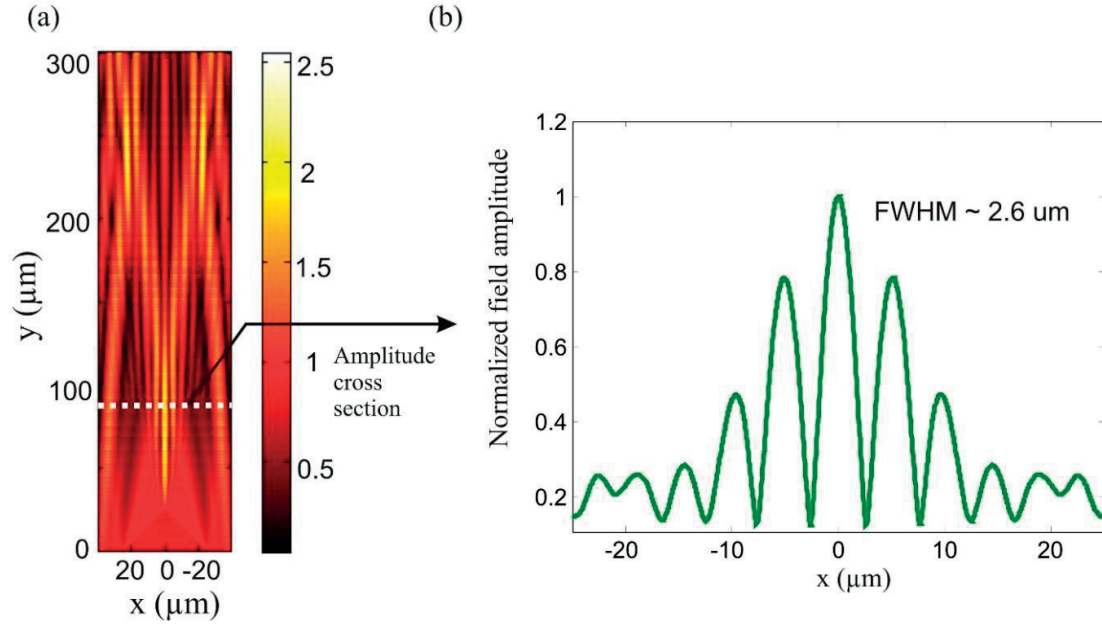


Fig.5.3 (a). The simulated field amplitude distribution of Bessel-like beam profile of the 2D axicon of  $50 \times 25 \mu\text{m}$  (base  $\times$  height) dimension. (b) The cross section of lateral profile of the axicon plotted as a field amplitude distribution in  $x$  direction.

## 5.2 Near-field measurement results and discussion

The incident beam illuminates the multilayers through the total internal reflection configuration (see Fig.5.4) at an oblique incident angle ( $58.62^\circ$ ) which is higher than the critical angle to attain the BSW propagation vector for  $60 \text{ nm}$  of  $\text{TiO}_2$  layer, at wavelength  $\lambda = 1548 \text{ nm}$ . To attain a plane wave approximation we work with the out of focus condition where the beam with a larger diameter (approximately  $100 \mu\text{m}$ ) is illuminating the 2D axicon with a base of  $50 \mu\text{m}$  (see Fig.5.5).

The multilayer structure is illuminated with a TE polarized light. The coupled BSW illuminates the base of the 2D triangle at normal incidence. After refraction from the two sides of triangle, the two constituent beams interfere constructively in  $y$ -direction and giving rise to a standing wave profile, modulated with a Gaussian envelope, in  $x$ -direction (Fig.5.6 (a)). Hence, the

interference of the two constituent beams produce a long and confined focus spot which has a 2D Bessel-like beam profile in transverse direction ( $x$ -direction). We investigate three different dimensions of 2D axicon in near-field for example, base  $\times$  height =  $50 \times 20 \mu\text{m}$ ,  $50 \times 25 \mu\text{m}$ ,  $50 \times 30 \mu\text{m}$ .

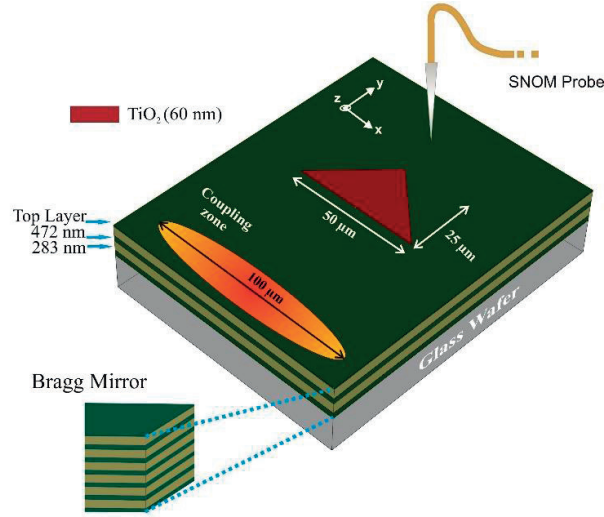


Fig.5.4. Schematic of the dielectric multilayers platform with 2D isosceles triangle fabricated into 60 nm-thick  $\text{TiO}_2$  layer. The SNOM probe, in collection mode, is used to observe the interaction of the BSW with the grating in near-field on the top.

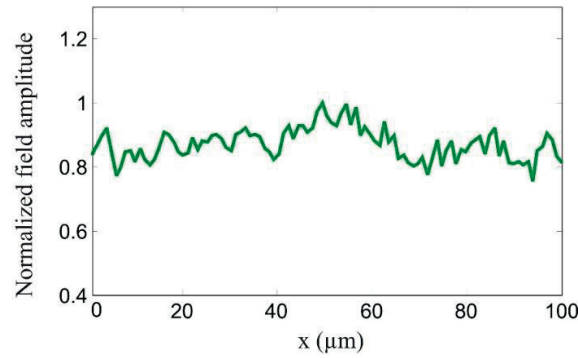


Fig.5.5. The transverse field profile of the enlarged (out of focus) illumination spot measured by MH-SNOM. The amplitude plot is normalized to its maximum.

The near-field amplitude distributions over the Bessel-like beam profile produced by the 2D axicon is measured using MH-SNOM. Figure 5.6 (a) demonstrates the near-field amplitude distributions of the beam profile with dimension of axicon: base of  $50 \mu\text{m}$  and height  $20 \mu\text{m}$ . Figure

5.6 (b) and (c) shows FWHM and the  $1/e$  propagation distance ( $L_{Bessel}$ ) obtained from the cross section of the  $x$  and  $y$  direction field profiles, respectively. The measured propagation distance  $L_{Bessel}$  and FWHM at the maximum amplitude for the axicon of  $50 \times 20 \mu\text{m}$  dimension are approximately  $194 \mu\text{m}$  and  $3.41 \mu\text{m}$ , respectively.

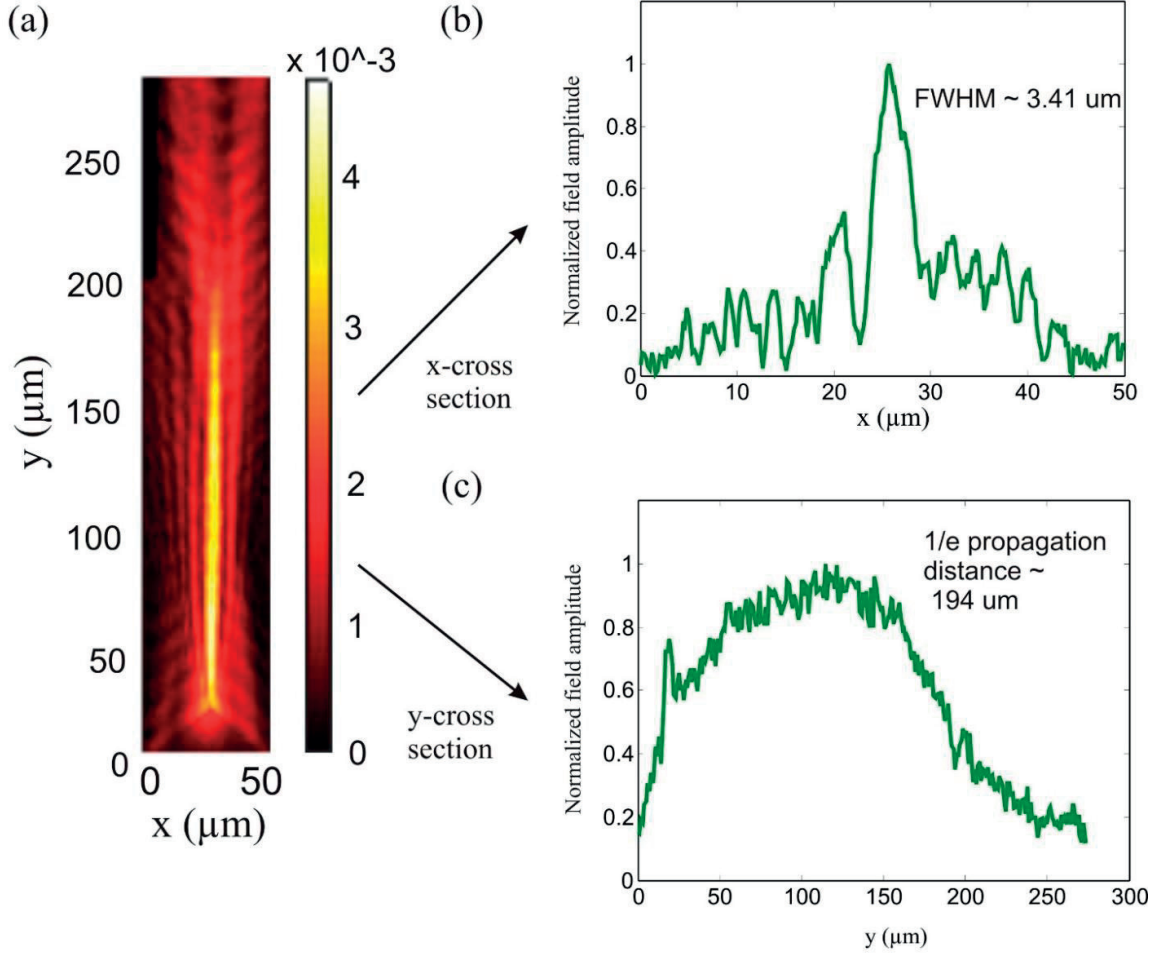


Fig.5.6 (a). The field amplitude distribution of the Bessel-like beam profile of the 2D axicon of  $50 \times 20 \mu\text{m}$  (base  $\times$  height) dimension. (b) The cross section of transverse profiles of the beam plotted as a field amplitude distribution at in  $x$  direction. (c) The cross section of the field amplitude distribution in  $y$  direction.

Similarly, we measure the near-field amplitude distributions of the Bessel-like beam profile produced by the 2D axicon of  $50 \mu\text{m}$  base and  $25 \mu\text{m}$  height, as shown in Fig.5.7 (a). The  $FWHM$  and  $1/e$  propagation distance ( $L_{Bessel}$ ) obtained from the cross section of the  $x$  and  $y$  direction field profiles, respectively, are shown in Fig.5.7 (b) and (c). The measured propagation distance  $L_{Bessel}$



and FWHM at the maximum amplitude for an axicon of  $50 \times 25 \mu\text{m}$  dimension are approximately  $133 \mu\text{m}$  and  $2.81 \mu\text{m}$ , respectively. The experimental results are in agreement to the simulation results. The plane wave approximation in experiments and approximations in effective refractive index are the important factors to be considered as the reason of differences between simulation and experimental results.

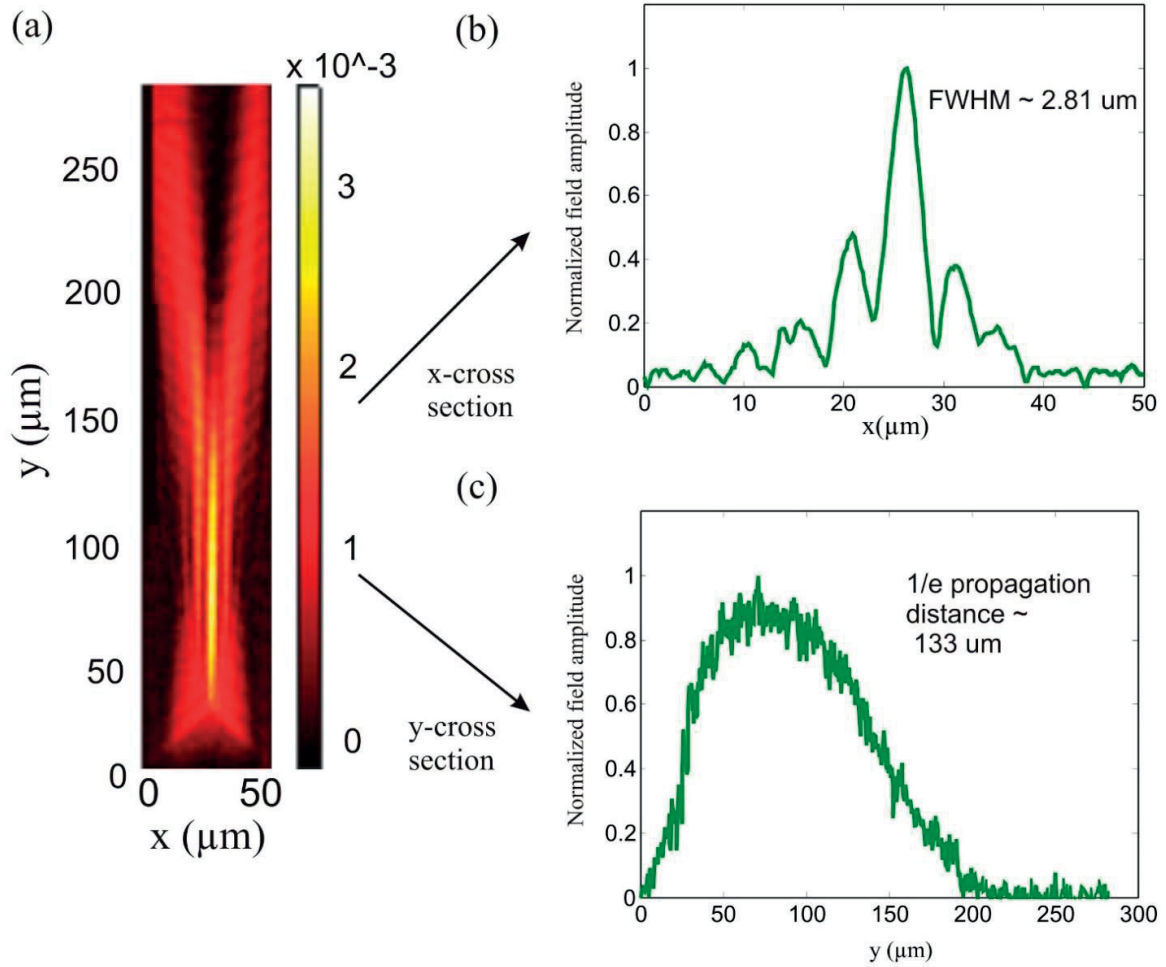


Fig.5.7 (a). The field amplitude distribution of Bessel-like beam profile of the 2D axicon of  $50 \times 25 \mu\text{m}$  (base  $\times$  height) dimension. (b) The cross section of transverse profiles of the beam plotted as a field amplitude distribution at in  $x$  direction. (c) The cross section of the field amplitude distribution in  $y$  direction.

Further, we also study the field profile produced by a 2D axicon of  $50 \mu\text{m}$  base and  $30 \mu\text{m}$  height in the near-field as shown in Fig.5.8 (a). The FWHM and  $1/e$  propagation distance ( $L_{\text{Bessel}}$ ) obtained from the cross section of the  $x$  and  $y$  direction field profiles respectively are shown in Fig.



5.8 (b) and (c). The measured propagation distance  $L_{Bessel}$  and FWHM at the maximum amplitude for axicon of  $50 \times 30 \mu\text{m}$  dimension are approximately  $69 \mu\text{m}$  and  $2.10 \mu\text{m}$ , respectively.

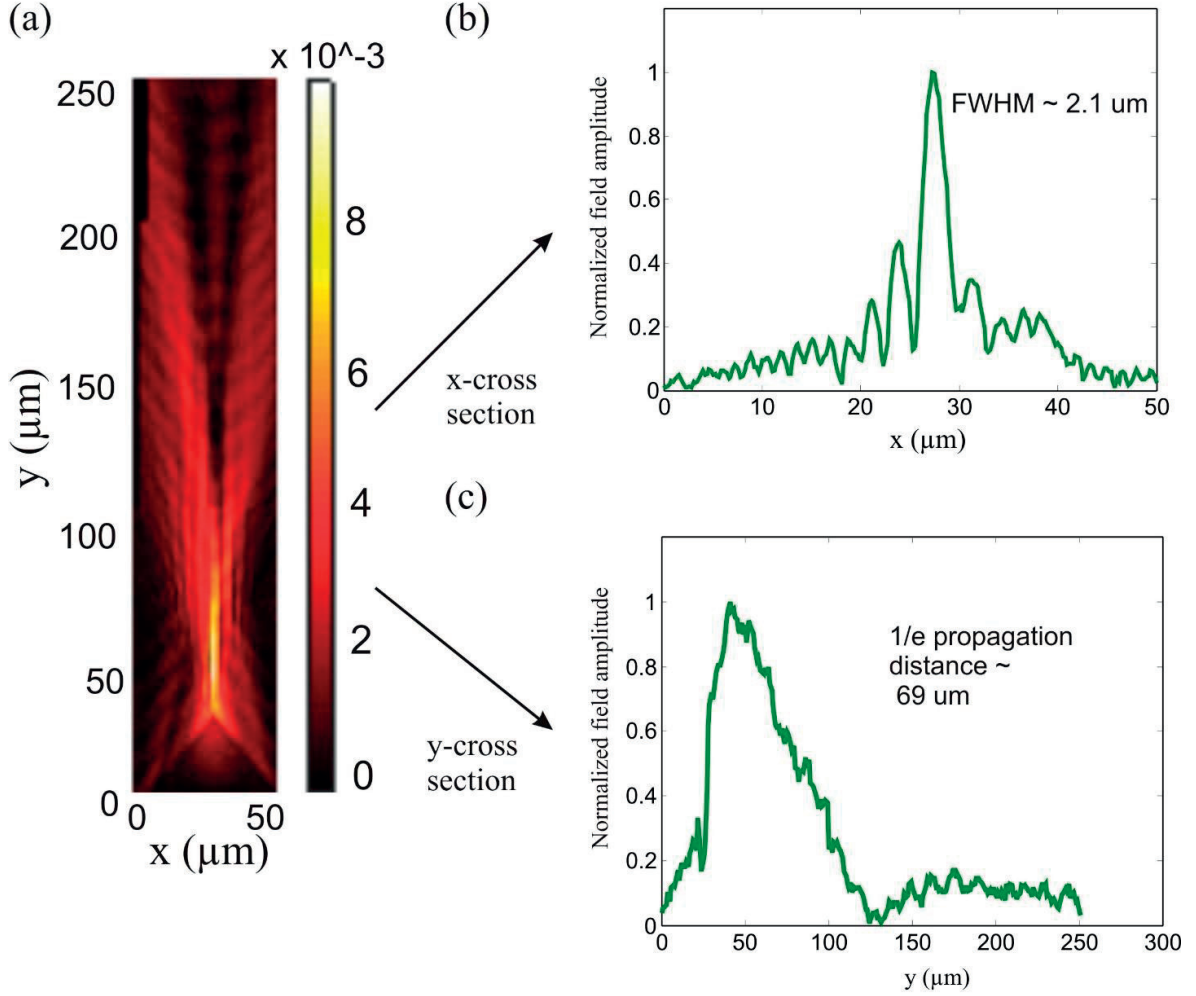


Fig.5.8 (a). The field amplitude distribution of the Bessel-like beam profile of the 2D axicon of  $50 \times 30 \mu\text{m}$  (base  $\times$  height) dimension. (b) The cross section of transverse profiles of the beam plotted as a field amplitude distribution in  $x$  direction. (c) The cross section of the field amplitude distribution in  $y$  direction.

Depending on the dimension of the axicon the propagation distance and FWHM of the focused spot vary. It should be noted that as we are increasing the height of the axicon the propagation distance decreases however confinement of the focus spot becomes tighter (as width of the focus spot decreases). We demonstrate that based on desired applications, long focus/tighter

confinement, the design parameters of the axicon can be chosen appropriately. The experimental results of  $1/e$  propagation distance ( $L_{Bessel}$ ) and FWHM are summarized in table 1.

Base ( $\mu\text{m}$ )	Height ( $\mu\text{m}$ )	$1/e$ Propagation distance, $L_{Bessel}$ ( $\mu\text{m}$ )	FWHM beam width ( $\mu\text{m}$ )
50	20	194	3.41
50	25	133	2.81
50	30	69	2.10

Table 1. Summary of measured propagation distance and FWHM of the focus spot for 50  $\mu\text{m}$  base and different heights of 20  $\mu\text{m}$ , 25  $\mu\text{m}$  and 30  $\mu\text{m}$ .

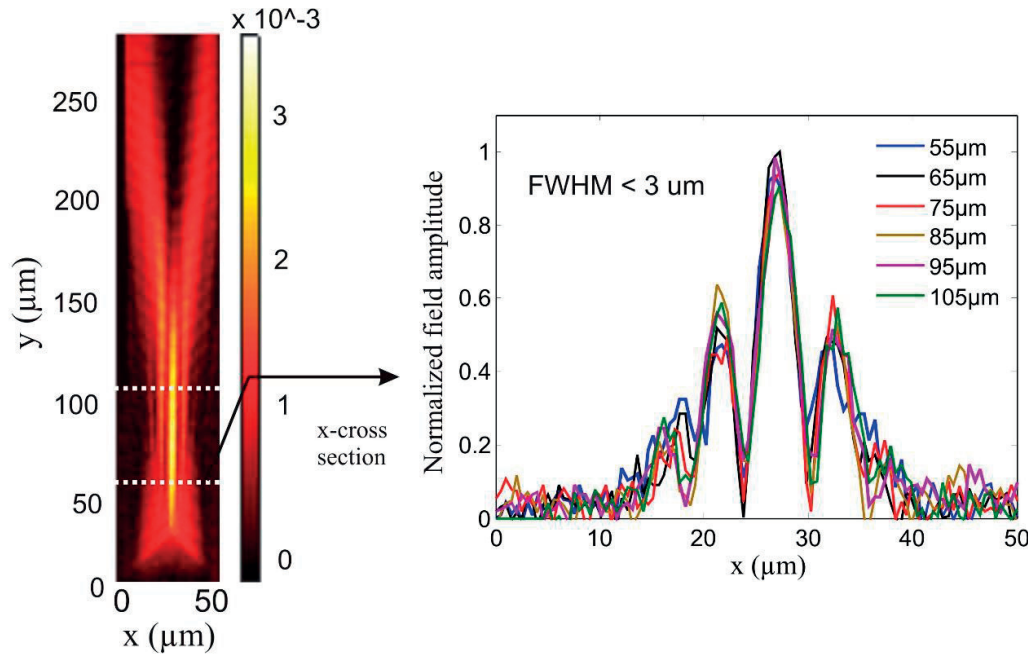


Fig.5.9. The cross section of transverse amplitude distribution ( $x$  direction) of the axicon (50  $\times$  25  $\mu\text{m}$ ) at different propagation distances in  $y$  direction.

To obtain the non-diffracted length of the long focused beam precisely, we extract the transverse field amplitude ( $x$  direction) profiles to compare the beam width at different distances along the propagation direction ( $y$  direction). As an example we consider an axicon of  $50\text{ }\mu\text{m}$  base and  $25\text{ }\mu\text{m}$  height, as shown in Fig.5.9. It is evident that from  $z = 55\text{ }\mu\text{m}$  to  $105\text{ }\mu\text{m}$ , the beam propagates without significant divergence (FWHM  $< 3\text{ }\mu\text{m}$ ). Thanks to low loss characteristics of BSWs, we obtain significantly longer maximum propagation distance  $Z_{\text{max\_prop}}$  than the SPPs based 2D Cosine-Gauss beam [12].

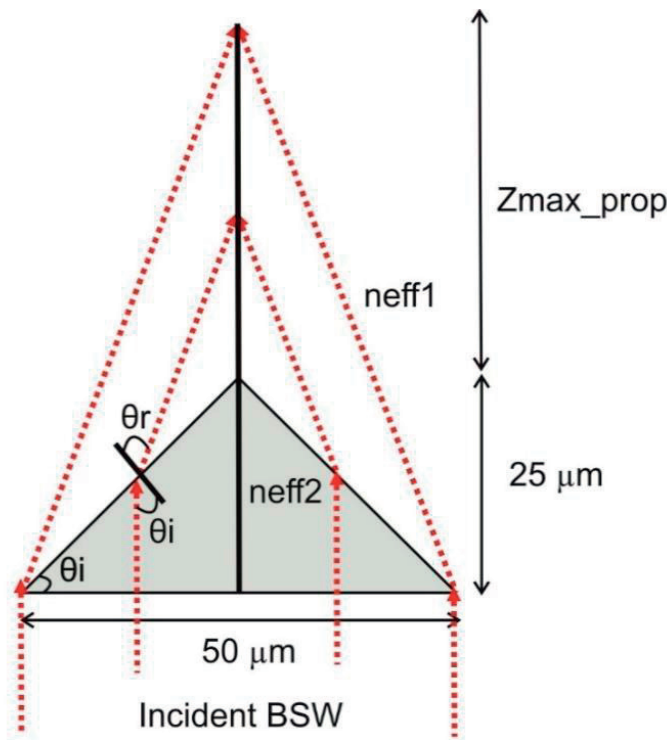


Fig.5.10. Schematic of 2D axicon illuminated with BSW. The interference of the two refracted beams from the sides of the axicon produces the diamond shaped overlapping area,  $Z_{\text{max\_prop}}$ .

The length of diamond shaped overlapping area,  $Z_{\text{max\_prop}}$ , which is produced due to the interference of the two refracted beams from the sides of the axicon can be deduced from Fig.5.7 (a). It is around  $140\text{ }\mu\text{m}$ . It can be also calculated theoretically (referring to Fig.5.10). For example, using Snell's law the angle of refraction  $\theta_r$  can be calculated from angle of incidence  $\theta_i$ .

$$n_{eff2} * \sin\theta_i = n_{eff2} * \sin\theta_r \quad (5.1)$$

$$\frac{25 + Z_{prop}^{max}}{25} = \tan(135 - \theta_r) \quad (5.2)$$

$$Z_{prop}^{max} = 198.2 \text{ } \mu\text{m} \quad (5.3)$$

Where,  $n_{eff2}$  (1.26) and  $n_{eff1}$  (1.14) are effective refractive indices in BML with device layer and BML.

The theoretically calculated overlapping distance  $Z_{max\_prop}$  is approximately 198  $\mu\text{m}$  for the axicon of 50 x 25  $\mu\text{m}$  dimension. However, the measured overlapping area is around approximately 140  $\mu\text{m}$ , (see Fig.5.7 (a)). The difference could arise due to plan wave approximation which leads the reduction in the length of effective base length (effectively illuminated base) of axicon. Considering this fact, if we take half of the effective base length equal to 20  $\mu\text{m}$  (see Fig.5.7 (a)), the calculated overlapping distance  $Z_{max\_prop}$  is 153.6  $\mu\text{m}$ .

As explained above the dimension of the axicon manipulates the optical properties of the long focus produced due to interference of two refracting waves. Until now, we kept the base of the axicon 50  $\mu\text{m}$ . Further, we study the axicon with 10  $\mu\text{m}$  base and 15  $\mu\text{m}$  height. Such an aspect ratio of the base and height of the triangle leads to the total internal refraction at the sides of the axicon ( $\theta_c = \sin^{-1}(\frac{n_{eff1}}{n_{eff2}} = \frac{1.14}{1.26} = 64.79 \text{deg.})$ ). Therefore, the waves interfere constructively in TIR condition [ $\theta_i(71.56 \text{deg}) > \theta_c(64.79 \text{deg.})$ ] and confine to a subwavelength focused spot as shown in Fig.5.11 (a). The measured FWHM of the focused spot from the amplitude cross of the near-field image in  $x$  direction is approximately 0.90  $\mu\text{m}$  (Fig.5.11 (b)). Figure 5.11 (c) and (d) shows the simulated field pattern of the focused spot and its corresponding amplitude cross section respectively. The calculated FWHM of the focused spot is 0.82 which is very close to what is obtained experimentally.

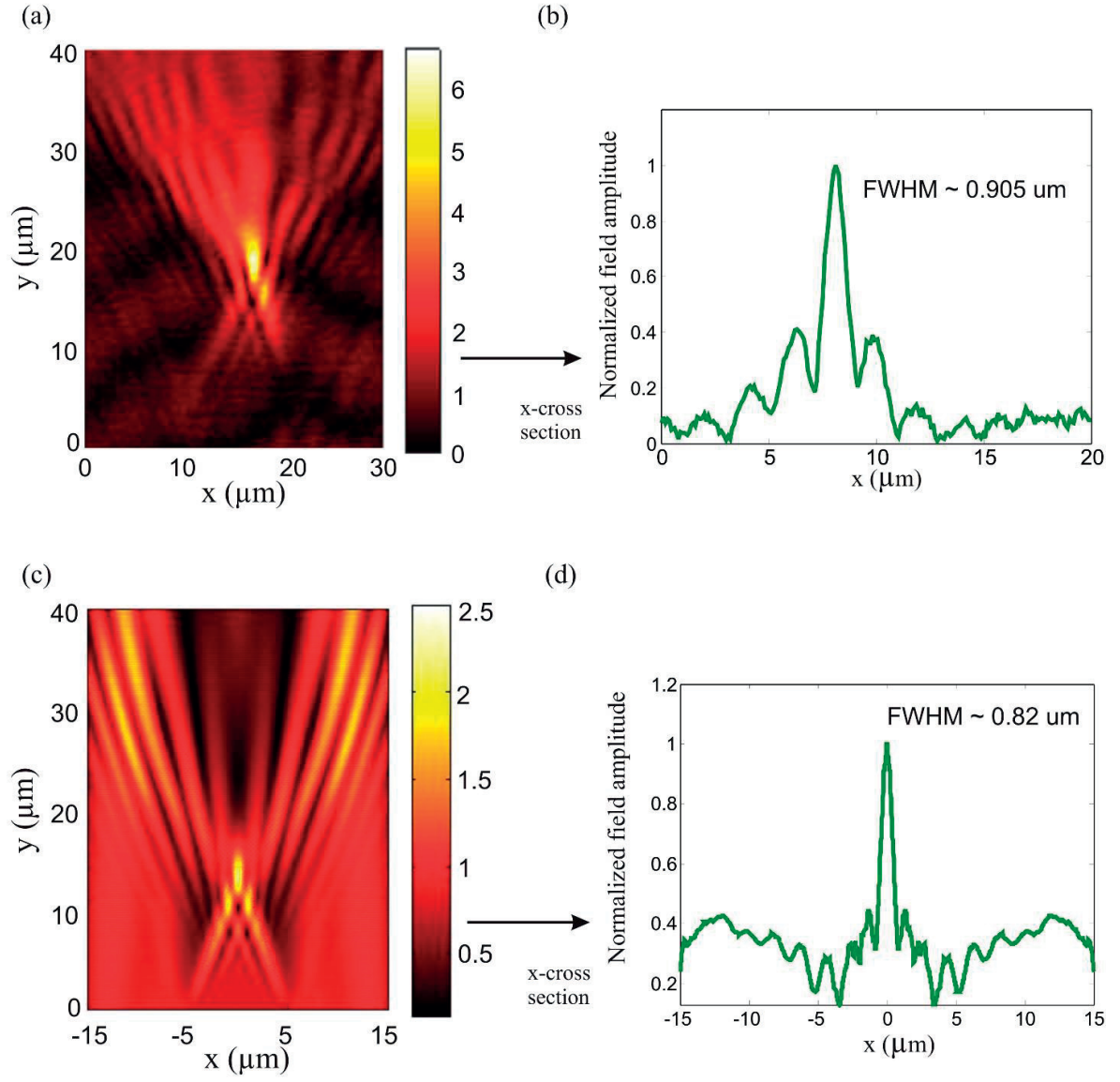


Fig.5.11 (a). The field amplitude distribution over an axicon of  $10 \times 15 \mu\text{m}$  (base  $\times$  height) dimension. (b) The cross section of the transverse profiles of the focused spot plotted as a field amplitude distribution in  $x$  direction. (c) and (d) The field amplitude distribution calculated with CST simulations and corresponding cross section.

### 5.3 Conclusion

We demonstrate the generation of Bessel-like beams using a 2D axicon on a Bloch surface wave platform. Such beams are generated using a 2D axicon fabricated into 60 nm thick layer of  $\text{TiO}_2$  on the top of multilayer platform. The different designs of the 2D axicon with the variation of height of the axicon are investigated. The purpose of studying different designs is to compare the optical performance of 2D Bessel-like beams, in particular propagation distance and full width half maximum. The optical parameter of the 2D Bessel-like beams are also calculated using CST simulations (FDTD method). The results obtained from experiments are in a good agreement with the simulation results. The measured near-field amplitude distribution shows the long focus spot propagating without significant spreading for a considerable propagation distance. Further, we tabulate the propagation properties of a 2D Bessel-like beam for different designs of the axicon. The study provides deep understanding of the optical properties of 2D Bessel-like beams which can be controlled by the design parameters of the 2D axicon with the aim of the desired applications (long focus/tighter confinement) behind. Thanks to low loss characteristics of BSWs, we obtain significantly longer propagating focus spots than the SPPs based 2D Cosine-Gauss beams. The 2D Bessel-like beams find applications as a low loss (coupling) optical interconnects between on-chip components, optical tweezers and in transportation and patterning of nano particles.

The main results of this chapter are published in conference proceedings [2, 3] in the list of appendices at the end of thesis.



# CHAPTER 6

## Bloch Surface Waves based 2D Bragg Mirror

With the aim of development of BSW based 2D integrated optical systems, several 2D optical components used to manipulate the BSWs propagation have already been studied theoretically and experimentally. They include, ridge waveguides, lenses, prisms, diffraction gratings, waveguide couplers, curved waveguides and disk resonators on top of the multilayer platform. These studies have demonstrated that BSWs can be focused, diffracted, resonated, and total internally reflected obeying the 2D propagation laws. Furthermore, the characterization of 2D disk resonators and 2D Bessel-like beams on the BSW platform have been presented in chapter 4 and 5.

In this chapter, we experimentally demonstrate the optical properties of gratings engraved in a single mode waveguide fabricated on top of a dielectric multilayer platform. The structure can be approached as a Bragg mirror for Bloch surface wave based two-dimensional integrated systems. The gratings are fabricated into a few tens of nanometer thin ( $\sim\lambda/25$ ) titanium dioxide layer deposited on the top of the multilayer platform. The optical properties of the gratings are characterized in the near-field with the aid of multi-heterodyne scanning near field optical microscopy. We investigate the surface wave's interference pattern, produced by incident and reflected light in front of the gratings. The presented gratings behave as an efficient Bragg mirror at telecommunication wavelengths.

We study the interaction of BSWs propagating through a single mode 2  $\mu\text{m}$ -wide waveguide along which a grating is patterned. We demonstrate that the presented gratings can be used as a BSW Bragg mirror in a specific wavelength range. This work provides the understanding of the fundamental principles of BSW reflection from a dielectric mirror and thus enables a step ahead towards the development of BSW based 2D integrated optical systems. To the best of our knowledge this is the first experimental realization and characterization of waveguide grating as a Bragg mirror based on Bloch Surface Waves. The study of Bragg mirror is an initial step to realize BSWs based Fabry-Perot resonators.



## 6.1 Design concept and fabrication

The grating presented in this study have been structured into a 2  $\mu\text{m}$ -wide waveguide, which is patterned in the 60 nm-thick layer of  $\text{TiO}_2$  ( $\sim\lambda/25$ ) on top of the multilayer platform, as shown in Fig.6.1. The measured value of effective refractive index of the  $\text{TiO}_2$  waveguide ( $n_{eff2}$ ) and BML ( $n_{eff1}$ ) are approximately 1.20 and 1.14, respectively. According to the Bragg condition  $d_1 n_{eff1} + d_2 n_{eff2} = \lambda_B/2$ , where  $\lambda_B$  is the Bragg wavelength, and by choosing the periodicity of  $d_1 + d_2 = 664$  nm with a fill factor of 50% (the slit width and the gap between the slits are set to 332 nm), we can obtain a Bragg reflector operating around the telecom wavelength of 1.55  $\mu\text{m}$ .

Because of low losses of the constituent dielectric materials, BSW can propagate longer and penetrate deep into the gratings. This provides the advantage of possibility of improving the reflectivity of grating by increasing the number of periods of the gratings which is not the case in Surface plasmonic gratings. The presented gratings are composed of 80 periods.

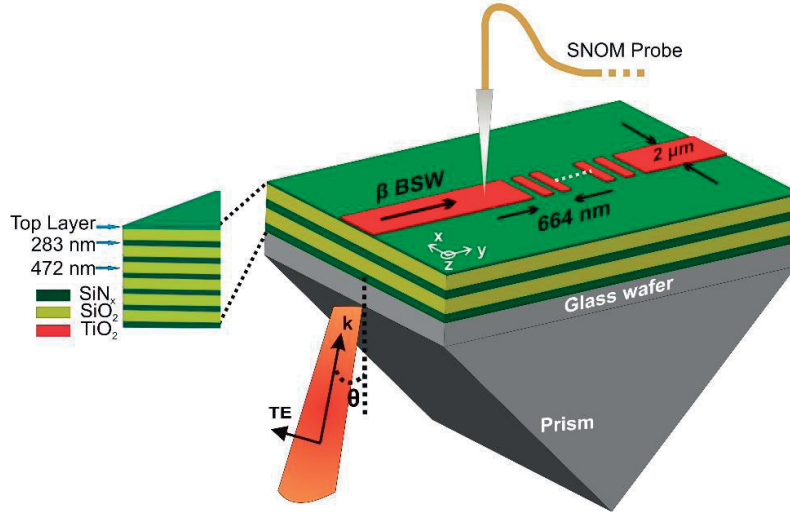


Fig.6.1. Schematic of the setup of total internal reflection configuration for BSW coupling with dielectric multilayers deposited on a glass wafer. The 2D grating patterned in the waveguide is fabricated on the top of multilayers into a 60 nm-thick  $\text{TiO}_2$  layer. The SNOM probe, in collection mode, is used to observe the interaction of the BSW with the grating in near-field.

In the similar manner as discussed in previous chapters, a total internal reflection (TIR) configuration is used to couple BSWs, and MH-SNOM for the characterization of the spatial light distribution of the 2D waveguide grating.

The 2D waveguide gratings are fabricate into 60 nm thick device layer of TiO<sub>2</sub> on the top of multilayer platform. The structure is patterned with e-beam lithography. The process and steps of e-beam patterning have been explained in fabrication section of chapter 3. The SEM image of fabricated waveguide grating is shown in Fig.6.2.

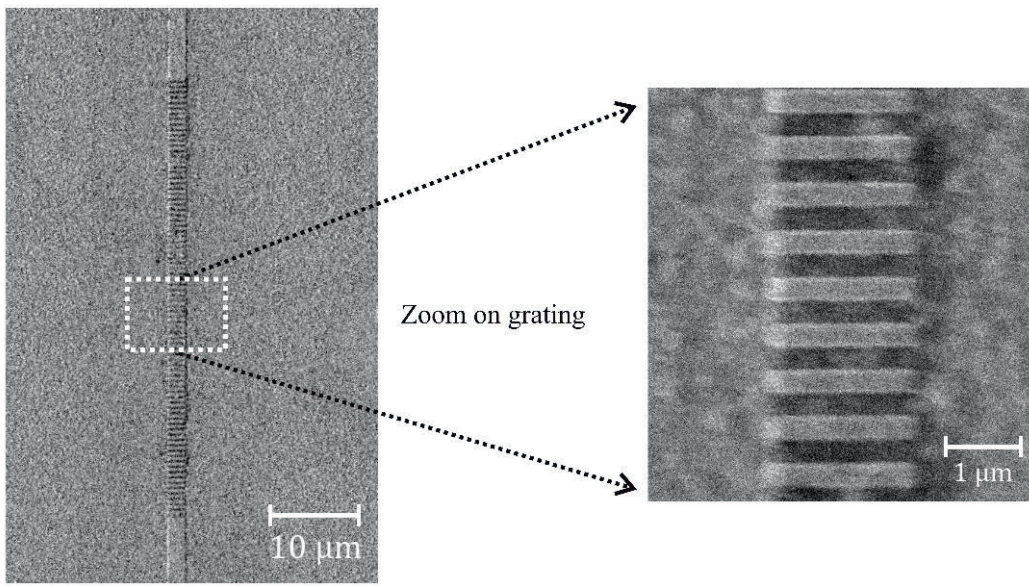


Fig.6.2. SEM image of waveguide grating engraved into 2 μm wide TiO<sub>2</sub> waveguide, with a zoom on grating area.

## 6.2 Near-field characterization

At a particular incident angle (larger than the critical angle of 58.26°), the BSW is excited inside the TiO<sub>2</sub> waveguide. We keep the illumination spot approximately 50 μm away from the beginning of the grating. Light propagates in the waveguide and reflects back as it interacts with the gratings. We observe that the field amplitude appears as a standing wave pattern across the waveguide. The standing wave is generated because of the interference of the incident and the back reflected light. The periodicity of the fringes is approximately  $\lambda_{Beff}/2$ , with  $\lambda_{Beff} = \lambda_B/n_{eff2}$ .

In order to investigate the wavelength response of the grating, we perform simulations using CST microwave studio based on the finite difference time domain (FDTD) method. Figure 6.3 (a) shows the reflection spectrum of the waveguide grating. The simulated field amplitude distributions over waveguide grating at wavelengths  $\lambda = 1500$  nm and  $\lambda = 1550$  nm are shown in Fig.6.3 (b) and (c) respectively.

The wavelength range of our tunable laser does not cover the full spectrum calculated with the FDTD method. Therefore we demonstrate here the behavior of the waveguide grating for wavelengths of 1550 nm, inside the Bragg band gap, and 1500 nm which falls outside the Bragg region. The corresponding wavelengths are represented by red stars in Fig.6.3 (a).

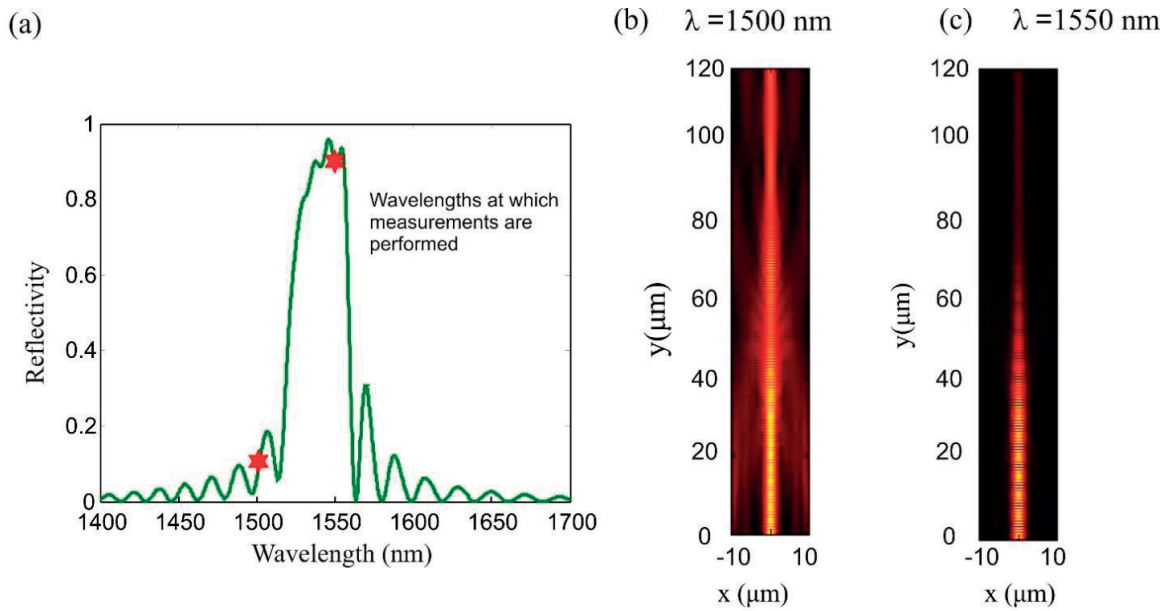


Fig.6.3 (a) Reflection spectrum of the waveguide gratings calculated using CST simulations, FDTD method. The red stars represent the wavelength region where we perform near-field measurements. (b)(c) Calculated field amplitude distribution inside waveguide grating at the wavelength  $\lambda = 1500$  nm and  $\lambda = 1550$  nm, respectively.

The MH-SNOM images and corresponding amplitude cross section at the wavelength when waveguide grating reflects the incident light are shown in Fig.6.4.

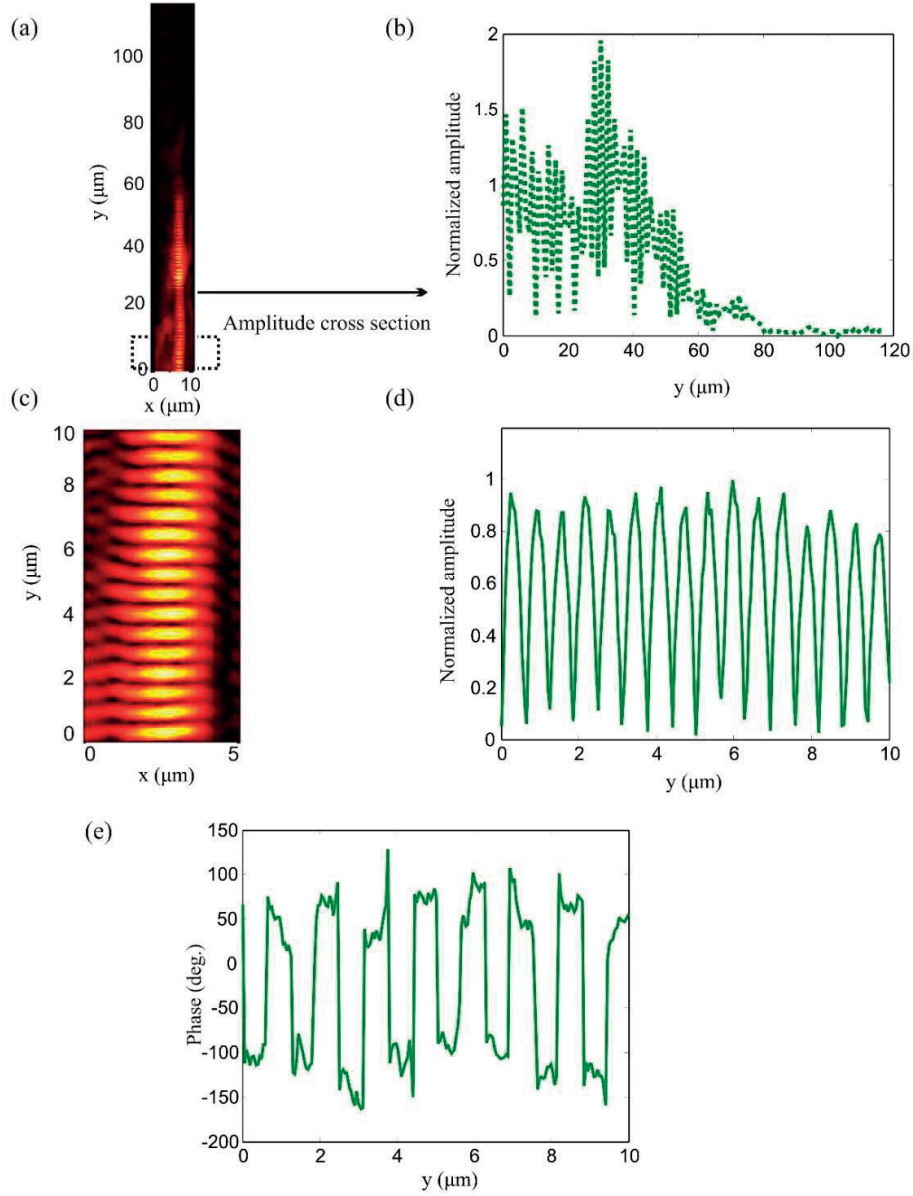


Fig.6.4. Near-field images acquired by MH-SNOM inside the photonic band gap at  $\lambda = 1550$  nm. (a) Field amplitude distribution over the waveguide grating. (b) Cross section of the field amplitude in the  $y$ -direction, along the waveguide. (c) High resolution amplitude scan in the area indicated by a black rectangle in (a). (d) Cross section of the field amplitude in the  $y$ -direction of (c). (e) Measured corresponding phase plot, representing a standing wave generated by the interference of the incident and the back reflected BSW mode.

We deduce the reflectivity  $R$  from the contrast  $C$  of the fringes, which can be defined as [9].

$$C = \frac{(A_{\max})^2 - (A_{\min})^2}{(A_{\max})^2 + (A_{\min})^2} \quad (6.1)$$

Where  $A_{\max}$  and  $A_{\min}$  are the field amplitudes at the point of maximum and consecutive minimum. The reflection coefficient ( $r$ ) is linked to the contrast by Eq.(6.2) [96].

$$C = \frac{2r}{1+r^2} \quad (6.2)$$

Figure 6.4 (a) shows the near-field amplitude distribution along the waveguide at  $\lambda = 1550$  nm. The longitudinal cross section of the surface mode propagating through the waveguide is displayed in Fig.6.4 (b), where a well pronounced interference pattern can be noticed. We assume the position of the peak amplitude as the grating input. The peak can be referred as a strong reflection and scattering from the first grating slit. To measure the fringe contrast, high resolution scan (20 points/ $\mu\text{m}$  in  $y$ -direction) at around 30  $\mu\text{m}$  before the grating is performed. The high resolution area is indicated by a black rectangle in Fig.6.4 (a). Figures 6.4 (c) and (d) represent the amplitude distribution of the interference pattern and its corresponding longitudinal cross section plot at  $\lambda = 1550$  nm. In Fig.6.4 (d), fringes are oscillating with a periodicity of 0.630  $\mu\text{m}$ . In theory, the periodicity of the interference fringes produced by a standing wave is defined by  $\lambda_{\text{eff}}/2$ . The calculated value of  $\lambda_{\text{eff}}/2$  is approximately 0.645  $\mu\text{m}$ . The value of the measured periodicity of the fringes is very close to the theoretical value. The phase of the standing wave with a periodicity of  $\lambda_{\text{eff}}$  is shown in Fig.6.4 (e). As expected for a standing wave, one can recognize the classical phase jumps from  $-\pi/2$  to  $+\pi/2$  and vice versa. The contrast of high resolution interference fringes has been calculated using Eq. (6.1). The average contrast over 13 oscillations is measured to be  $C = 0.986$ . It yields a reflection coefficient  $r = 0.8456$  (reflectivity = 71.5 %) at  $\lambda = 1550$  nm (Eq.6.2). It can be observed in Fig.6.4 (b) that the field amplitude transmitted through the slits vanishes quickly inside the grating in the Bragg mirror regime. The calculated reflection coefficient from the measured fringe contrast for 2D plasmonic Bragg mirror remains limited to 0.25, because of metal absorption [9].

The transmissivity can be deduced from the field amplitude cross section along the waveguide in Fig.6.4 (a). The estimated transmission coefficient with respect to the point around 30  $\mu\text{m}$  away from the grating is 0.05 (transmissivity = 0.25%). Considering the law of energy conservation, one

can estimate that 28 % of the incoming light will be damped by leakage to the substrate and scattering due to roughness of the side walls of the waveguide.

We perform the fast Fourier Transform (FFT) on the complex field of the high resolution amplitude scan of Fig.6.4 (c) at  $\lambda = 1550$  nm. As expected, the peaks corresponding to two counter-propagating BSWs are identified, see Fig.6.5. The counter-propagating BSWs have same wavenumber ( $f_s$ ) with a phase shift of  $\pi$  radian. Further, the reflection coefficient can be deduced from the corresponding amplitude of counter-propagating BSWs. The estimated reflection coefficient is 0.8525, which is very close to what we have calculated from measured contrast of the fringes (0.8456).

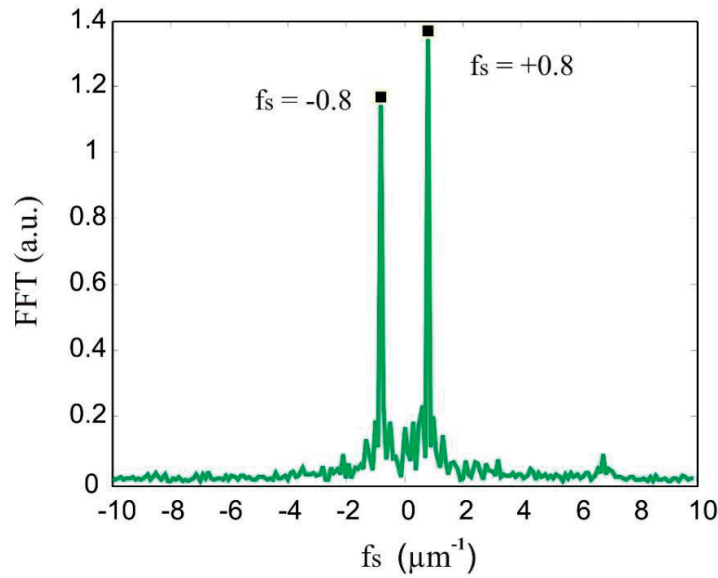


Fig.6.5. Fourier spectrum computed at on the complex field amplitude of interference fringes (in Fig.6.4 (c)) at  $\lambda = 1550$  nm. The peaks corresponds to wavenumbers of two counter-propagating BSWs.

We perform the measurements at  $\lambda = 1500$  nm (outside the photonic band gap of the waveguide grating) following the same procedure than for  $\lambda = 1550$  nm. The near-field amplitude distribution along the waveguide is shown in Fig.6.6 (a) and the corresponding cross section in Fig. 6.6 (b). On the high resolution scan, see Figs.6.6 (c) and (d), only very weak interference fringes can be seen. The value of the measured contrast (averaged over 13 oscillations) is  $C = 0.187$ . A very low contrast fringe pattern can be attributed to a weak back reflection of the incident BSW and hence a low reflectivity which is evident from the amplitude distribution shown in Fig.6.6 (a).



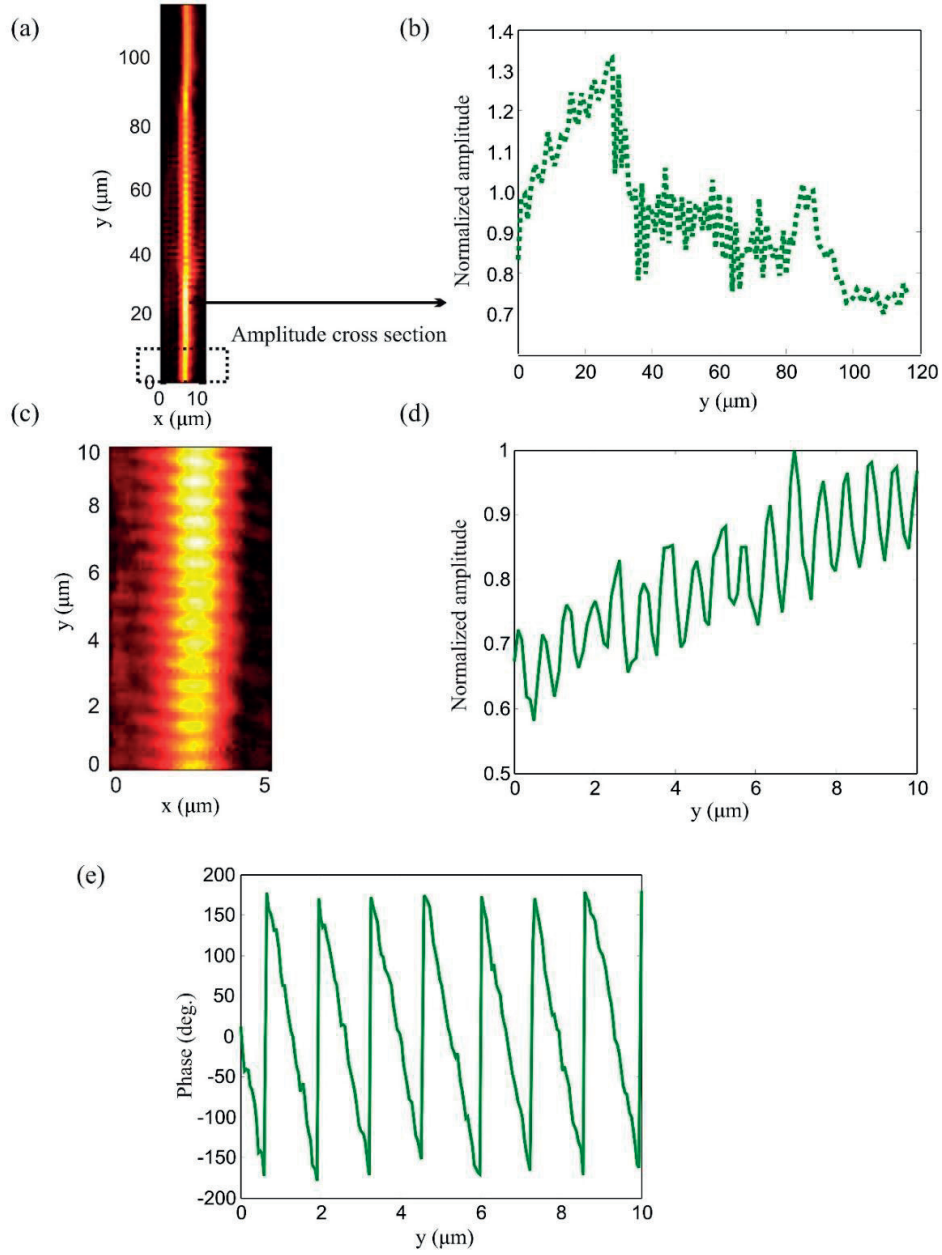


Fig.6.6. Near-field images acquired by MH-SNOM outside the photonic band gap at  $\lambda = 1500$  nm. (a) Field amplitude distribution over the waveguide grating. (b) Cross section of the field amplitude in the y-direction along the waveguide. (c) High resolution amplitude scan in the area indicated by a black rectangle in (a). (d) Cross section of the field amplitude in the y-direction of (c). (e) Phase plot showing a propagating plane wave behavior which indicates very weak reflection at 1500 nm.

Light propagates through the waveguide with the least effect of presence of grating. The calculated corresponding value of the reflection coefficient (reflectivity), from the measured contrast, is approximately 0.94 (0.89 %) at  $\lambda = 1500$  nm. In other way, it can be inferred that most of the light is transmitting at wavelength of 1500 nm. We perform the phase measurement  $30\text{ }\mu\text{m}$  before the gratings, see Fig.6.6 (e). We obtain a phase plot signature of a propagative plane wave without the influence of interference of back reflected light because of a very weak reflection, proving that the measurement is done outside the photonic band gap. The estimated transmission coefficient (transmissivity) from the field amplitude plot in Fig.6.6 (b) is 0.72 (52%). The propagation losses can be deduced following the conservation of energy, which are 48%.

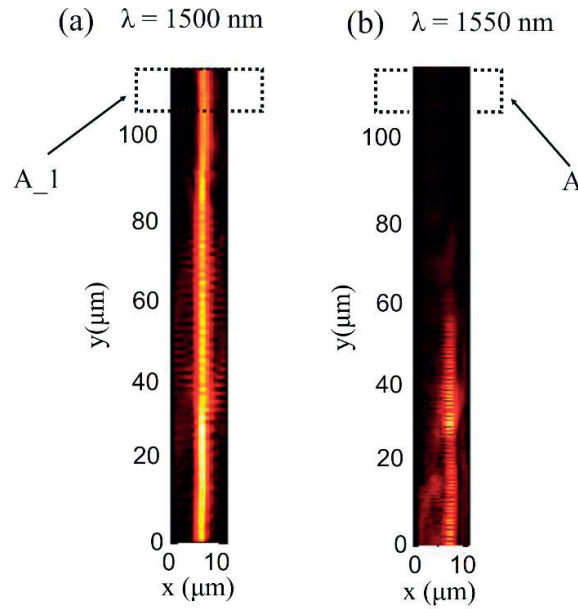


Fig.6.7. The field amplitude distribution over the waveguide grating at (a)  $\lambda = 1500$  nm and (b)  $\lambda = 1550$  nm, measured by MH-SNOM. The black rectangles indicate the areas over which integration has been performed.

The reflection coefficient  $r$ , of the waveguide grating can also be deduced by integration of field amplitude distribution at the equidistant area from the grating at  $\lambda = 1500$  nm (at transmission) and  $\lambda = 1550$  nm (at reflection). We perform simple calculation to deduce reflection coefficient, using Eq.6.3.



$$r = \left( \frac{A_{-1} - A}{A_{-1}} \right) * 100 \quad (6.3)$$

The area  $A_{-1}$  and  $A$  are indicated with black rectangles (around 35  $\mu\text{m}$  away from the end of grating) in Fig.6.7 (a, b). The calculated reflection coefficient is approximately 0.68 which is reasonable considering the higher propagation losses inside the waveguide at wavelength  $\lambda = 1500$  nm (at transmission).

### 6.3 Conclusion

In summary, for the first time a waveguide grating engraved into a Bloch surface wave based waveguide is realized and experimentally analyzed as a flat Bragg mirror. The gratings are engraved in a 2  $\mu\text{m}$ -wide waveguide by e-beam lithography. The MH-SNOM is used to map the near-field amplitude distribution of a BSW propagating along the structure. The waveguide grating shows the expected Bragg mirror behavior with a measured reflection coefficient of approximately 0.8456 (reflectivity = 71.5 %) inside the photonic band gap at  $\lambda = 1550$  nm. We also deduce the reflectivity using some other methods (FFT and area integration), the value of which lies close to the one obtained from the contrast of the fringes. We demonstrate the complete transmission outside the forbidden band at  $\lambda = 1500$  nm. The near-field images of the grating show high contrast interference fringes at  $\lambda = 1550$  nm. This standing wave pattern is found to arise from the interference of two counter-propagating BSWs. It is shown that a very low contrast attributed to a weak back reflection and hence to a low reflectivity at  $\lambda = 1500$  nm. The FDTD simulations and near-field measurements confirm that waveguide grating works as a Bragg reflector at telecommunication wavelength. We believe that this study enables a step forward in the direction of the development of BSWs based 2D integrated optical systems.



# CHAPTER 7

## Conclusion and Future Prospects

The main objective of this thesis is to investigate and demonstrate that the dielectric multilayer sustaining Bloch surface waves can be exploited as a platform for planar optics. To this aim, the six periods of multilayers, silicon dioxide and silicon nitride, are deposited on a glass wafer using plasma enhanced chemical vapor deposition technique. To develop the compact and low loss 2D optical components and systems, we study titanium dioxide as a device layer of high refractive index material, which has been deposited on the top of multilayer platform. Further, various 2D optical components including disk resonator, 2D Bessel-like beam generator and waveguide grating, are patterned into the high refractive index material device layer on the top of multilayer platform. To structure the optical components, we use electron beam lithography.

To couple the Bloch surface waves into multilayers, total internal configuration is utilized. The coupling configuration consists of a glass prism to match the propagation vector condition in order to excite Bloch surface waves. The near-field characterization of 2D optical devices is performed with the aid of multi-heterodyne scanning near-field microscopy. This is the most efficient tool to directly access the spatial distribution of the surface mode, because of the evanescent character of Bloch surface waves.

The device layer of high refractive index material on the top of multilayer manipulates the propagation properties of Bloch surface wave modes. The propagation length and effective refractive index are the two prominent propagation properties of Bloch surface waves. They determine the losses associated with the multilayer platform and the optical properties of the surface modes and hence the optical components. We study theoretically and experimentally the propagation properties of Bloch surface waves for different thicknesses of titanium dioxide with the aim to determine the thickness of the 2D optical components which are patterned into the device layer.

For this particular design of the multilayer platform, the longest obtained propagation length is approximately 3.24 millimeter for a 30 nm thick titanium dioxide layer. The dispersion curve is located near to the middle of the photonic band gap where theory suggests stronger attenuation. However, this is not the limit, higher values might be achieved using grating couplers. We demonstrate that by tailoring the thickness of the device layer a surface mode can be shaped differently according to the application, for example integrated optics or sensing. The effective refractive index contrast is studied in order to develop low loss and compact photonic devices. We obtain a refractive index contrast close to 0.15 for 60 nm of titanium dioxide layer. In theory, a refractive index contrast up to 0.2 can be achieved for 100 nm thickness of titanium dioxide. The propagation properties of Bloch surface waves are compared in the near-field, far-field and in theory. The experimental results show a good agreement with the theoretical results. In addition to the valuable increase of the propagation length of the Bloch surface waves, we also demonstrate that a device layer allows fine tuning of the BSW resonance frequency, which can thus be positioned at any place within the photonic band gap. Based on the obtained results, we design and fabricate the 2D optical components into 60 nm thickness of titanium dioxide.

Dielectric ring/disk resonators are part of the key building blocks of integrated optical systems. These structures can be used as channel-drop filters, all-optical logic gates, optical frequency division multiplexers and sensors. We present the very first experimental demonstration of a Bloch surface waves based 2D disk resonator. The 2D disk resonator is fabricated into a thin layer ( $\sim\lambda/25$ ) of titanium dioxide on the top of a dielectric periodic stack. Thanks to low loss characteristics of the dielectric multilayer platform, we obtain higher quality factor for Bloch surface waves based resonators in comparison to plasmonic resonators (more than an order of magnitude). To measure the quality factor of the resonator, we perform a wavelength scan at the through port. For a disk radius of 100  $\mu\text{m}$  and gap spacing 0.5  $\mu\text{m}$ , the measured quality factor is approximately  $2 \times 10^3$ . The calculated quality factor, using CST microwave studio simulations (FDTD method), is approximately  $2 \times 10^4$ . In experiments, the scattering losses, fabrication imperfections and leakage are the dominant reasons of degradation the quality factor.

The spreading of the beam in the transverse direction is a source of coupling losses in on chip interconnects. For this purpose, we study 2D Bessel-like beams, which possess a long and tight focus spot. We study theoretically and experimentally a 2D isosceles triangle/axicon to generate 2D Bessel-like quasi-non-diffracting beams, which is fabricated into a thin layer ( $\sim\lambda/25$ ) of titanium dioxide layer deposited on the top of the multilayer platform. We investigate different designs of 2D axicons, where the height of the axicon varied from 20  $\mu\text{m}$  to 30  $\mu\text{m}$  with a step of 5  $\mu\text{m}$ . The purpose of studying different designs is to compare the optical performance of 2D Bessel-like beams, in particular propagation distance and full width at half maximum. We calculate the optical

parameter of the 2D Bessel-like beams using CST simulations based on FDTD method. The results obtained from experiments are in good agreement with the simulation results. We demonstrate in near-field that the long focus spot propagates without significant spreading for considerable propagation distances. The study provides the deep understanding of optical properties of 2D Bessel-like beams which can be controlled by the design parameters of the 2D axicon with the aim of desired applications (long focus/tighter confinement) behind. We obtain a significantly longer propagating focus spot than the SPPs based 2D Cosine-Gauss beams, thanks to the low loss characteristics of Bloch surface waves. These beams can be used as a low loss (coupling) optical interconnects between on-chip components and optical tweezers.

Further, we study theoretically and experimentally the gratings engraved into Bloch surface waves based waveguides and demonstrate in the near-field that the waveguide grating can perform as 2D Bragg mirror. The fringe pattern produced by interference of incident and back reflected light is recorded with multi-heterodyne scanning near-field microscopy. The reflectivity is deduced from the contrast of measured fringes. We have shown that in the photonics band gap, which is calculated with the FDTD method using CST microwave studio simulations, the waveguide grating works as a reflector (reflectivity of approximately 71.5 % inside the photonic band gap at  $\lambda = 1550$  nm) and outside the band gap it works as a transmitter. Besides, the phase of the standing wave pattern arises from the interference of two counter-propagating Bloch surface waves is measured, when the waveguide grating work as a reflector. However, in transmission we obtain the phase of plane waves, proving the very weak reflection from the waveguide grating. The presented waveguide gratings can be used as a Bragg mirror for 2D optics at telecommunication wavelengths. This study could be helpful as an initial step to realize Bloch surface waves based Fabry-Perot resonators.

To summarize, the main objective of the thesis has been achieved. The propagation properties of Bloch surface waves have been studied for different thicknesses of titanium dioxide as a high refractive index material device layer. We achieved significantly improved propagation lengths in comparison to the one obtained by L. Yu *et al.* [45]. Further, different 2D optical components have been fabricated into 60 nm ( $\sim \lambda/25$ ) thickness of titanium dioxide on the top of multilayer platform. These elements include, 2D disk resonator, 2D Bessel-like beam generator and 2D waveguide grating as a Bragg mirror. This thesis presents the very first theoretical and experimental demonstration of aforementioned 2D optical components based on BSWs platform. The 2D optical components have been characterized in the near-field. The significant improvement in the performance of optical components in comparison to plasmonics based 2D optical devices has been reported, thanks to low loss characteristics of Bloch surface waves. This work provides the understanding of the optical properties of Bloch surface waves when it is manipulated by different

2D structures. The presented results contribute to an advancement in the direction of developing 2D integrated optical systems based on Bloch surface waves.

Hereafter, we discuss the future perspective of this work in terms of improving the design of the multilayer platform, optimizing the performance of 2D optical components and the contribution of the work to the evolution of further BSWs based 2D optical components for sensing and integrated optics applications. As discussed in chapter 3, the leakage into the multilayer because of prism coupling is the main loss mechanism in our system. We expect that the propagation lengths can be increased in the range of centimeters using grating couplers. The concept of grating couplers has already been proven on the BSWs based platform [61]. However, the prism coupling allows to exploit a single coupling configuration to study different 2D optical component with minimum complexity in the near-field characterization experiments.

The quality factor of the disk resonators can be improved by reducing the propagation losses of the system (using grating coupler). Further efforts are ongoing to improve the design of the resonator, by adjusting the gap spacing, to achieve higher extinction ratios at through port. In addition, the coupling efficiency of the incident BSW into the input waveguide of the resonator can be increased using a triangular coupler. This will lead to the enhanced signal to noise ratio inside the disk. We compromise the footprint of 2D devices with the optical performance. The 2D components with smaller dimensions can be realized by using higher refractive index materials as a device layer, e.g., silicon.

With the aim realizing BSWs based detectors, we studied Graphene as a device layer. The propagation lengths are reduced drastically in comparison to BML. Our preliminary experimental results show strong absorption of BSW in the presence of a single layer of Graphene. The results are not included as a part of this thesis. To understand deeply the absorption properties of Graphene layer on BSWs based platform, future investigations are required. The Graphene layer can also serve as a foundation to realize BSWs based active/tunable components.

Furthermore, the study of the 2D Bragg mirror, presented in this thesis, provides an insight to realize BSWs based Fabry-Perot resonators.



## List of abbreviations

**AFM** Atomic Force Microscope

**AOM** Acousto-Optic Modulator

**ALD** Atomic layer deposition

**BS** Beam splitter

**BSWs** Bloch surface waves

**EBL** E-beam lithography

**FDTD** finite-difference time-domain

**FF** Far- field

**FFT** Fast Fourier Transform

**FSR** Free-Spectral Range

**FWHM** full width of half maximum

**IMI** Insulator-Metal-Insulator

**MH-SNOM** multi-heterodyne scanning near-field optical microscope

**MIM** Metal-Insulator-Metal

**NF** Near-field

**PBS** Polarizing Beam Splitter



**PECVD** Plasma enhanced chemical vapor deposition

**PMF** Polarization Maintaining Fiber

***Q*-factor** Quality factor

**RCWA** rigorous coupled-wave analysis

**SEM** Scanning Electron Microscope

**SMF** Single Mode Fiber

**SNOM** scanning near-field optical microscope

**STM** Scanning Tunneling Microscope

**TE** transverse electric

**TIR** total internal reflection

**TM** transverse magnetic

**2D** Two-dimensional



## Bibliography

- [1] P. Yeh, A. Yariv, and A. Y. Cho, “Optical surface waves in periodic layered media,” *Appl. Phys. Lett.*, vol. **32**, no. 2, p. 104, 1978.
- [2] W. L. Barnes, A. Dereux, and T. W. Ebbesen, “Surface plasmon subwavelength optics,” *Nature*, vol. **424**, no. 6950, pp. 824–830, 2003.
- [3] A. V. Zayats and I. I. Smolyaninov, “Near-field photonics: surface plasmon polaritons and localized surface plasmons,” *J. Opt. Pure Appl. Opt.*, vol. **5**, no. 4, p. S16, 2003.
- [4] K. V. Sreekanth, S. Zeng, J. Shang, K.-T. Yong, and T. Yu, “Excitation of surface electromagnetic waves in a graphene-based Bragg grating,” *Sci. Rep.*, vol. **2**, 2012.
- [5] N. Danz, A. Sinibaldi, F. Michelotti, E. Descrovi, P. Munzert, U. Schulz, and F. Sonntag, “Improving the sensitivity of optical biosensors by means of Bloch surface waves,” *Biomed Tech*, vol. **57**, p. 1, 2012.
- [6] J. Gao, A. M. Sarangan, and Q. Zhan, “Polarization multiplexed fluorescence enhancer using a pixelated one-dimensional photonic band gap structure,” *Opt. Lett.*, vol. 37, no. **13**, pp. 2640–2642, 2012.
- [7] W. M. Robertson, “Experimental measurement of the effect of termination on surface electromagnetic waves in one-dimensional photonic bandgap arrays,” *J. Light. Technol.*, vol. **17**, no. 11, p. 2013, 1999.
- [8] V. N. Konopsky and E. V. Alieva, “Photonic Crystal Surface Waves for Optical Biosensors,” *Anal. Chem.*, vol. **79**, no. 12, pp. 4729–4735, 2007.
- [9] J.-C. Weeber, Y. Lacroute, A. Dereux, E. Devaux, T. Ebbesen, C. Girard, M. U. González, and A.-L. Baudrion, “Near-field characterization of Bragg mirrors engraved in surface plasmon waveguides,” *Phys. Rev. B*, vol. **70**, no. 23, 2004.
- [10] M. U. González, J.-C. Weeber, A.-L. Baudrion, A. Dereux, A. L. Stepanov, J. R. Krenn, E. Devaux, and T. W. Ebbesen, “Design, near-field characterization, and modeling of surface-plasmon Bragg mirrors,” *Phys. Rev. B*, vol. **73**, no. 15, p. 155416, 2006.

- [11] J. A. Sánchez-Gil, “Surface defect scattering of surface plasmon polaritons: Mirrors and light emitters,” *Appl. Phys. Lett.*, vol. **73**, no. 24, pp. 3509–3511, 1998.
- [12] J. Lin, J. Dellinger, P. Genevet, B. Cluzel, F. De Fornel, and F. Capasso, “Cosine-Gauss plasmon beam: a localized long-range nondiffracting surface wave,” *Phys. Rev. Lett.*, vol. **109**, no. 9, p. 093904, 2012.
- [13] C. E. Garcia-Ortiz, V. Coello, Z. Han, and S. I. Bozhevolnyi, “Generation of diffraction-free plasmonic beams with one-dimensional Bessel profiles,” *Opt. Lett.*, vol. **38**, no. 6, pp. 905–907, 2013.
- [14] S. I. Bozhevolnyi, V. S. Volkov, E. Devaux, J.-Y. Laluet, and T. W. Ebbesen, “Channel plasmon subwavelength waveguide components including interferometers and ring resonators,” *Nature*, vol. **440**, no. 7083, pp. 508–511, 2006.
- [15] Z. Gu, S. Liu, S. Sun, K. Wang, Q. Lyu, S. Xiao and Q. Song, “Photon hopping and nanowire based hybrid plasmonic ring-resonator,” *Sci. Rep.*, vol. **5**, 2015.
- [16] Y. Gong, L. Wang, X. Hu, X. Li, and X. Liu, “Broad-bandgap and low-sidelobe surface plasmon polariton reflector with Bragg-grating-based MIM waveguide,” *Opt. Express*, vol. **17**, no. 16, pp. 13727–13736, 2009.
- [17] A. Boltasseva, T. Søndergaard, T. Nikolajsen, K. Leosson, S. I. Bozhevolnyi, and J. M. Hvam, “Propagation of long-range surface plasmon polaritons in photonic crystals,” *JOSA B*, vol. **22**, no. 9, pp. 2027–2038, 2005.
- [18] J.-C. Weeber, A. Dereux, C. Girard, J. R. Krenn, and J.-P. Goudonnet, “Plasmon polaritons of metallic nanowires for controlling submicron propagation of light,” *Phys. Rev. B*, vol. **60**, no. 12, pp. 9061–9068, 1999.
- [19] N. N. Feng, M. L. Brongersma, and L. D. Negro, “Metal-Dielectric Slot-Waveguide Structures for the Propagation of Surface Plasmon Polaritons at 1.55  $\mu\text{m}$ ,” *IEEE J. Quantum Electron.*, vol. **43**, no. 6, pp. 479–485, 2007.
- [20] S. I. Bozhevolnyi, V. S. Volkov, E. Devaux, and T. W. Ebbesen, “Channel Plasmon-Polariton Guiding by Subwavelength Metal Grooves,” *Phys. Rev. Lett.*, vol. **95**, no. 4, p. 046802, 2005.
- [21] H.-S. Chu, W.-B. Ewe, and E.-P. Li, “Tunable propagation of light through a coupled-bent dielectric-loaded plasmonic waveguides,” *J. Appl. Phys.*, vol. **106**, no. 10, p. 106101, 2009.
- [22] R. F. Oulton, V. J. Sorger, D. A. Genov, D. F. P. Pile, and X. Zhang, “A hybrid plasmonic waveguide for subwavelength confinement and long-range propagation,” *Nat. Photonics*, vol. **2**, no. 8, pp. 496–500, 2008.
- [23] Z. Liu, J. M. Steele, W. Srituravanich, Y. Pikus, C. Sun, and X. Zhang, “Focusing surface plasmons with a plasmonic lens,” *Nano Lett.*, vol. **5**, no. 9, pp. 1726–1729, 2005.

- [24] L. Yin, V. K. Vlasko-Vlasov, J. Pearson, J. M. Hiller, J. Hua, U. Welp, D. E. Brown, and C. W. Kimball, "Subwavelength Focusing and Guiding of Surface Plasmons," *Nano Lett.*, vol. **5**, no. 7, pp. 1399–1402, 2005.
- [25] Z. Han, L. Liu, and E. Forsberg, "Ultra-compact directional couplers and Mach–Zehnder interferometers employing surface plasmon polaritons," *Opt. Commun.*, vol. **259**, no. 2, pp. 690–695, 2006.
- [26] M. Kaliteevski, I. Iorsh, S. Brand, R. A. Abram, J. M. Chamberlain, A. V. Kavokin, and I. A. Shelykh, "Tamm plasmon-polaritons: Possible electromagnetic states at the interface of a metal and a dielectric Bragg mirror," *Phys. Rev. B*, vol. **76**, no. 16, 2007.
- [27] M. E. Sasin, R. P. Seisyan, M. A. Kaliteevski, S. Brand, R. A. Abram, J. M. Chamberlain, I. V. Iorsh, I. A. Shelykh, A. Y. Egorov, A. P. Vasil'ev, V. S. Mikhlin, and A. V. Kavokin, "Tamm plasmon-polaritons: First experimental observation," *Superlattices Microstruct.*, vol. **47**, no. 1, pp. 44–49, 2010.
- [28] M.A. Paesler and P. J. Moyer, "Near-Field Optics: Theory, Instrumentation, and Applications," *Wiley*, 1996.
- [29] G. Binnig, H. Rohrer, C. Gerber, and E. Weibel, "Surface studies by scanning tunneling microscopy," *Phys. Rev. Lett.*, vol. **49**, p. 57, 1982.
- [30] G. Binnig, C. F. Quate, and C. Gerber, "Atomic force microscope," *Phys. Rev. Lett.*, vol. **56**, no. 9, p. 930, 1986.
- [31] D. W. Pohl, W. Denk, and M. Lanz, "Optical stethoscopy: Image recording with resolution  $\lambda/20$ ," *Appl. Phys. Lett.*, vol. **44**, no. 7, pp. 651–653, 1984.
- [32] D. Courjon, J.-M. Vigoureux, M. Spajer, K. Sarayedine, and S. Leblanc, "External and internal reflection near field microscopy: experiments and results," *Appl. Opt.*, vol. **29**, no. 26, pp. 3734–3740, 1990.
- [33] B. Hecht, D. W. Pohl, H. Heinzelmann, and L. Novotny, "'Tunnel' near-field optical microscopy: TNOM-2," *Ultramicroscopy*, vol. **61**, no. 1–4, pp. 99–104, 1995.
- [34] R. Dändliker, "Heterodyne, quasi-heterodyne and after," in *Fringe 2005*, Springer, Berlin, Heidelberg, pp. 65–73, 2006.
- [35] R. Dändliker, "I Heterodyne Holographic Interferometry," *Prog. Opt.*, vol. **17**, pp. 1–84, 1980.
- [36] A. Nesci, R. Dändliker, M. Salt, and H. P. Herzig, "Measuring amplitude and phase distribution of fields generated by gratings with sub-wavelength resolution," *Opt. Commun.*, vol. **205**, no. 4–6, pp. 229–238, 2002.

- [37] R. Dändliker, P. Tortora, L. Vaccaro, and A. Nesci, “Measuring three-dimensional polarization with scanning optical probes,” *J. Opt. Pure Appl. Opt.*, vol. **6**, no. 3, p. S18, 2004.
- [38] P. Tortora, M. Abashin, I. Märki, W. Nakagawa, L. Vaccaro, M. Salt, H.-P. Herzig, U. Levy, and Y. Fainman, “Observation of amplitude and phase in ridge and photonic crystal waveguides operating at 1.55  $\mu\text{m}$  by use of heterodyne scanning near-field optical microscopy,” *Opt. Lett.*, vol. **30**, no. 21, pp. 2885–2887, 2005.
- [39] T. Sfez, “Investigation of Surface Electromagnetic Waves with Multi-Heterodyne Scanning Near-Field Optical Microscopy,” PhD Dissertation, École polytechnique fédérale de Lausanne, 2010.
- [40] Lukas Novotny, “Principles of Nano-Optics,” *Cambridge Core*, 2006.
- [41] T. Sfez, E. Descrovi, L. Yu, D. Brunazzo, M. Quaglio, L. Dominici, W. Nakagawa, F. Michelotti, F. Giorgis, and O. J. Martin, “Bloch surface waves in ultrathin waveguides: near-field investigation of mode polarization and propagation,” *JOSA B*, vol. **27**, no. 8, pp. 1617–1625, 2010.
- [42] T. Sfez, E. Descrovi, L. Dominici, W. Nakagawa, F. Michelotti, F. Giorgis, and H.-P. Herzig, “Near-field analysis of surface electromagnetic waves in the bandgap region of a polymeric grating written on a one-dimensional photonic crystal,” *Appl. Phys. Lett.*, vol. **93**, no. 6, p. 061108, 2008.
- [43] E. Descrovi, T. Sfez, M. Quaglio, D. Brunazzo, L. Dominici, F. Michelotti, H. P. Herzig, O. J. F. Martin, and F. Giorgis, “Guided Bloch Surface Waves on Ultrathin Polymeric Ridges,” *Nano Lett.*, vol. **10**, no. 6, pp. 2087–2091, 2010.
- [44] T. Sfez, E. Descrovi, L. Yu, M. Quaglio, L. Dominici, W. Nakagawa, F. Michelotti, F. Giorgis, and H. P. Herzig, “Two-dimensional optics on silicon nitride multilayer: Refraction of Bloch surface waves,” *Appl. Phys. Lett.*, vol. **96**, no. 15, p. 151101, 2010.
- [45] L. Yu, E. Barakat, T. Sfez, L. Hvozdar, J. Di Francesco, and H. Peter Herzig, “Manipulating Bloch surface waves in 2D: a platform concept-based flat lens,” *Light Sci. Appl.*, vol. **3**, no. 1, p. e124, 2014.
- [46] L. Yu, E. Barakat, J. Di Francesco, and H. P. Herzig, “Two-dimensional polymer grating and prism on Bloch surface waves platform,” *Opt. Express*, vol. **23**, no. 25, p. 31640, 2015.
- [47] L. Yu, E. Barakat, W. Nakagawa, and H. P. Herzig, “Investigation of ultra-thin waveguide arrays on a Bloch surface wave platform,” *J. Opt. Soc. Am. B*, vol. **31**, no. 12, p. 2996, 2014.
- [48] E. Descrovi, F. Frascella, B. Sciacca, F. Geobaldo, L. Dominici, and F. Michelotti, “Coupling of surface waves in highly defined one-dimensional porous silicon photonic crystals for gas sensing applications,” *Appl. Phys. Lett.*, vol. **91**, no. 24, p. 241109, 2007.

- [49] F. Giorgis, E. Descrovi, C. Summonte, L. Dominici, and F. Michelotti, "Experimental determination of the sensitivity of Bloch surface waves based sensors," *Opt. Express*, vol. **18**, no. 8, pp. 8087–8093, 2010.
- [50] A. Sinibaldi, N. Danz, E. Descrovi, P. Munzert, U. Schulz, F. Sonntag, L. Dominici, and F. Michelotti, "Direct comparison of the performance of Bloch surface wave and surface plasmon polariton sensors," *Sens. Actuators B Chem.*, vol. **174**, pp. 292–298, 2012.
- [51] M. Liscidini and J. E. Sipe, "Analysis of Bloch-surface-wave assisted diffraction-based biosensors," *JOSA B*, vol. **26**, no. 2, pp. 279–289, 2009.
- [52] V. Paeder, V. Musi, L. Hvozdar, S. Herminjard, and H. P. Herzig, "Detection of protein aggregation with a Bloch surface wave based sensor," *Sens. Actuators B Chem.*, vol. **157**, no. 1, pp. 260–264, 2011.
- [53] S. Pirotta, X. G. Xu, A. Delfan, S. Mysore, S. Maiti, G. Dacarro, M. Patrini, M. Galli, G. Guizzetti, and D. Bajoni, "Surface-enhanced Raman scattering in purely dielectric structures via Bloch surface waves," *J. Phys. Chem. C*, vol. **117**, no. 13, pp. 6821–6825, 2013.
- [54] A. Delfan, M. Liscidini, and J. E. Sipe, "Surface enhanced Raman scattering in the presence of multilayer dielectric structures," *JOSA B*, vol. **29**, no. 8, pp. 1863–1874, 2012.
- [55] I. V. Sobleva, E. Descrovi, C. Summonte, A. A. Fedyanin, and F. Giorgis, "Fluorescence emission enhanced by surface electromagnetic waves on one-dimensional photonic crystals," *Appl. Phys. Lett.*, vol. **94**, no. 23, p. 231122, 2009.
- [56] M. Scaravilli, G. Castaldi, A. Cusano, and V. Galdi, "Grating-coupling-based excitation of Bloch surface waves for lab-on-fiber optrodes," *Opt. Express*, vol. **24**, no. 24, pp. 27771–27784, 2016.
- [57] L. L. Doskolovich, E. A. Bezus, D. A. Bykov, and V. A. Soifer, "Spatial differentiation of Bloch surface wave beams using an on-chip phase-shifted Bragg grating," *J. Opt.*, vol. **18**, no. 11, p. 115006, 2016.
- [58] V. Koju and W. M. Robertson, "Excitation of Bloch-like surface waves in quasi-crystals and aperiodic dielectric multilayers," *Opt. Lett.*, vol. **41**, no. 13, p. 2915, 2016.
- [59] M. Menotti and M. Liscidini, "Optical resonators based on Bloch surface waves," *J. Opt. Soc. Am. B*, vol. **32**, no. 3, p. 431, 2015.
- [60] V. Koju and W. M. Robertson, "Slow light by Bloch surface wave tunneling," *Opt. Express*, vol. **22**, no. 13, pp. 15679–15685, 2014.
- [61] T. Kovalevich, P. Boyer, M. Suarez, R. Salut, M.-S. Kim, H. P. Herzig, M.-P. Bernal, and T. Grosjean, "Polarization controlled directional propagation of Bloch surface wave," *Opt. Express*, vol. **25**, no. 5, pp. 5710–5715, 2017.

- [62] T. Kovalevich, A. Ndao, M. Suarez, S. Tumenas, Z. Balevicius, A. Ramanavicius, I. Baleviciute, M. Häyrynen, M. Roussey, M. Kuittinen, T. Grosjean, and M.-P. Bernal, “Tunable Bloch surface waves in anisotropic photonic crystals based on lithium niobate thin films,” *Opt. Lett.*, vol. **41**, no. 23, pp. 5616–5619, 2016.
- [63] E. Bontempi, L. E. Depero, L. Sangaletti, F. Giorgis, and C. F. Pirri, “Growth process analysis of a-Si<sub>1-x</sub>N<sub>x</sub>:H films probed by X-ray reflectivity,” *Mater. Chem. Phys.*, vol. **66**, no. 2–3, pp. 172–176, Oct. 2000.
- [64] M. Hayrinen, M. Roussey, V. Gandhi, P. Stenberg, A. Saynatjoki, L. Karvonen, M. Kuittinen, and S. Honkanen, “Low-Loss Titanium Dioxide Strip Waveguides Fabricated by Atomic Layer Deposition,” *J. Light. Technol.*, vol. **32**, no. 2, pp. 208–212, 2014.
- [65] X. Wu, E. Barakat, L. Yu, L. Sun, J. Wang, Q. Tan, and H. P. Herzig, “Phase-sensitive near field Investigation of Bloch surface wave propagation in curved waveguides,” *J. Eur. Opt. Soc.-Rapid Publ.*, vol. **9**, pp. (14049-1) – (14049-8), 2014.
- [66] R. Ulrich, “Theory of the prism-film coupler by plane-wave analysis,” *JOSA*, vol. **60**, no. 10, pp. 1337–1350, 1970.
- [67] J. Gaspar-Armenta, “Surface waves in finite one-dimensional photonic crystals: mode coupling,” *Opt. Commun.*, vol. **216**, no. 4–6, pp. 379–384, 2003.
- [68] V. N. Konopsky, “Plasmon-polariton waves in nanofilms on one-dimensional photonic crystal surfaces,” *New J. Phys.*, vol. **12**, no. 9, p. 093006, 2010.
- [69] A. Yariv and P. Yeh, “*Photonics : optical electronics in modern communications*,” New York Oxford University Press, 2007.
- [70] V. Paeder, “Bloch Surface Wave Biosensing: Study of Optical Elements for the Early Detection of Protein Aggregation,” PhD Dissertation, École polytechnique fédérale de Lausanne, 2011.
- [71] M. Leskelä and M. Ritala, “Atomic layer deposition (ALD): from precursors to thin film structures,” *Thin Solid Films*, vol. **409**, no. 1, pp. 138–146, 2002.
- [72] P. Yeh, A. Yariv, and C.-S. Hong, “Electromagnetic propagation in periodic stratified media. I. General theory,” *JOSA*, vol. **67**, no. 4, pp. 423–438, 1977.
- [73] I. V. Soboleva, V. V. Moskalenko, and A. A. Fedyanin, “Giant Goos-Hänchen Effect and Fano Resonance at Photonic Crystal Surfaces,” *Phys. Rev. Lett.*, vol. **108**, no. 12, 2012.
- [74] P. K. Tien, R. Ulrich, and R. J. Martin, “Modes of propagating light waves in thin deposited semiconductor films,” *Appl. Phys. Lett.*, vol. **14**, no. 9, pp. 291–294, 1969.
- [75] V. N. Konopsky and E. V. Alieva, “Observation of fine interference structures at total internal reflection of focused light beams,” *Phys. Rev. A*, vol. **86**, no. 6, p. 063807, 2012.



- [76] E. Descrovi, T. Sfez, L. Dominici, W. Nakagawa, F. Michelotti, F. Giorgis, and H.-P. Herzig, "Near-field imaging of Bloch surface waves on silicon nitride one-dimensional photonic crystals," *Opt. Express*, vol. **16**, no. 8, pp. 5453–5464, 2008.
- [77] S. C. Hagness, D. Rafizadeh, S. T. Ho, and A. Taflove, "FDTD microcavity simulations: design and experimental realization of waveguide-coupled single-mode ring and whispering-gallery-mode disk resonators," *Light. Technol. J. Of*, vol. **15**, no. 11, pp. 2154–2165, 1997.
- [78] T. Chang, "Coupled mode theory for modeling microring resonators," *Opt. Eng.*, vol. **44**, no. 8, p. 084601, 2005.
- [79] M. Soltani, S. Yegnanarayanan, Q. Li, and A. Adibi, "Systematic Engineering of Waveguide-Resonator Coupling for Silicon Microring/Microdisk/Racetrack Resonators: Theory and Experiment," *IEEE J. Quantum Electron*, vol. **46**, no. 8, pp. 1158–1169, 2010.
- [80] B. E. Little, S. T. Chu, H. A. Haus, J. Foresi, and J.-P. Laine, "Microring resonator channel dropping filters," *J. Light. Technol.*, vol. **15**, no. 6, pp. 998–1005, 1997.
- [81] B. Liu, A. Shakouri, and J. E. Bowers, "Wide tunable double ring resonator coupled lasers," *IEEE Photonics Technol. Lett.*, vol. **14**, no. 5, pp. 600–602, 2002.
- [82] F. Frascella, C. Petri, S. Ricciardi, L. Napione, P. Munzert, U. Jonas, J. Dostalek, F. Bussolino, C. Fabrizio Pirri, and E. Descrovi, "Hydrogel-Terminated Photonic Crystal for Label-Free Detection of Angiopoietin-1," *J. Light. Technol.*, vol. **34**, no. 15, pp. 3641–3645, 2016.
- [83] A. Hosseini and Y. Massoud, "Nanoscale surface plasmon based resonator using rectangular geometry," *Appl. Phys. Lett.*, vol. **90**, no. 18, p. 181102, 2007.
- [84] N. Talebi, A. Mahjoubfar, and M. Shahabadi, "Plasmonic ring resonator," *JOSA B*, vol. **25**, no. 12, pp. 2116–2122, 2008.
- [85] T. Holmgaard, Z. Chen, S. I. Bozhevolnyi, L. Markey, and A. Dereux, "Dielectric-loaded plasmonic waveguide-ring resonators," *Opt. Express*, vol. **17**, no. 4, p. 2968, 2009.
- [86] B. Min, E. Ostby, V. Sorger, E. Ulin-Avila, L. Yang, X. Zhang, and K. Vahala, "High-Q surface-plasmon-polariton whispering-gallery microcavity," *Nature*, vol. **457**, no. 7228, pp. 455–458, 2009.
- [87] K. Q. Le and P. Bienstman, "Nanoplasmonic ring resonator for biosensing applications," *Proceeding of 15th Annual Symposium of the IEEE Photonics Benelux Chapter*, Netherlands, 2010.
- [88] M. Soltani, "Novel integrated silicon nanophotonic structures using ultra-high Q resonators," PhD Dissertation, Georgia Institute of Technology, 2009.

- [89] W. Bogaerts, P. De Heyn, T. Van Vaerenbergh, K. De Vos, S. Kumar Selvaraja, T. Claes, P. Dumon, P. Bienstman, D. Van Thourhout, and R. Baets, “Silicon microring resonators,” *Laser Photonics Rev.*, vol. **6**, no. 1, pp. 47–73, 2012.
- [90] J. Durnin, J. J. Miceli, and J. H. Eberly, “Diffraction-free beams,” *Phys. Rev. Lett.*, vol. **58**, no. 15, pp. 1499–1501, 1987.
- [91] J. Durnin, “Exact solutions for nondiffracting beams. I. The scalar theory,” *JOSA A*, vol. **4**, no. 4, pp. 651–654, 1987.
- [92] F. Gori, G. Guattari, and C. Padovani, “Bessel-Gauss beams,” *Opt. Commun.*, vol. **64**, no. 6, pp. 491–495, 1987.
- [93] M. L. Juan, M. Righini, and R. Quidant, “Plasmon nano-optical tweezers,” *Nat. Photonics*, vol. **5**, no. 6, pp. 349–356, 2011.
- [94] G. U. O. HongLian, L. I. ZhiYuan, G. U. O. HongLian, and L. I. ZhiYuan, “Optical tweezers technique and its applications,” *Sci. CHINA Phys. Mech. Astron.*, vol. **56**, no. 12, pp. 2351–2360, 2013.
- [95] D. McGloin and K. Dholakia, “Bessel beams: Diffraction in a new light,” *Contemp. Phys.*, vol. **46**, no. 1, pp. 15–28, 2005.
- [96] A. Drezet, A. L. Stepanov, A. Hohenau, B. Steinberger, N. Galler, H. Ditlbacher, A. Leitner, F. R. Aussenegg, J. R. Krenn, M. U. Gonzalez, and J.-C. Weeber, “Surface plasmon interference fringes in back-reflection,” *Europhys. Lett. EPL*, vol. **74**, no. 4, pp. 693–698, 2006.



## Acknowledgements

I am using this opportunity with pleasure to acknowledge everyone who supported me throughout the PhD studies. I am thankful for aspiring guidance and friendly advices during the work. I am grateful to the truthful and illuminating views on a number of issues related to the work.

First of all, I want to express my sincere gratitude towards my thesis advisor, *Prof. Hans Peter Herzig*, who believed in me and provided an opportunity to work in his group. His concrete guidance and mentorship throughout the research supported me to overcome the hard time. His pragmatic approach to see the problems provides unique and evident ways to understand the subject. He is always available for the scientific discussions. He is approachable with just a knock on his door.

I am grateful to the jury members, *Prof. Emiliano Descrovi*, *Dr. Maria-Pilar Bernal* and *Prof. Fabien Sorin*, for spending time to correct my thesis and providing their critical reviews on it.

I would like to thank my officemates, *Sophiane*, *Johana* and *Karin*, for the friendly atmosphere they built around. They are always ready for the discussions related to either optics or personal life. In particular, I progressed doing sports, thanks to *Karin* and *Johana*.

I would like to thank *Dr. Elsie Barakat* for her guidance and support.

I was lucky to have *Babak Lahijani Vosoughi* who helped me in experiments during last year of my PhD. My thanks to him for the fruitful optics-related discussions. I enjoyed time working with him.

Many thanks to *Dr. Nicolas Descharmes* and *Johana Bernasconi* for the French translation of my abstract.

My thanks to *Dr. Myun-Sik Kim* who is always ready to discuss topics related to optics and share his deep knowledge.

I would also like to thank to *Dr. Gaël Osowiecki* for providing support on software and electronics.

I am thankful to *Tania* for BSWs related fruitful discussions.

My thanks to *Marcel Groccia* for helping me in the laboratory.

I am grateful to my colleagues and friends, *Krishna, Greg, Sara, Daniel, Raphaël and Irène* for the happening and joyous environment in the group. Thanks to the friends from *Galatea lab* and *AQUA lab* for sharing those happy moments.

Many thanks to *Mme. Brigitte Khan* for her support in administrative affairs for the period of my stay and for her valuable advices on all other kind of matters.

I am also thankful to *Mme. Sandrine Piffaretti* for her help in administrative work.

Specially, I want to express my gratitude to my parents and family for their continuous love and support throughout the difficult phases. In particular, many thanks to my mother who kept waiting for me late nights during my experiments. My deepest feelings to my grandfather who passed away.....I miss you Dada Ji.

Finally, I reserve my heartfelt feeling to my husband, *Sandeep*, who has been a constant source of support and encouragement during the challenges. Thank you *Sandeep* for your understanding and cooperation throughout this work which would have not been possible otherwise.

At the end, I would like to thank Swiss National Science Foundation for funding this research activity under the project: Bloch Surface Waves Platform – SWAP.



## List of appendices

### A.Publications and Conferences

Most of this work has been published as a journal papers or conference proceedings/presentations.

#### Journal publications

1. **R. Dubey**, B. Vosoughi Lahijani, E. Barakat, M. Häyrinen, M. Roussey, M. Kuittinen, and H. P. Herzig. Near-field characterization of a Bloch-surfacewave-based 2D disk resonator, in Optics Letters, vol. 41(21), num. 275128, pp. 4867-4870, 2016.
2. **R. Dubey**, E. Barakat, M. Häyrinen, M. Roussey, S. Honkanen, M. Kuittinen and H. P. Herzig. Experimental investigation of the propagation properties of Bloch surface waves on dielectric multilayer platform, in Journal of the European Optical Society-Rapid Publications, vol. 13:5, 2017.
3. **R. Dubey**, B. Vosoughi Lahijani, M. Häyrinen, M. Roussey, M. Kuittinen, and H. P. Herzig. Bloch Surface Wave based waveguide grating as a Bragg mirror for 2D optics, Submitted, 2017.
4. B. Vosoughi Lahijani, **R. Dubey**, H. Badri Ghavifekr, M.-S. Kim, I. Vartiainen, M. Roussey and H. P. Herzig. Experimental demonstration of critical coupling of whispering gallery mode cavities on Bloch surface wave platform, at the final stage of submission, 2017.

## Conference proceedings

1. **R. Dubey**, E. Barakat, H. P. Herzig, " Bloch Surface Waves Based Platform for Integrated Optics", 2015 IEEE Photonics Conference **1092-8081**, Reston, Virginia, USA, Proceeding of IEEE Photonics, 2015.
2. **R. Dubey**, B. Vosoughi Lahijani, M.-S. Kim, E. Barakat and M. Häyrynen et al. Near-field investigation of Bloch surface wave based 2D optical components. Proceeding SPIE Photonics West 10106, San Francisco, CA, USA, 2017.
3. M.-S. Kim, **R. Dubey**, E. Barakat, and H. P. Herzig, "Nano-thin 2D axicon generating nondiffracting surface waves," Proceeding Optical MEMS and Nanophotonics (OMN),1–2 (2016).
4. M.S. Kim, E. Barakat, **R. Dubey**, T. Scharf, and H. P. Herzig, " Nondiffracting Bloch surface wave: 2D quasi-Bessel-Gauss beam", Proceeding OSA CLEO Pacific Rim Conference 2015, Busan, Korea, 2015.

## Conference presentations

1. **R. Dubey**, E. Barakat, and H. P. Herzig, " Bloch Surface Based Platform for Optical Integration", EOS Annual Meeting 2014, TOM 5 – Slow light in Nanostructures, Berlin, Germany, 2014.
2. **R. Dubey**, E. Barakat, H. P. Herzig, "Near Field Investigation of Bloch Surface Based Platform for 2D Integrated Optics", Progress In Electromagnetics Research Symposium, PIERS, Czech Republic, Prague, 2015.
3. **R. Dubey**, E. Barakat, M.-S. Kim and H. P. Herzig. Near-field characterization of 2D disk resonator on Bloch surface wave platform. 14th International Conference on Near-field Optics, Nanophotonics, and Related Techniques, Hamamatsu, 2016.
4. M.-S. Kim, **R. Dubey**, E. Barakat and H. P. Herzig. Exotic optical elements generating 2D surface waves. EOS Topical Meeting on Trends in Resonant Nanophotonics, Berlin, Germany, 2016.
5. M.-S. Kim, **R. Dubey**, E. Barakat and H. P. Herzig. 2D photonic nanojet via Bloch surface wave: limitations and beyond, 14th International Conference on Near-field Optics, Nanophotonics, and Related Techniques, Hamamatsu, 2016.
6. H. P. Herzig, E. Barakat, **R. Dubey** and M. S. Kim. Optics in 2D, Bloch surface wave phenomena and applications. 15th Workshop on Information Optics (WIO), 2016.



## B. Curriculum vitae

### Richa DUBEY

Doctoral Assistant (PhD), Optics & Photonics Technology Laboratory  
École polytechnique fédérale de Lausanne (EPFL)  
Neuchatel, Switzerland

Date of birth: 4th April 1986

Language: English (fluent),

French (intermediate), Hindi (mother tongue).

[richa.dubey@epfl.ch](mailto:richa.dubey@epfl.ch) ; +41 (0) 77 95 59 030

[www.linkedin.com/in/richa-dubey](http://www.linkedin.com/in/richa-dubey)

### EDUCATIONAL BACKGROUND

#### PhD in Optics & Photonics

2013 – 2017

Supervisor: Prof. Hans Peter Herzig  
École polytechnique fédérale de Lausanne (EPFL), Switzerland

*Designing and characterizing 2-dimensional nano-optical components such as ring resonators, wave guides, lenses on Bloch surface wave based multilayer platform with the aim of developing a nano-scale integrated optical system for integrated optics applications.*

#### Master in Technology

2009 – 2011

Laser Technology/Photonics Science and Engineering Programme  
Indian Institute of Technology Kanpur  
Master thesis – ‘An educational website for interferometry’

### NOTABLE ACHIEVEMENTS

- Best poster presentation award at '14th International Conference of Near-Field Optics, Nanophotonics and Related Techniques (NFO-14)', held at Hamamatsu, Japan, among 207 posters. **(2016)**
- Prestigious DAAD (The German Academic Exchange Service) doctorate scholarship to study in Germany. **(2013)**
- Obtained 98.1% All India GATE score (Graduate Aptitude Test in Engineering) among 100,000 candidates. **(2009)**

## **PROFESSIONAL EXPERIENCE**

**Finisar Corporation**  
**Ipoh, Malaysia**

**2011-2013**

*With \$1.2 billion in revenues, and 13,400 employees worldwide, Finisar is the largest Supplier of sub-optical systems for optical high speed communications such as optical transceivers, optical assemblies, RF-over-Fiber, and many more.*

### **Product Engineer**

*Main responsibilities include, the study of new designs of optical subassemblies with the aim of mass manufacturing, the improvement of optical performance of current subassemblies, and the manufacturing process improvements in terms of cost savings.*

- VCSEL SW TOSA (Vertical cavity Surface Emitting Laser, Shortwave-850nm, Transmitter Optical Sub-Assembly).
- 6 PIN ROSA APD ( Receiver Optical Sub Assembly, Avalanche Photo-Diode )
- Responsivity, Sensitivity and ORL (Optical return loss) of Photo-Diodes in Sub-Optical Assemblies.
- Studying and qualifying new designs of TOSA/ROSA in collaboration with Research and Development team, Singapore
- Cost saving projects (Manufacturing Process Improvement): the short lead length of TOSA/ROSA resulting in saving of gold, and the qualification of new epoxy used to bond header and housing.

## **TEACHING ACTIVITIES**

- Supervision of exchange student from Sahand University of Technology, Tabriz, Iran. **6 months (2016)**
- Teaching assistance in Ingénierie optique II, Microtechnique, Bachelor semester course. **(2013-2016)**

## **TECHNICAL SKILLS**

CST Microwave studio, SNOM, Matlab, SEM, AFM, C, CorelDraw, Zotero, OpenGL, Zemax, Solidworks, LabVIEW.

## **AREAS OF INTEREST**

Photonic Devices, Multi-heterodyne Interferometer, SNOM, Optics and photonics, Integrated optics, Optical Sensors, Optics at surfaces, two-dimensional optics.

## **LANGUAGES**

- English      Fluent
- French      Intermediate
- Hindi      Mother tongue

## **JOURNAL PUBLICATIONS**

- R. Dubey, *et.al*, ‘Near-field characterization of a Bloch surface wave based 2D disk resonator’, Opt. Lett. **41**(21), 4867(2016).  
<https://doi.org/10.1364/OL.41.004867>
- R. Dubey, *et.al*, ‘Experimental Investigation of the Propagation Properties of Bloch Surface Waves on Dielectric Multilayer Platform’, J. Eur. Opt. Soc.-Rapid Publ. **13**(1), 5 (2017). <http://link.springer.com/article/10.1186/s41476-016-0029-1>
- R. Dubey, *et.al*, ‘Bloch Surface Wave based waveguide grating as a Bragg mirror for 2D optics’, Submitted, (2017).

## **CONFERENCE PROCEEDINGS**

- R. Dubey, *et.al*, ‘Near-field investigation of Bloch surface wave based 2D optical components’, Proceeding of SPIE Photonics West **10106**, San Francisco, United States, 2017. <http://dx.doi.org/10.1117/12.2250394>
- R. Dubey, *et.al*, ‘Bloch Surface Waves Based Platform for Integrated Optics’, Proceeding of IEEE Photonics Conference (IPC) **1092-8081**, Reston, United States, 2015. [10.1109/IPCon.2015.7323451](http://dx.doi.org/10.1109/IPCon.2015.7323451)

## **CONFERENCE PRESENTATIONS**

- R. Dubey, *et.al*, ‘Near-field characterization of 2D disk resonator on Bloch surface wave platform’, The 14th International Conference on Near-field Optics, Nanophotonics, and Related Techniques, Hamamatsu, Japan, 2016.
- R. Dubey, *et.al*, ‘Near Field Investigation of Bloch Surface Based Platform for 2D Integrated Optics’, PIERS Progress In Electromagnetics Research Symposium, Prague, Czech Republic, 2015.
- R. Dubey, *et.al*, ‘Bloch Surface Based Platform for Optical Integration. TOM 5 – Metamaterials’, Photonic Crystals and Plasmonics: Fundamentals and Applications, Berlin, Germany, 2014.

